

INAUGURAL - DISSERTATION

submitted to the
Combined Faculties for the Natural Sciences and for Mathematics
of the Ruperto-Carola University of Heidelberg, Germany
for the degree of
Doctor of Natural Sciences

Put forward by
M.Sc. Maja Solin
Born in: Örnnäset (Luleå - Sweden)

Oral examination: 1. April 2009

Mapping of Tissue Oxygenation using
Quantitative BOLD Methods:
Stability under non-static conditions

Referees: Prof. Dr. Lothar R. Schad
Prof. Dr. Wolfgang Schlegel

Mapping of Tissue Oxygenation using Quantitative BOLD Methods: Stability under non-static conditions

A method to quantify the susceptibility difference ($\Delta\chi$) between venous blood and surrounding tissue by utilization of a tissue model has been previously used for simultaneous estimation of relative blood volume fraction (ζ) and the blood oxygenation level. In this work, the previously neglected effect of diffusion on the MR signal formation in the presence of a cylinder network was studied in simulations and validated in phantom measurements. To mimic a capillary network, phantoms were constructed by randomly coiling polyamide fibers ($\varnothing = 27 - 245 \mu m$, $\Delta\chi = 1.0 - 1.3 ppm$, $\zeta = 2 - 5 \%$). Additional measurements of $\Delta\chi$ between a single polyamide string and solutions of different $NiSO_4$ concentrations were performed. The relation found, $\Delta\chi = 0.23 \cdot [NiSO_4] + 0.31 ppm$, was used to validate the results obtained with the network phantoms. Simulations showed that in order to keep the relative error in $\Delta\chi$ below 10 % a SNR of 600 is required. If, however, ζ is previously known $\Delta\chi$ can be estimated with 3.2 % error already at a SNR of 200. Furthermore, it was found that neglecting the effect of diffusion causes an underestimation of $\Delta\chi$ of approximately 13 %. The sensitivity of the method to variation in the oxygenation level *in vivo* was demonstrated by modification of the oxygenation level using caffeine. An increase in $\Delta\chi$ of $0.12 \pm 0.04 ppm$ could be measured, 1 hour after intake of 200 mg caffeine. This sensitivity to oxygenation changes is encouraging for further studies of the theoretical cylinder network model as a tool for MR-based *in vivo* quantification of tissue oxygenation.

Bestimmung der Gewebe-Oxygenierung mittels quantitativer BOLD Methoden: Stabilität bei nicht-statischen Bedingungen

In vorherigen Arbeiten wurde eine Methode verwendet, um die Suszeptibilitätsdifferenz ($\Delta\chi$) zwischen venösem Blut und umgebendem Gewebe zu quantifizieren. Hierbei wurde ein Gewebemodell zur gleichzeitigen Bestimmung des relativen Blutvolumen (ζ) und der Gewebe-Oxygenierung verwendet. In dieser Arbeit wird der bisher vernachlässigte Effekt der Diffusion auf die MR Signalförmung in der Gegenwart eines Zylindernetzwerks mit Hilfe von Simulationen untersucht und in Phantommessungen validiert. Um ein Kapillarnetz nachzubilden wurden Phantome aus zufällig orientierten Polyamidfäden ($\varnothing = 27 - 245 \mu m$, $\Delta\chi = 1.0 - 1.3 ppm$, $\zeta = 2 - 5 \%$) konstruiert. Zusätzlich wurde $\Delta\chi$ zwischen einem einzelnen Polyamid-Faden und Lösungen verschiedener $NiSO_4$ Konzentrationen gemessen. Der gefundene Zusammenhang, $\Delta\chi = 0.23 \cdot [NiSO_4] + 0.31 ppm$, wurde zur Validierung der mit dem Netzwerk-Phantom gemessenen Resultate verwendet. Durch Simulationen wurde gezeigt, dass ein SNR von 600 benötigt wird, um einen relativen Fehler von $\Delta\chi$ kleiner als 10 % zu erreichen. Wenn jedoch ζ vorher bekannt ist, kann $\Delta\chi$ schon bei einem SNR von 200 mit 3.2 % relativem Fehler bestimmt werden. Des Weiteren wurde gezeigt, dass die Vernachlässigung der Diffusion eine Unterschätzung von $\Delta\chi$ um etwa 13 % verursacht, wenn der Gefäßdurchmesser von der Größenordnung der Diffusionslänge ist. Die Sensitivität der Messmethode auf Änderung der Oxygenierung *in vivo* wurde durch Veränderung der Oxygenierung mit Hilfe von Koffein demonstriert. Eine Stunde nach der Einnahme von 200 mg Koffein konnte ein Anstieg von $\Delta\chi$ um $0,12 \pm 0.04 ppm$ gemessen werden. Diese Sensitivität auf Veränderungen der Oxygenierung ist vielversprechend für weitere Studien des theoretischen Zylinder-Netzwerk-Modells, als Werkzeug für eine MR-basierte *in vivo* Quantifizierung der Gewebe-Oxygenierung.

To my family,
for the love and support

List of Abbreviations

α	Flip Angle
χ	Magnetic susceptibility
$\Delta\chi$	Difference in magnetic susceptibility between two materials
γ	Gyromagnetic ratio
ω	Angular frequency
ζ	Deoxygenated blood volume fraction
ADC	Apparent Diffusion Coefficient
B_0	Main magnetic field strength
BF	Blood Flow
BW	Band Width
CPMG	Carr-Purcell-Meiboom-Gill
CSF	Cerebrospinal Fluid
FID	Free Induction Decay
FOV	Field of View
GESFIDE	Gradient Echo Sampling of FID and Echo
GESSE	Gradient Echo Sampled Spin Echo
GRE	Gradient Echo
Hb	Deoxyhemoglobin
HbO ₂	Oxyhemoglobin
Hct	Hematocrit
IDEA	Integrated Development Environment for Applications
ISF	Interstitial Fluid
MR	Magnetic Resonance
MRI	Magnetic Resonance Imaging
MRO ₂	Metabolic Rate of Oxygen
NMR	Nuclear Magnetic Resonance
OEF	Oxygen Extraction Fraction
PET	Positron Emission Tomography
pO ₂	Oxygen partial pressure
PSF	Point Spread Function
R1	Spin-lattice/longitudinal relaxation rate
R2	Spin-spin/transverse relaxation rate
RF	Radio Frequency
RMSE	Root Mean Square Error
ROI	Region of Interest

SE	Spin Echo
SNR	Signal to Noise Ratio
SWI	Susceptibility Weighted Imaging
T1	Spin-lattice/longitudinal relaxation time
T2	spin-spin/transverse relaxation time
T2*	Relaxation time of spin-spin relaxation and reversible signal dephasing in static magnetic field inhomogeneities
T2'	Relaxation time of reversible signal dephasing in static inhomogeneities
TE	Echo Time
TR	Repetition Time
Y	Blood oxygenation level

Contents

I	Introduction	1
II	Basic principles	3
2.1	Nuclear Magnetic Resonance	3
2.1.1	Nuclear Spin and Magnetic Moment	3
2.1.2	Macroscopic Magnetization	5
2.1.3	Motion of Magnetic Moment in an External Field	6
2.1.4	Resonance Absorption and Rotating Frame of Reference	6
2.1.5	Relaxation in a Homogeneous Magnetic Field	7
2.1.6	Measurement Signal in NMR experiments	9
2.1.7	Relaxation in Inhomogeneous Magnetic Fields	10
2.1.8	Spin Echo	11
2.2	Magnetic Resonance Imaging	12
2.2.1	Spatial encoding	12
2.2.2	Image reconstruction and k-space	14
2.2.3	Imaging Methods	18
2.3	Physiological Properties of Blood	20
2.3.1	Microscopic vascular anatomy of the brain	20
2.3.2	Oxygen Transport in the Brain	21
2.3.3	Tissue Oxygen Consumption	22
2.3.4	Oxygenation Dependent Magnetic Properties of Blood	23

III Materials and Methods	25
3.1 Modeling blood vessels	25
3.1.1 Single Vessel in Homogeneous Tissue	25
3.1.2 Vessel Network in Homogeneous Tissue	27
3.2 Measurement Techniques	32
3.2.1 MR Scanners	32
3.2.2 MR Sequences	33
3.2.3 Measurement Phantoms	35
3.3 Evaluation Techniques	39
3.3.1 Macroscopic Inhomogeneity Correction	39
3.3.2 Single Cylinder Measurements	41
3.3.3 Cylinder Network Measurements	42
IV Results	45
4.1 Phantom Measurements	45
4.1.1 Macroscopic inhomogeneities	45
4.1.2 Single Cylinder	46
4.1.3 Network Phantom	50
4.2 Simulations	59
4.2.1 Static Evaluation of Non-static dephasing Data	59
4.2.2 Dependence on SNR and Sequence Parameters	59
4.2.3 Expected Effect <i>in vivo</i>	70
4.3 In Vivo Measurements	71
V Discussion	77
VI Conclusion and Outlook	87
Bibliography	94
List of Tables	95
List of Figures	98

Appendix A Phantom Measurements	101
Appendix B Simulations	119

I

Introduction

MAGNETIC RESONANCE IMAGING (MRI) is a non-invasive technique used to produce, spatially resolved, anatomical and functional images. The images are created using a powerful magnetic field accompanied by a beam of radio waves. Positioned in an external magnetic field, the hydrogen nuclei in the body behave like small magnets and line up with the magnetic field. The successive radio waves supply energy to the nuclei that disturbs their alignment. After the radio beam is switched off, the nuclei return to their steady state. By doing so, the nuclei produce a faint signal which can be detected, and subsequently localized.

One of the great advantages of MRI, compared to conventional x-ray or computed tomography scans, is the fact that exposure to x-ray radiation is avoided. During an x-ray examination, high energetic photons are produced and used for imaging. A large part of the energy is deposited in the examined object, which may lead to DNA damage. In MRI, electromagnetic radiation, no more energetic than normal radio waves is used together with a very strong magnetic field. Neither static magnetic fields nor radio waves have any known side effects for humans¹. Furthermore, MRI has the ability to give different information about structures in the body than can be seen with an X-ray, ultrasound, or computed tomography scan. One of the most important attributes of MRI, which distinguishes it from all other human imaging techniques, is the high quality of soft tissue contrast. In standard MRI, the contrast is given by the difference in density of the observed nucleus, and by the, so-called, relaxation times, which describes how fast the nuclei return to their steady state after excitation. Those parameters can be arbitrarily mixed using numerous imaging techniques, producing a great variety of contrasts.

The relaxation times of an atomic nucleus are determined by the local magnetic field it experiences. In turn, the local magnetic field is affected by a large number of parameters, including blood flow, diffusion and other physiological phenomena. Hence, MRI offers, in addition to an anatomical imaging method, a noninvasive way to access functional parameters. In 1988, Seiji Ogawa and his colleagues discovered that small veins in the brain give extra contrast to the image. The phenomenon was named Blood Oxygenation

¹Even though radio waves do not have any direct side effects, intensive RF exposure can cause heating of the body. For this reason, limits that restrict radio frequency heating effects are present in the clinic.

Level Dependent (BOLD) effect, since the signal change were found to be dependent on the oxygenation level in the veins. The explanation for this effect is that deoxyhemoglobin in blood, as present in the veins, is paramagnetic, in contrast to the surrounding tissue, and therefore distorts the magnetic environment of the surrounding water molecules. Hence, information about the oxygenation of the tissue could be attained by quantification of this distortion. Since its discovery, the dynamic properties of the BOLD effect have been widely studied in, so-called, functional MRI experiments of the brain, i.e. to measure the hemodynamic response related to neural activity. However, the BOLD effect during the baseline, i.e., without stimulation, state of the brain has not received much attention.

However, quantitative mapping of oxygen supply in the brain during resting state is of great interest since such maps can provide important information about tissue viability. Oxygen partial pressure is an important parameter in the metabolic processes of cells and plays a crucial role in many pathophysiological conditions. Oxygenation is known to be a central factor for the aggressiveness and metastasis tendency of cancer tumors [Brown und Giaccia, 1998]. In addition, hypoxia is a major obstacle to tumor therapy and is associated with poor outcome for cancer patients [Molls et al., 1998]. The practical diagnostic possibilities for quantification of cerebral blood oxygenation are few although several measurement methods exist. The available methods are either strongly invasive (oxygen electrodes) or require a toxic contrast agent (^{19}F) and are therefore almost exclusively used in animal experiments. Near infrared spectroscopy can be used for non-invasive measurements of blood oxygenation, however, only to scan cortical tissue [Malonek et al., 1997]. Positron Emission Tomography (PET) has problems with the short half-life of the tracers used for oxygenation measurements. In addition, PET is expensive and may not be so commonly available [Ito et al., 2004].

Yablonskiy und Haacke [1994] proposed a theoretical model predicting the MR signal dephasing in brain parenchyma in presence of deoxyhemoglobin. The signal decay depends on the vascular network, which can be characterized by its relative volume fraction, and the amount of oxygen in the blood. Since then, this model has been extended to include diffusion effects [Kiselev und Posse, 1999], as well as effects arising from extracellular fluid and blood [He und Yablonskiy, 2007]. An independent verification of the practical use of the diffusion theory has not been carried out yet.

The aim of this work was to verify and investigate the stability of the above mentioned model under non-static dephasing conditions. Simulations and phantom experiments were performed as well as initial *in vivo* measurements.

II

Basic principles

2.1 Nuclear Magnetic Resonance

NUCLEAR MAGNETIC RESONANCE (NMR) was independently discovered by Purcell *et al.* and Bloch *et al.* in 1946 [Purcell et al., 1946; Bloch, 1946]. In 1973, Lauterbur found how magnetic resonance could be used to produce spatially resolved images by application of linear magnetic field gradients [Lauterbur, 1973]. His discovery builds the base for the modern Magnetic Resonance Imaging (MRI). Both discoveries have been awarded with the Nobel price. In this chapter, a brief introduction to the phenomena of Nuclear Magnetic Resonance will be given. A more detailed description of the theory of NMR can be found in the standard works of Abragam [1994] or Slichter [1992].

2.1.1 Nuclear Spin and Magnetic Moment

The physical basics of NMR are that all nuclei with an uneven number of nucleons possess an inherent angular momentum, also referred to as nuclear spin, \vec{I} . This nuclear spin has a related magnetic moment $\vec{\mu}$, proportional to \vec{I} ,

$$\vec{\mu} = \gamma \vec{I}. \quad (2.1)$$

The proportionality constant γ is the so-called gyromagnetic ratio, a characteristic measure for every nucleus (Table 2.1).

In theory, all nuclei with a non-zero spin can be used for NMR. In practice, however, the hydrogen nucleus 1H ($s = 1/2$) is almost exclusively used for MRI on humans, even though other nuclei, i.e. ^{23}Na and ^{31}P , have gained popularity during the last years. The favoring of 1H over other nuclei results from the high abundance in the human body as well as the very large gyromagnetic ratio of 1H (see Table 2.1). Henceforward, the discussion will be mainly focused on imaging of hydrogen protons.

Table 2.1. List of selected nuclear species with their spins (in units of \hbar), their associated magnetic moments (in units of a nuclear magneton, μ_n), gyromagnetic ratios (in units of $\text{rad} \cdot \text{s}^{-1} \cdot \text{T}^{-1}$), and their concentrations in human body. Table adopted from Haacke et al. [1999]

Nucleus	Spin	Magnetic Moment	γ	Concentration in Human Body ^a
^1H	1/2	2.793	$2.68 \cdot 10^8$	88 M
^{23}Na	3/2	2.216	$0.71 \cdot 10^8$	80 mM
^{31}P	1/2	1.131	$1.08 \cdot 10^8$	75 mM
^{17}O	5/2	-1.893	$-0.36 \cdot 10^8$	16 mM
^{19}F	1/2	2.627	$2.52 \cdot 10^8$	4 μM

^a The concentration of hydrogen (88 M) refers to tissue with 80 % water content, as gray matter in the brain, but will vary with tissue type.

The nuclear spin can be characterized by two dimensionless quantum numbers: The spin quantum number s , and the spin magnetic quantum number m_s . The spin quantum number can be non-negative integers or half-integers, and is related to the magnitude of the nuclear spin,

$$|\vec{I}| = \hbar \sqrt{s(s+1)} \quad \text{with} \quad s = 0, \frac{1}{2}, 1, \frac{3}{2}, \dots \quad (2.2)$$

where \hbar is Planck's constant ($1.055 \cdot 10^{-34} \text{ m}^2 \text{ kg/s}$). Furthermore, the spin magnetic quantum number is related to the orientation of the nuclear spin. Given an arbitrary direction z (usually determined by an external magnetic field), the z -projection of the nuclear spin is given by,

$$I_z = m_s \hbar, \quad (2.3)$$

where m_s can have values between $-s$ and s , in integer steps. This give rise to, in total, $2s + 1$ nuclear spin states. If no external field is present, those states are degenerate, i.e., they are the same. However, the degeneracy will disappear as soon as the nucleus interacts with an external magnetic field \vec{B} (Figure 2.1). The corresponding Hamiltonian for this, so-called, Zeeman-effect is,

$$H = -\vec{\mu} \cdot \vec{B} = -\gamma \vec{I} \cdot \vec{B}. \quad (2.4)$$

With the external magnetic field in the z -direction, $\vec{B} = (0, 0, B_0)$, the Hamiltonian reduces to,

$$H = -\gamma I_z B_0 \quad (2.5)$$

In analogy with other angular momentum operators, $2s + 1$ discrete, equidistant energy levels E_m arise as solutions to the eigenvalue equation of the Hamiltonian in Eq. 2.5 (Figure 2.1),

$$E_m = -\gamma m_s \hbar B_0. \quad (2.6)$$

The energy difference ΔE_m between two adjacent levels is given by,

$$\Delta E_m = \gamma \hbar B_0 = \hbar \omega_0. \quad (2.7)$$

Induction of transitions between the single Zeeman-levels can be achieved by application of a, to main field perpendicular, alternating field with the so-called Larmor frequency ω_0 ,

$$\omega_0 = \gamma B_0. \quad (2.8)$$

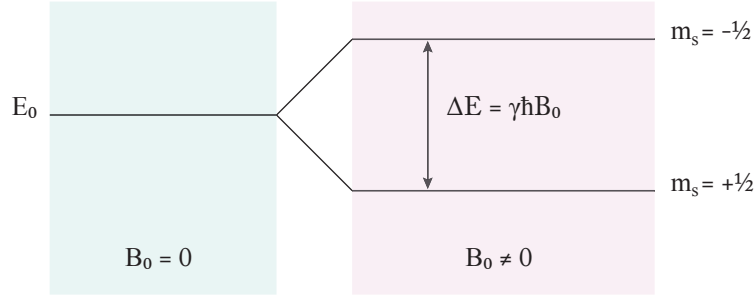


Figure 2.1. Zeemann splitting for a spin $I = 1/2$ system. When an external magnetic field is applied, the degeneracy of the energy levels disappears and two discrete energy levels will be present. The energy gap ΔE is determined by the magnetic field strength B_0 .

This phenomenon, which is based on interaction between high frequency fields and the nuclear magnetic moment, is called nuclear magnetic resonance.

2.1.2 Macroscopic Magnetization

In medical magnetic resonance imaging the typical size of a measured volume is on the order of 1 mm^3 , a volume that contains about $7 \cdot 10^{19}$ protons for water equivalent tissue. For such a large number of spins, a macroscopic magnetization, \vec{M}_0 , can be assumed as the sum of the expectation-values for the single magnetic moments, $\langle \mu_i \rangle$, per unit volume, for all N spins in the measured volume,

$$M_0 = \sum_{i=1}^N \frac{\langle \mu_i \rangle}{V} = \frac{N}{V} \cdot \sum_{m_s=-s}^s p_m \gamma \hbar m_s. \quad (2.9)$$

The right of Eq. 2.9 expresses the magnetization in terms of the population probability, p_m , of the Zeeman levels. At thermal equilibrium, these probabilities are described by a Boltzmann distribution,

$$p_m = \frac{1}{Z} e^{-E_m/k_B T}, \quad Z = \sum_m e^{-E_m/k_B T}, \quad (2.10)$$

where k_B is the Boltzmann constant ($1.38 \cdot 10^{-23} \text{ m}^2 \text{ kg/s}^2 \text{ K}$) and T is the absolute temperature. If an external field is applied, there will be a slight polarization of the spin angular momentum vector along the direction of the magnetic field. The surplus of spins in this parallel orientation, Δn , can be calculated as,

$$\Delta n = N \cdot \tanh \left(\frac{\gamma \hbar B_0}{2 k_B T} \right). \quad (2.11)$$

Since $k_B T \gg \gamma \hbar B_0$, Eq. 2.11 can be expanded to first order. The macroscopic magnetization in thermal equilibrium can then be calculated as,

$$\vec{M}_0 = \vec{\mu} \cdot \Delta n \approx \vec{\mu} N \frac{\gamma \hbar B_0}{2 k_B T}. \quad (2.12)$$

The population ratio between the two levels is of the order of 10^{-6} for protons at room temperature.

2.1.3 Motion of Magnetic Moment in an External Field

In case of thermal equilibrium, the macroscopic magnetization will be directed along the main magnetic field and its temporal evolution will be zero. If the equilibrium is disrupted the temporal evolution can be described with the following equation,

$$\frac{d\vec{M}(t)}{dt} = \vec{M}(t) \times \gamma \vec{B}(t). \quad (2.13)$$

The macroscopic magnetization describes a precession motion in a constant magnetic field, like a spinning top in the gravitation field.

2.1.4 Resonance Absorption and Rotating Frame of Reference

By application of an electromagnetic, time dependent field, \vec{B}_1 , transitions between the Zeeman levels can be induced, providing that the oscillating frequency agrees with the Larmor frequency ω_0 . The resulting change of the macroscopic magnetization is described by Eq. 2.13.

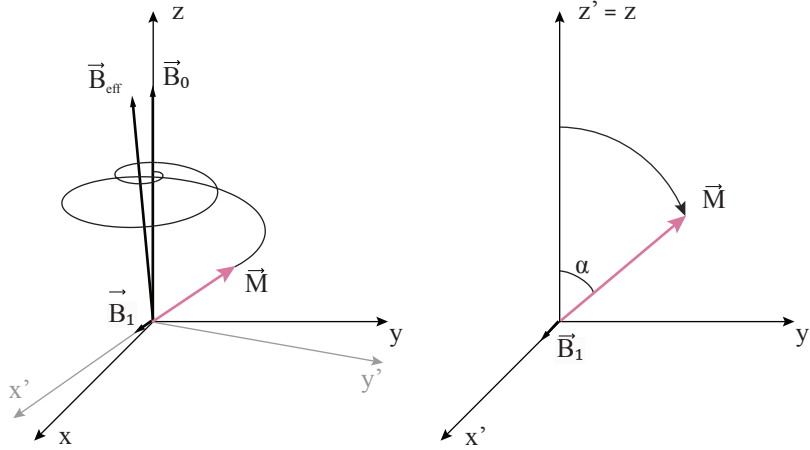


Figure 2.2. Motion of the magnetization vector in the laboratory and rotating coordinate system. In the laboratory system (left) the magnetization \vec{M} precess around the total magnetic field B_{eff} which is the sum of the static magnetic field B_0 and the time dependent B_1 field. By implementation of a rotating system (right) with the same frequency as B_1 , the motion of the magnetization can be described as a rotation around the B_1 field.

With a main magnetic field, B_0 , in z-direction, a transverse, circularly polarized, alternating field B_1 can be described by,

$$\vec{B}_1(t) = B_1 \cdot (\cos(\omega_{RF} \cdot t), \sin(\omega_{RF} \cdot t), 0). \quad (2.14)$$

By superposition of the main magnetic field and such an alternating field, Eq. 2.13 becomes explicit time dependent,

$$\frac{d\vec{M}(t)}{dt} = \vec{M}(t) \times \gamma \begin{pmatrix} B_1 \cos(\omega_{RF} \cdot t) \\ B_1 \sin(\omega_{RF} \cdot t) \\ B_0 \end{pmatrix}. \quad (2.15)$$

The time dependency can be eliminated by introduction of a rotating frame of reference (x', y', z') that rotates around the z -axis ($z = z'$) with the frequency ω_{RF} . Equation 2.15 then simplifies to (B_1 is directed in x -direction, without loss of generality),

$$\frac{d\vec{M}'(t)}{dt} = \vec{M}'(t) \times \gamma \begin{pmatrix} B_1 \\ 0 \\ B_0 - \frac{\omega_{RF}}{\gamma} \end{pmatrix} = \vec{M}'(t) \times \gamma \vec{B}_{\text{eff}}. \quad (2.16)$$

Again, this is a precession according to Eq. 2.13, but now around the effective magnetic field, B_{eff} . If the frequency, ω_{RF} , agrees with the Larmor-frequency, ω_0 , the contribution in z -direction will disappear and B_{eff} will be directed along the x' -axis. Hence, a precession motion about the B_{eff} field tips the magnetization vector by an angle α relative to the direction of the main magnetic field (Figure 2.2). The flip angle α is given by the amplitude and the duration of the B_1 -field,

$$\alpha = \gamma \int_0^t B_1(t') dt'. \quad (2.17)$$

Typical durations for 90° or 180° flip angles are a few milliseconds.

2.1.5 Relaxation in a Homogeneous Magnetic Field

According to the equation of movement (Eq. 2.13), a macroscopic magnetization vector rotating in the transversal plane should stay in this state without returning to the original steady state. However, this is only the case for an ideal collection of spins. In a real system, a return of the magnetization to the original state will be observed. Investigation of this lead Bloch [1946] to the (phenomenological based) Bloch equations, which are an extension of the classical equation of movement. It is assumed that the longitudinal and transverse components of the magnetization, after a disturbance, strive after their steady states M_0 and 0, respectively. For the three components of the magnetization vector, the following equations are valid,

$$\frac{dM_x}{dt} = \gamma \left(\vec{M} \times \vec{B} \right)_x - \frac{M_x}{T_2}, \quad (2.18)$$

$$\frac{dM_y}{dt} = \gamma \left(\vec{M} \times \vec{B} \right)_y - \frac{M_y}{T_2}, \quad (2.19)$$

$$\frac{dM_z}{dt} = \gamma \left(\vec{M} \times \vec{B} \right)_z - \frac{M_0 - M_z}{T_1}. \quad (2.20)$$

The two introduced time constants, T_1 and T_2 , characterize the relaxation of the magnetization. The constant T_1 is called longitudinal or spin-lattice relaxation time, and the constant T_2 is called transverse or spin-spin relaxation constant.

2.1.5.1 Spin-Lattice Relaxation

After the longitudinal magnetization has been flipped into the transverse plane, it starts to return to the original state. As the spin system exchanges the excess energy with the surroundings (i.e., the lattice) during this process, it is referred to as spin-lattice relaxation (T_1 relaxation). The thermal motion of the molecules creates time fluctuating magnetic fields, which induce transitions between the spin states whenever they agree with the resonance frequency. The so-called spin-lattice relaxation rate $R_1 = 1/T_1$ is a measure for the transition probability between the Zeeman-levels [Slichter, 1992].

Under the assumption of a homogeneous static magnetic field in the z -direction, the Bloch equation for the longitudinal magnetization (Eq. 2.20) simplifies to a first order linear differential equation,

$$\frac{dM_z}{dt} = -\frac{M_0 - M_z}{T_1}. \quad (2.21)$$

Solving Eq. 2.21 yields the following expression for the longitudinal magnetization,

$$M_z(t) = M_0 \left(1 - e^{-t/T_1}\right) + M_z(t_0)e^{-t/T_1}. \quad (2.22)$$

Equation 2.22 describes the so-called free relaxation of the longitudinal component of the magnetization in an ideal probe without intrinsic field inhomogeneities in a homogeneous magnetic field. The relaxation process is shown schematically in Figure 2.3.

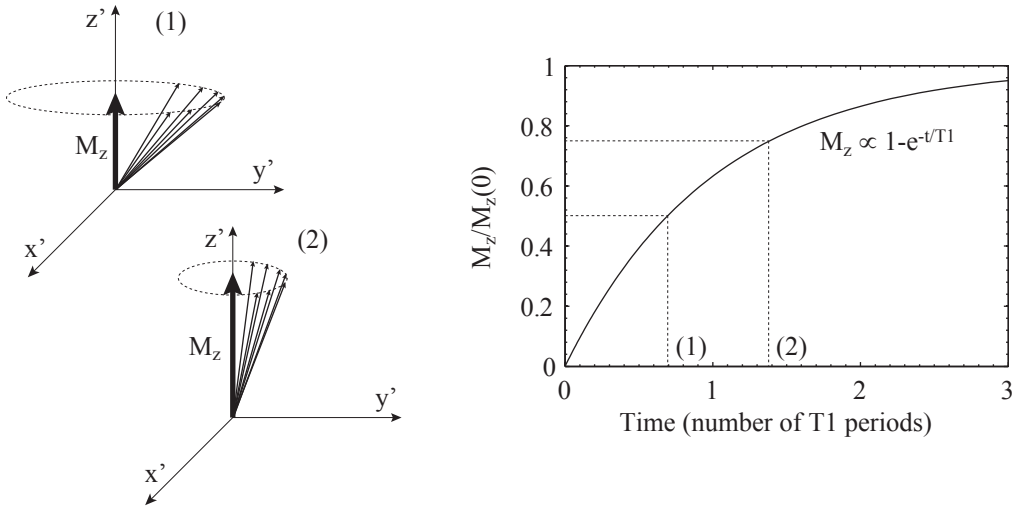


Figure 2.3. Spin-Lattice Relaxation. Directly after a 90° excitation pulse, no longitudinal magnetization is present. It returns to its equilibrium state with the spin-lattice relaxation time constant, T_1 .

2.1.5.2 Spin-Spin Relaxation

The spin-spin relaxation (T_2 relaxation) describes the dephasing of the transverse component of the magnetization. Due to Brownian molecular movement, quickly varying field

in the vicinity of every spin in a probe are created. As a result, not all spins precess with the same frequency and the initial phase coherence will be lost over time. This will be observed as an exponential decay of the macroscopic transversal magnetization. The characteristic spin-spin relaxation rate $R_2 = 1/T_2$ is introduced as measure for the decrease of the transversal component.

With a homogeneous magnetic field in the z-direction, the transverse relaxation can be expressed as follows (cf. Eq. 2.18 and 2.19),

$$\frac{dM_{xy}}{dt} = -i\gamma B_0 M_{xy} - \frac{M_{xy}}{T_2}. \quad (2.23)$$

The solution to this first order differential equation is given by,

$$M_{xy}(t) = M_{xy}(0)e^{-i\gamma B_0 t - t/T_2}. \quad (2.24)$$

Equation 2.24 describes the free relaxation of the transverse component of the magnetization. The decay of the transversal component is called free induction decay (FID) and is shown schematically in Figure 2.4.

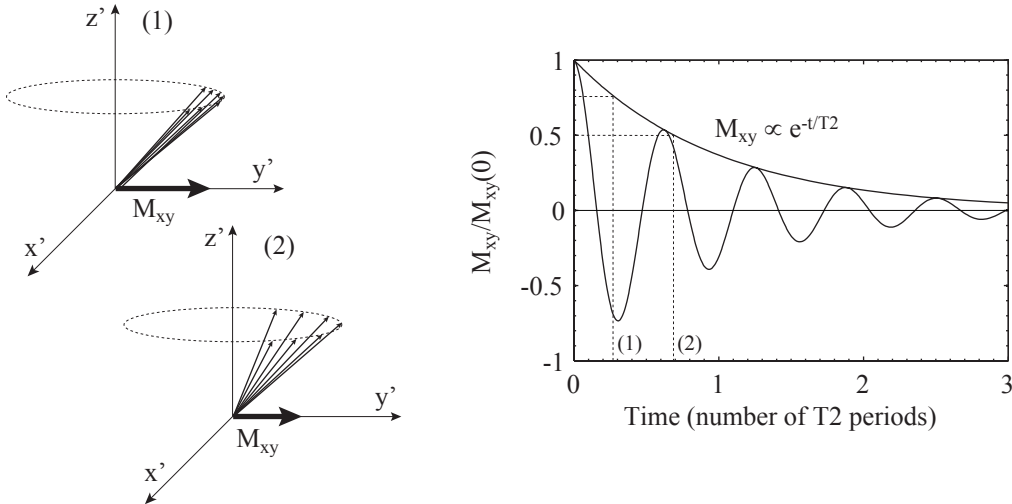


Figure 2.4. Spin-Spin relaxation. Due to dephasing of the individual spins, the magnitude of the transverse magnetization decreases after excitation. The time constant that describe the decay of the transverse magnetization is called the spin-spin relaxation time, T_2 .

2.1.6 Measurement Signal in NMR experiments

The signal measured in an NRM experiment is directly proportional to the transverse component of the magnetization, M_{xy} . The oscillating transverse component induces a voltage proportional to M_{xy} in a receiving coil positioned transversely to the main magnetic field. The longitudinal component, M_z , cannot be directly measured, which means that the signal is given by Eq. 2.24.

The detection of the transverse magnetization is often performed by means of two coupled coils with a constant phase relationship. Hence, it is convenient to represent the transverse magnetization as a complex quantity,

$$M_{xy} = M_x + iM_y \equiv |M_{xy}| e^{i\phi}. \quad (2.25)$$

In reality, the signal is demodulated after detection by multiplication with a sine and a cosine function, each synchronized with the Larmor frequency. As a result, only the exponentially decaying envelope, as shown in Figure 2.4, is measured.

Since the spin density can fluctuate spatially, the signal is a function of position. However, in an MRI experiment a mean signal from the whole measurement volume is detected, which makes integration over the volume necessary,

$$S(t) \propto \int_V M_{xy}(t_0) e^{i\gamma B_0 t} \cdot e^{-t/T^2} d\vec{r}. \quad (2.26)$$

2.1.7 Relaxation in Inhomogeneous Magnetic Fields

In addition to the quickly varying local fields that cause T_2 relaxation, local magnetic field variations can be present due to imperfections in the main magnetic field or due to magnetic, non-homogeneous, probes that are placed in the field.

The dependency of the magnetization, \vec{M} , on the magnetic field strength, \vec{B}_0 , can be described by the susceptibility, χ ,

$$\vec{M} = \chi \vec{B}_0. \quad (2.27)$$

For most materials, χ is on the order of a few parts per million (ppm), and may be either negative (diamagnetic materials) or positive (paramagnetic materials).

In the case of probes that consist of areas with different magnetic properties, discontinuities in the susceptibility will be present, and the magnetic field inside the probe will be position dependent. The exact form of the magnetic field distribution, $B_s(\vec{r})$, depends on the geometrical position of the areas with different magnetic properties within the medium, and can be described as a function of the susceptibility difference, $\Delta\chi$, between the compartments,

$$B_s(\vec{r}) = f(\vec{r}, \Delta\chi). \quad (2.28)$$

Those field variations leads to an additional phase in the local magnetization, M_{xy} , proportional to the local magnetic field and, assuming that no diffusion effects are present, linearly increasing with time,

$$\phi(\vec{r}, t) = \gamma B_s(\vec{r}) t. \quad (2.29)$$

This creates a phase distribution within the probe. According to Eq. 2.26, the total measured signal is then given by,

$$S(t) \propto \int_V M_{xy}(t_0) e^{i\gamma B_s(\vec{r}) t} \cdot e^{-t/T^2} d\vec{r}. \quad (2.30)$$

Hence, in a magnetic inhomogeneous medium, an additional dephasing of the spins is present, which shortens the relaxation time. This supplementary relaxation is described by the time constant $T2'$. Equation 2.30 now reduces to,

$$S(t) \propto e^{-t/T2'} \cdot e^{-t/T2}. \quad (2.31)$$

The time constant $T2'$ is referred to as the reversible relaxation time since the signal decay it describes can be reversed if the magnetization is inverted using a 180° -pulse (see section 2.1.8). The effective relaxation time, $T2^*$ is defined as,

$$\frac{1}{T2^*} = \frac{1}{T2} + \frac{1}{T2'}. \quad (2.32)$$

This mono-exponential signal decay is only valid for a Lorentzian distribution of resonance frequencies, which for instance is produced by randomly distributed magnetic dipoles [Brown, 1961]. Other geometries such as vascular networks or single blood vessels lead to non-mono-exponential signal decays and will be discussed later in this work.

2.1.8 Spin Echo

In the beginning of MR history, it was difficult to get a measurable signal due to inhomogeneous magnetic fields that caused very short $T2^*$ relaxation times. However, the two dephasing processes that destroy the measurement signal (spin-spin interaction and field inhomogeneities) are fundamentally different. The spin-spin interaction is a random and irreversible process. On the contrary, the magnetic field inhomogeneities have a constant static influence on the spin system and can theoretically be accounted for. In the year 1950, Hahn published the first spin echo (SE) measurement [Hahn, 1950], and offered with this a tool to correct the influence of static inhomogeneities. A 180° RF pulse is applied at some point in time ($TE/2$) after the magnetization has been flipped into the transverse plane by a 90° -pulse. In the transverse plane, the individual magnetic moments immediately start to dephase. The subsequent 180° -pulse flips the individual spins around one of the transverse axes, in a mirror-like fashion. After an additional time, the spins once again are back in phase, rebuilding the FID and resulting in an echo at a time TE . The result is a measurement insensitive to magnetic field inhomogeneities and a measurement signal that is dependent on the local $T2$ of the probe. This sequence of events is summarized in Figure 2.5.

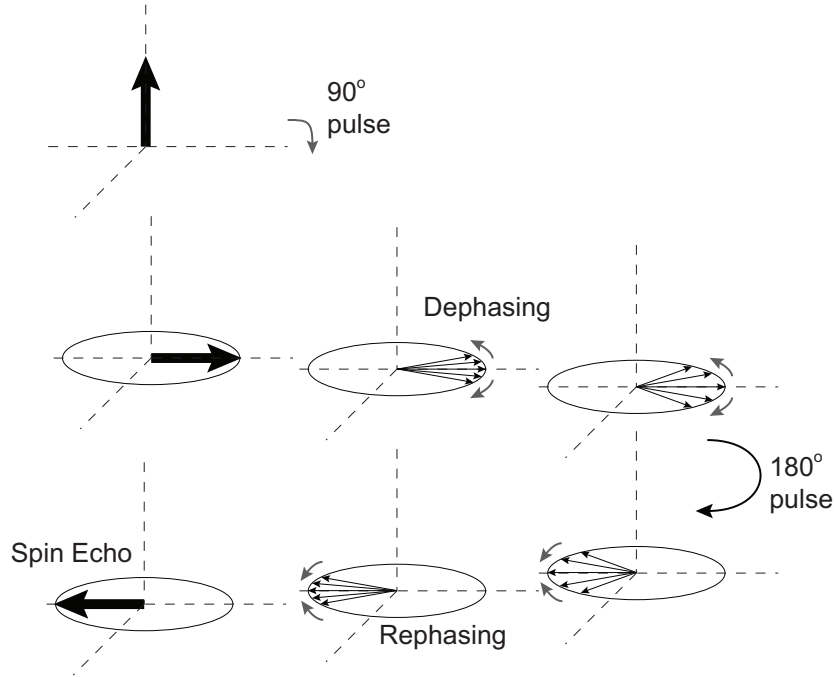


Figure 2.5. Spin Echo formation. The effect of a 180° refocusing pulse on the spin system during spin echo generation. The figure is explained in the text.

2.2 Magnetic Resonance Imaging

IN THIS SECTION, the techniques used to produce spatially resolved images with magnetic resonance are briefly outlined. For further reading Haacke et al. [1999] and Vlaardingerbroek und den Boer [2003] are recommended.

2.2.1 Spatial encoding

In order to reconstruct an image, it is necessary to encode the emitted signal so that its components can be related to the spatial position of the nuclei that contribute to them. This is achieved by a position dependent modification of the signal phase. As described in section 2.1.3, the precession frequency has a linear dependence on the external magnetic field. Hence, a position dependent modification of the phase can be achieved using additional linear gradient fields superimposed on the main magnetic field. The electromagnetic fields used for this purpose are parallel to the external magnetic field, but have a linear field strength gradient in one spatial direction. Consequently, they are referred to as gradient fields, \vec{G} , or just gradients. In MRI three gradients are generally used, each with a gradient strength that changes along one spatial direction (x,y,z),

$$\vec{G} = \left(\frac{\delta B_z}{\delta x}, \frac{\delta B_z}{\delta y}, \frac{\delta B_z}{\delta z} \right). \quad (2.33)$$

This gives the following resonance condition,

$$\omega(\vec{r}) = \gamma B(\vec{r}) = \gamma(B_0 + \vec{r} \cdot \vec{G}). \quad (2.34)$$

By application of gradient fields, the resonance frequency for every sub-volume, voxel, becomes dependent on its position. The individual voxel signal can then be reconstructed using frequency analysis of the NRM signal. Due to the use of frequency analysis, such an imaging method is entitled Fourier imaging. 2D Fourier imaging has three spatial encoding steps, one for every spatial direction. They are often referred to as slice selection, phase encoding and frequency encoding.

2.2.1.1 Slice Selection

The slice selection gradient is used to selectively excite a two-dimensional slice in the three-dimensional measurement volume. This is done by simultaneous application of a gradient field, G_z , perpendicular to the slice orientation, and a radio frequency (RF) pulse with a narrow bandwidth $\Delta\omega_{RF}$. The magnetic field along the slice selection direction (here z-direction) is then,

$$B_z(z) = B_0 + z \cdot G_z. \quad (2.35)$$

Since the angular frequency of the two fields is superimposed,

$$\omega(z) = \omega_0 + \omega_G(z) = \gamma \cdot (B_0 + z \cdot G_z), \quad (2.36)$$

the Larmor frequency will be dependent on the position along the z-axis. Hence, the resonance condition from Eq. 2.36 is satisfied only for spins that precess with a frequency that is contained in the bandwidth of the excitation pulse (Figure 2.6). The slice thickness, Δz , is controlled by the amplitude of the gradient field and the bandwidth of the RF pulse, and is given by,

$$\Delta z = \frac{|\omega(z_1) - \omega(z_2)|}{\gamma G_z} = \frac{\Delta\omega_{RF}}{\gamma G_z}. \quad (2.37)$$

The method described above is called slice selective excitation. If the RF pulse is applied without an applied slice selection gradient, the whole volume is excited, a method referred to as global excitation.

2.2.1.2 Phase Encoding

In order to spatially resolve the excited slice to generate an image, a gradient is applied for a certain time, t_y , in a direction parallel to the slice (here y-direction). During this time the precession frequency, and with this the accumulated phase, is dependent on the position along the y-axis. For constant gradients, the following is valid,

$$\omega(y) = \gamma \cdot (B_0 + y \cdot G_y). \quad (2.38)$$

After the gradient is switched off, the magnetization continues to precess with the initial Larmor frequency. However, the accumulated phase remains,

$$M_{xy} = |M_{xy}| \cdot e^{i \int_0^{t_y} \omega(t) dt} = |M_{xy}| \cdot e^{i\phi}. \quad (2.39)$$

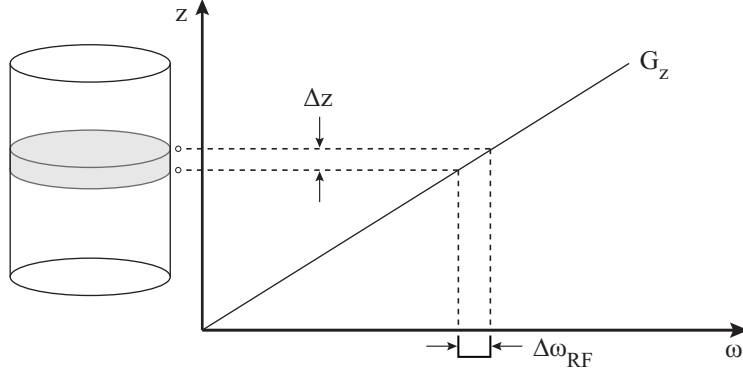


Figure 2.6. Slice selective excitation. A RF pulse with bandwidth, $\Delta\omega_{RF}$, together with the slice selection gradient, G_z , defines the slice thickness Δz .

The signal cannot be spatially resolved using only one phase encoding step, because the signal will not contain different frequencies in y-direction. To overcome this, the phase encoding step has to be repeated many times with different G_y .

2.2.1.3 Frequency Encoding

During the signal readout an additional gradient is switched in the last spatial direction (here x-direction). The precession frequency now depends on the location along the x-direction,

$$\omega(x) = \gamma(B_0 + x \cdot G_x). \quad (2.40)$$

The signal received during the readout time contains several frequencies, which allows positioning of the signal origin along the x-axis using Fourier analysis (Figure 2.7).

2.2.2 Image reconstruction and k-space

The measured signal in a slice selective 2D imaging experiment can be described in total analogy to the free induction decay in a NMR experiment (Eq. 2.26). The signal is proportional to the volume integral of the complex transverse magnetization in the measurement volume, now represented by the excited slice. Furthermore, the phase factors from the phase and frequency-encoding gradients have to be considered,

$$S(t, G) = S_0 \iiint_{\text{slice}} M_{xy}(t_0) e^{i\gamma \left(\int_0^{t_y} G_y(\tau) y d\tau + \int_0^{t_x} G_x(\tau) x d\tau \right)} dx dy. \quad (2.41)$$

Let us define two wave numbers, k_y and k_x , as

$$k_y = \gamma \int_0^{t_y} G_y(\tau) d\tau, \quad (2.42)$$

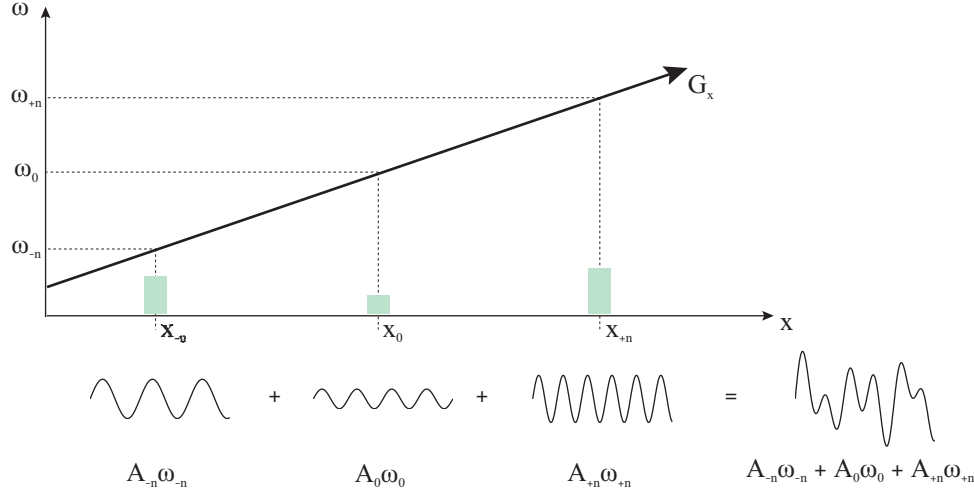


Figure 2.7. Frequency encoding. By application of the frequency encoding gradient, G_x , the local precession frequency is dependent on the position along the x-direction while the signal amplitude (A) is proportional to the total amount of protons in each sample. The measured signal is the sum of the signal coming from all samples, but when applying Fourier analysis the individual components can be isolated.

$$k_x = \gamma \int_0^{t_x} G_x(\tau) d\tau. \quad (2.43)$$

Combining Eq. 2.42 and Eq. 2.43 with Eq. 2.41 yields the following signal expression for a 2D MRI experiment,

$$S(t, \vec{k}) = S_0 \iint_{\text{slice}} M_{xy}(t_0) e^{i(k_y \cdot y + k_x \cdot x)} dx dy. \quad (2.44)$$

According to Eq. 2.44, the data that are sampled using frequency and phase encoding can be interpreted as sampling of the wave numbers k_y and k_x in the Fourier space, frequently referred to as the k-space [Brown et al., 1982; Ljunggren, 1983; Twieg, 1983]. The trajectory in k-space is determined by the time modulation of the gradients, according to Eq. 2.42 and Eq. 2.43. The desired spatial distribution of the transverse magnetization can be obtained by taking the inverse Fourier transform of the raw data (Eq. 2.44)

$$M_{xy}(\vec{r}) = \frac{1}{S_0 \cdot (2\pi)^2} \cdot \iint_{\text{slice}} S(t, \vec{k}) \cdot e^{-i(k_x x + k_y y)} dk_x dk_y. \quad (2.45)$$

This is the fundamental equation of the spatially resolved MRI. Since M_{xy} is a complex quantity, it is possible to reconstruct magnitude images as well as phase images.

2.2.2.1 k-space characteristics

In practice, it is not possible to cover the whole k-space in a continuous manner, but a discrete number of points have to be sampled. The discrete sampling can be described

as multiplication of the continuous signal with a discrete sampling function $u(k)$. The convolution theorem in Fourier theory states that the Fourier transform of a product equals the convolution of the Fourier transforms. Hence, the reconstructed image, $M_{sample}(\vec{r})$, is the convolution of the inverse Fourier transform, $U(\vec{r})$, of the sampling function and the original object, $M(\vec{r})$,

$$M_{sample}(\vec{r}) = M(\vec{r}) \otimes U(\vec{r}). \quad (2.46)$$

Cartesian sampling of N_x data points with a distance Δk_x of one line in k-space is accomplished using a frequency encoding gradient with constant amplitude G_x and equidistant sampling time Δt . Furthermore, the discrete sampling in phase encoding direction is carried out, as mentioned in 2.2.1.2, by changing the amplitude of the phase encoding gradient stepwise with ΔG_y . The sampling density in k-space is then given by

$$\Delta k_x = \gamma G_x \Delta t_x \quad (2.47)$$

$$\Delta k_y = \gamma \Delta G_y t_y \quad (2.48)$$

The sampling function can be described by an infinite set of equally spaced δ -functions, the Dirac comb. The measured signal is then,

$$S_{sample}(t, \vec{k}) = S(t, \vec{k}) \sum_{n=-\infty}^{+\infty} \delta(k - n\Delta k). \quad (2.49)$$

The Fourier transform of a Dirac comb with period Δk is yet another Dirac comb, but now with the period $1/\Delta k$. This results in the following expression for the reconstructed distribution of the magnetization,

$$M_{sample}(\vec{r}) = M_{xy}(\vec{r}) \otimes \sum_{n=-\infty}^{+\infty} \delta(x - \frac{m}{\Delta k}). \quad (2.50)$$

Hence, the image reconstruction results in an infinite series of images, reoccurring at the positions corresponding to the positions $(1/\Delta k)$ of the δ -functions. To avoid image overlapping (so-called aliasing), $1/\Delta k$ has to be chosen larger than the field of view (FOV),

$$\Delta k \leq \frac{2\pi}{FOV}. \quad (2.51)$$

Combining Eq. 2.47 and 2.48 with Eq. 2.51, and using $FOV_x = N_x \Delta x$ and $FOV_y = N_y \Delta y$, yields the following sampling criteria,

$$\Delta t_x \leq \frac{2\pi}{\gamma G_x N_x \Delta x} \quad (2.52)$$

$$\Delta G_y \leq \frac{2\pi}{\gamma t_y N_y \Delta y} \quad (2.53)$$

These requirements are equivalent to the Nyquist sampling theorem, stating that exact reconstruction of a function is possible only when the function is sampled at a rate larger than, or equal, twice the maximal signal frequency [Shannon, 1949]. Hence, the resolution is determined by the maximum value of the k-space vector. The image pixel size is given by,

$$\Delta x = \frac{2\pi}{\gamma G_x \Delta t_x N_x} \quad (2.54)$$

$$\Delta y = \frac{2\pi}{\gamma \Delta G_y t_y N_y} \quad (2.55)$$

The image resolution can be increased by using a stronger readout gradient G_x or by increasing the sampling time Δt_x , and if the number of samples N_x is kept constant, this will reduce the FOV_x . Similarly, FOV_y will be reduced if t_y or G_y is increased while keeping N_y constant. Hence, to avoid aliasing, the number of samples has to be increased accordingly with image resolution. The characteristics of k-space are presented in Figure 2.8.

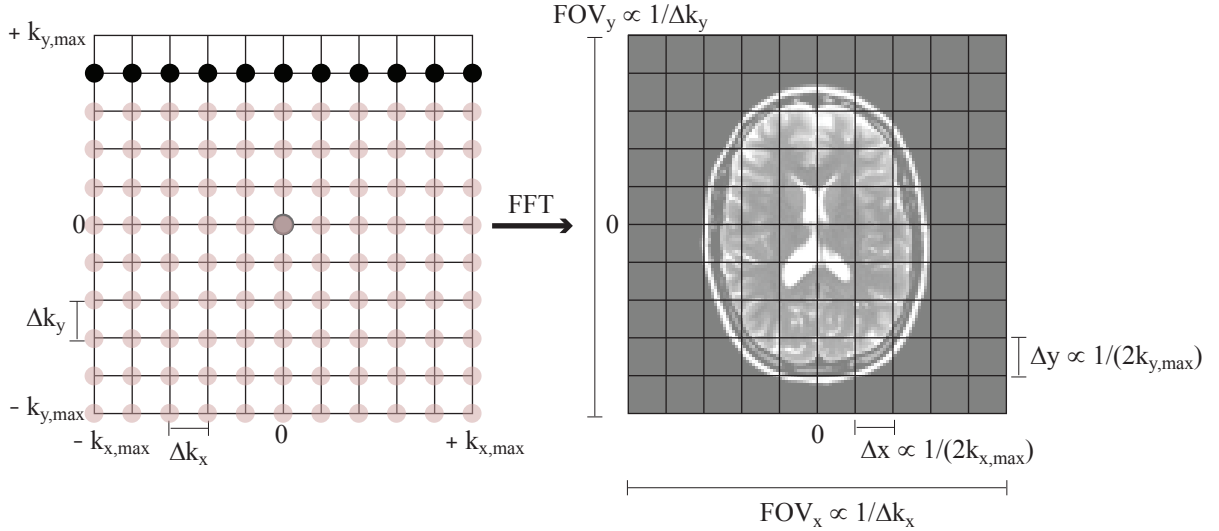


Figure 2.8. Schematic view of the concept of k-space. The signal measured at specific values of k_x and k_y is arranged in a matrix, the so-called k-space. Fourier analysis transforms the k-space to the image space.

2.2.2.2 Point Spread Function

In addition to the discrete sampling, we have to work with finite spatial frequencies instead of covering the k-space in an infinite manner. Again, this can be expressed mathematically as multiplication of the, in theory, infinite raw data with a certain window function, $h_\omega(k)$,

$$S_{sample}(k) = S(k) \cdot h_\omega(k). \quad (2.56)$$

The reconstructed magnetic field distribution is then,

$$M_{sample}(\vec{r}) = M(\vec{r}) \otimes H_\omega(\vec{r}). \quad (2.57)$$

The inverse Fourier transformation of the window function is the so-called point spread function (PSF). Using a rectangular window function, having the width of the sampled frequency interval, results in a sinc-shaped PSF. This means that each point of the measuring volume is imaged as its convolution with a sinc-function. The distinct side lobes of the sinc-function can appear as Gibbs ringing artifacts at sharp edges in the image [Folland, 1992].

2.2.3 Imaging Methods

The wave numbers (Eq. 2.42) that build up the k-space can be sampled in, basically, any desired trajectory by variation of the strength and the duration of the gradients. However, most of the pulse sequences used, samples the data on a Cartesian grid because this enables simple and fast image reconstruction. There are two fundamental types of MR pulse sequences; the spin echo and the gradient echo. All other MR sequences are variations of these two. The basic methods behind the two sequence types are presented in the following sections.

2.2.3.1 Spin Echo

Figure 2.9 shows a standard spin echo imaging sequence (left picture). The combination of the 90° pulse and the slice selection gradient define the image slice, and flips the magnetization in this slice to the transverse plane. Subsequently, the phase encoding gradient is switched in phase encoding direction (G_y) simultaneously as the so-called dephasing gradient is switched in frequency encoding direction (G_x). The 180° -pulse is the refocusing pulse given at time $TE_{SE}/2$. The maximum echo signal occurs at a time TE_{SE} . The signal read-out is accomplished using a rephasing gradient in frequency encoding direction. The sequence is repeated N_y times, with N_y different values for the phase encoding gradient. The time between successive excitations is called repetition time (TR). After the readout, the longitudinal magnetization has to recover to its equilibrium state before the sequence is repeated. Therefore, the major disadvantage of T2 weighted spin echo sequences is the demand of long TR, resulting in long acquisition times.

To the right in figure 2.9, a schematic description of how k-space is mapped during a SE acquisition is shown. The 90° pulse brings us to the k-space center (A). The phase encoding gradient lets us travel in k_y direction in k-space, and by choosing a specific gradient strength, one particular k_y -line can be selected. Simultaneously, the frequency-encoding gradient transports us in k_x direction in k-space and brings us to the far end of the selected k_y -line (B). The 180° pulse that reverses the effect of field inhomogeneities also reverses the effect of the gradients (B \rightarrow C). The read out gradient following the 180° pulse initiate the sampling of this k-space line (C \rightarrow D). Repeating this sequence for different amplitudes of the phase encoding gradient results in a fully sampled k-space.

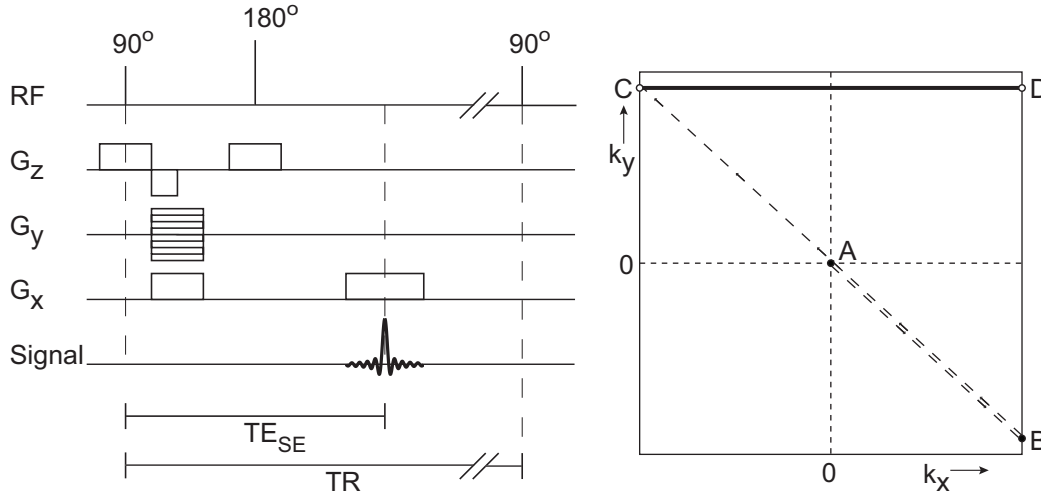


Figure 2.9. Schematic Spin Echo timing sequence (left) with corresponding k-space map (right). The figure is explained in the text.

2.2.3.2 Gradient Echo

Instead of using a 180° -pulse to rephase the spins into an echo, it is possible to detect the signal directly in the FID domain. In a gradient echo (GRE) sequence, the signal is dephased, by means of gradients, before the signal readout, and subsequently refocused during the signal readout, creating an echo at time TE . Since the additional phase accumulated by a spin packet is directly proportional to the time integral of the gradient, the echo will turn up when the areas under the gradient-time curve equal zero. One major advantage of the GRE technique is that an RF excitation pulse that partly flips the net magnetization vector into the transverse plane can be used. As a result, the longitudinal magnetization will recover to equilibrium much more rapidly, and a faster imaging procedure is possible. However, the gain in time is on the expense of SNR since a smaller flip angle produces less transverse magnetization and therefore less signal.

Figure 2.10 shows a standard GRE imaging sequence together with a schematic description of how k-space is mapped during a GRE acquisition. A slice selective excitation is accomplished using a slice selection gradient and a RF pulse, which typically has a rotation angle between 10° and 90° . Subsequently, a phase encoding gradient is applied, varied between G_y and $-G_y$ in several steps. The dephasing gradient in frequency encoding direction is applied simultaneously as the phase encoding gradient, and literally destroys the signal by dephasing it. The rephasing frequency encoding gradient, with inverted polarity with respect to the dephasing gradient, is turned on during the data acquisition and produces an echo because it refocuses the previous dephasing. The echo time is defined as the time between the excitation pulse and the maximum of the signal. The sequence is repeated every TR seconds. The TR period could be as short as milliseconds.

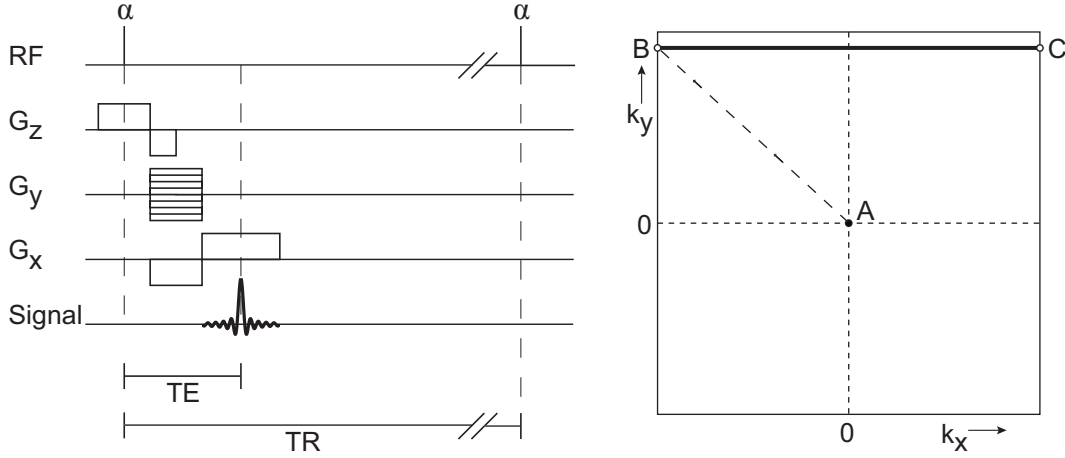


Figure 2.10. Schematic Gradient Echo timing sequence (left) with corresponding k-space map (right). The figure is explained in the text.

2.3 Physiological Properties of Blood

THE METHODS EXAMINED in this work aim to measure the oxygenation of human tissue using MRI. The physical basics of such a measurement are that the magnetic properties of the blood are dependent on its oxygenation level. The magnetic susceptibility difference that arises between venous blood and tissue creates an inhomogeneous magnetic field that can be detected since the created field variations induce associated signal losses in gradient echo images. In this section, the basic physiological processes that affect this effect are compiled.

2.3.1 Microscopic vascular anatomy of the brain

The sizes of the blood vessels in human brain are on the order of $120 - 240 \mu m$ for large intracortical supplying arteries, and $80 - 120 \mu m$ for draining veins. The arterioles and venules that are in connection with the capillary network have a size of $30 - 40 \mu m$ whereas the capillary network itself has a radius distribution that ranges from $20 \mu m$ down to $4 \mu m$ [Duvernoy et al., 1981]. A dense capillary network guarantees the oxygen supply to the gray matter in the brain. The network continues into the white matter but shows there a lower density. Figure 2.11 shows the vessel structure inside gray matter in the human cortex. As can be seen in the figure, the capillaries form an equally, spatially, distributed vessel network. The relative volume fraction of blood has been measured using positron emission tomography (PET) to 4.3 ml blood/ml in gray matter and 2.1 blood/ml in white matter [Yamaguchi et al., 1986]. Additionally, several MR studies have aimed to measure the blood volume. Their results, however, are not always consistent with each other or with the PET results. Nevertheless, all studies showed a consistent blood volume ratio between gray and white matter of about 2:1. The venous part of the blood vessel network has been measured, in dogs, to a volume fraction of 0.7 to the total blood volume [Moskalenko, 1980]. This part is the deoxygenated blood volume fraction, ζ , which is used in the MR

signal calculations of this work.

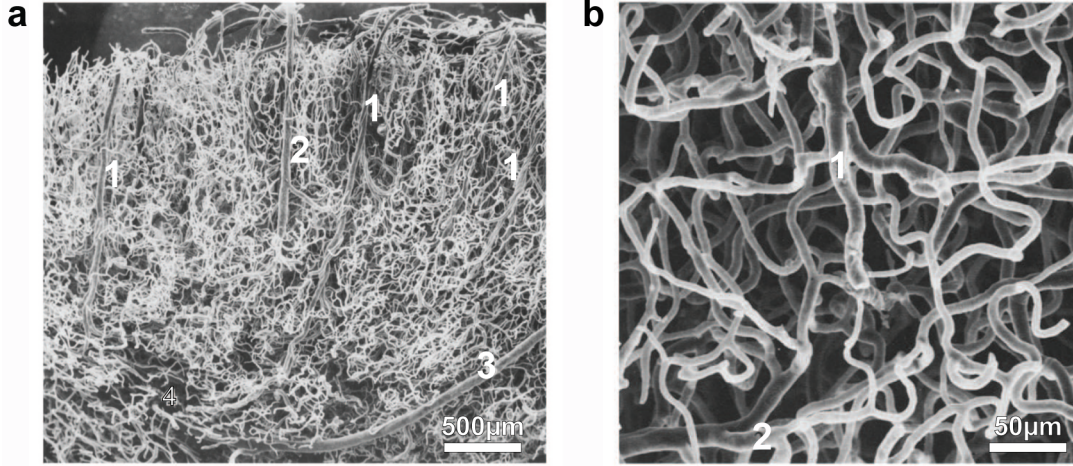


Figure 2.11. **a)** Overview of the cortical blood vessels. (1) Artery of gray matter, (2) vein of gray matter, (3) artery of white matter, (4) smaller vessels of the white matter. **b)** Detailed view of the capillary structure in the gray matter. (1) Arteriole, (2) venule. (Figures from Duvernoy et al. [1981])

2.3.2 Oxygen Transport in the Brain

The blood is an essential transport and communication medium for all mammals. The energy needed by cells in order to maintain their vital functions comes, almost exclusively, from oxidative degradation of nutrients, a process that requires the presence of glucose, proteins and enough molecular oxygen. The blood covers the glucose as well as the oxygen demands of the organ. The human blood consists primarily of aqueous plasma, which contains dissolved proteins, electrolytes, water-soluble nutrients, vitamins, gases and blood cells. The essential blood cells present are red blood cells (erythrocytes), white blood cells (leukocytes) and thrombocytes. The volume fraction of erythrocytes in the blood is called Hematocrit (Hct) and amounts to 0.44 – 0.46 for healthy grown up males, and 0.40 – 0.43 for healthy grown up females [Schmidt und Thews, 1995].

The erythrocytes main task is oxygen transport. For this purpose, hemoglobin is present in the cells. Hemoglobin is an assembly of four globular protein subunits that bind to each other. Each subunit contains a, so-called, heme, a Fe^{2+} contained in an organic molecule, to which oxygen can bind reversible during oxygen transport. Hemoglobin with bound oxygen is called oxyhemoglobin (HbO_2) and hemoglobin without bound oxygen is called deoxyhemoglobin (Hb). The oxygen saturation of hemoglobin, also called blood oxygenation level (Y), is defined as the fraction of the overall bounding sites that are saturated with oxygen,

$$Y = \frac{HbO_2}{Hb + HbO_2}. \quad (2.58)$$

The hemoglobin oxygen saturation is dependent on the oxygen partial pressure (pO_2) in

the blood and shows a (empirically found) sigmoid behavior [Stryer, 1998]

$$Y = \frac{(pO_2)^{2.8}}{(pO_2)^{2.8} + (p_{0.5})^{2.8}} \quad (2.59)$$

$p_{0.5}$ is the oxygen partial pressure at half oxygen saturation ($Y = 0.5$) and is equal to 3.6 kPa under normal physiological conditions. The typical shape of the oxygenation saturation curve of hemoglobin can be seen in Figure 2.12. The values emphasized in the figure represent normal values for arterial blood, mixed venous blood and the half oxygen saturation value for a healthy adult.

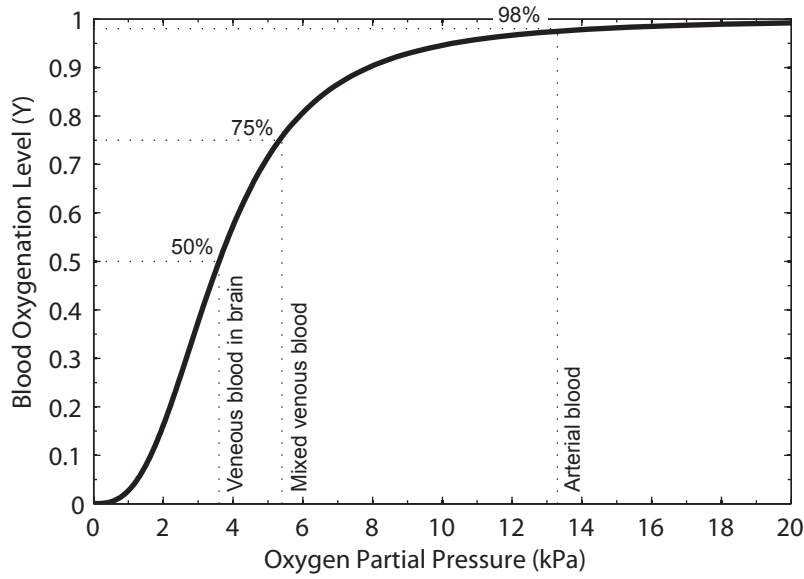


Figure 2.12. Oxygen saturation curve of hemoglobin. The oxygen saturation curve for a healthy grown up under normal physiological conditions ($pH = 7.4$, $T = 37^\circ\text{C}$). The marked values highlight the typical pO_2 values for arterial blood, mixed venous blood and venous blood in the brain.

The partial pressure of oxygen in air is approximately 20 kPa under normal conditions. This is reduced to about 16 kPa in the gas mixture found in the alveoli. Furthermore, in arterial blood, values of 13 kPa are found for healthy humans, which corresponds to an oxygen saturation of $97 - 98\%$. In the capillaries, the oxygen is released to the surrounding tissue. Hence, dependent on the oxygen demand of the respective tissue, the oxygen partial pressure in the veins drops to a value of $3.5 - 5.5 \text{ kPa}$, corresponding to an oxygen saturation of $50 - 75\%$.

2.3.3 Tissue Oxygen Consumption

The consumption of oxygen in the tissue can be quantified by the, so-called, metabolic rate of oxygen MRO_2 , which is defined as,

$$\text{MRO}_2 = \frac{O_2^{\text{consumption}}}{\text{tissue mass}} \quad \left[\frac{\text{mol/s}}{\text{g}} \right] \quad (2.60)$$

While the MRO_2 represents a measure for the absolute oxygen consumption, the oxygen extraction fraction (OEF) describes the relation between the oxygen consumption in the tissue and the oxygen delivery by the blood [Golay et al., 2001]. This important measure quantifies the oxygen utilization of the tissue and is defined as,

$$\text{OEF} = \frac{O_2^{\text{consumption}}}{O_2^{\text{delivery}}}. \quad (2.61)$$

The required oxygen is extracted from the blood in the capillaries. Hence, the OEF can be calculated as the difference in oxyhemoglobin content between arterial and venous blood,

$$\text{OEF} = \frac{HbO_{2,\text{arterial}} - HbO_{2,\text{venous}}}{HbO_{2,\text{arterial}}} = 1 - \frac{Y_{\text{venous}}}{Y_{\text{arterial}}}. \quad (2.62)$$

As previously mentioned, the oxygen saturation in arterial blood is approximately 100 %. Hence, the OEF can be approximated as,

$$\text{OEF} = 1 - Y_{\text{venous}}. \quad (2.63)$$

The OEF is organ dependent and varies with the stress state. In healthy myocardium and skeletal muscle, the OEF is about 0.4 to 0.6 during resting state. However, this can rise up to 0.9 in case of very high physical stress [Schmidt und Thews, 1995]. The OEF in a resting human brain is approximately 40 – 50 % [Hoogenraad et al., 1998]. Pathophysiological conditions can give rise to a considerable increase in the OEF, for instance if there is a deficiency in the concentration of dissolved oxygen in arterial blood (e.g., arterial hypoxemia) or if the oxygen demand is increased (e.g., in tumor).

The OEF and the MRO_2 are correlated by the absolute oxygen delivery,

$$\text{MRO}_2 = \text{OEF} \cdot \text{BF} \cdot HbO_{2,\text{arterial}}, \quad (2.64)$$

where BF represents the blood flow, and $HbO_{2,\text{arterial}}$ the oxyhemoglobin concentration of the arterial blood. Hence, during physical stress, the oxygen supply can be adjusted by either increasing the OEF or increasing the tissue perfusion.

2.3.4 Oxygenation Dependent Magnetic Properties of Blood

The physiological basic of the oxygen sensitive imaging is that the hemoglobin changes its permanent dipole moment dependent on the oxygenation status. In deoxygenated hemes, only five of the six coordinating positions of the Fe^{2+} -ion are occupied. As a result, unpaired electrons are present which give rise to a permanent magnetic dipole moment and, consequently, to paramagnetic properties. When oxygen is bound to the last coordinating position, the iron changes its electron configuration. Spin coupling is then energetically favorable and the heme becomes diamagnetic [Pauling und Coryell, 1936]. Macroscopically, the successive occupation of the coordinating positions appears as a continuous change of the magnetic susceptibility of the blood. The total magnetic

susceptibility of the blood is proportional to the magnetic susceptibility of the erythrocytes (χ_{ery}) and the blood plasma (χ_{plasma}),

$$\chi_{blood} = Hct \cdot \chi_{ery} + (1 - Hct) \cdot \chi_{plasma}. \quad (2.65)$$

The value of χ_{ery} depends linearly on the amount of oxygenated and deoxygenated hemoglobin [Spees et al., 2001],

$$\chi_{blood} = Hct \cdot (Y \cdot \chi_{ery,ox} + (1 - Y) \cdot \chi_{ery,deox}) + (1 - Hct) \cdot \chi_{plasma}. \quad (2.66)$$

where $\chi_{ery,ox}$ and $\chi_{ery,deox}$ denote the magnetic susceptibility of completely oxygenated and completely deoxygenated erythrocytes.

The volume susceptibility of blood plasma and fully oxygenated blood are approximately -9.05 ppm [Schenk, 1996] and -9.25 ppm [Weisskoff und Kiihne, 1992], respectively. Due to the small difference in the magnetic susceptibility, they can be approximated to be equal. With the susceptibility difference between fully oxygenated, and fully deoxygenated blood given by,

$$\Delta\chi_{do} = \chi_{ery,deox} - \chi_{ery,ox}, \quad (2.67)$$

Eq. 2.66 simplifies to,

$$\chi_{blood} = \chi_{ery,ox} + Hct \cdot (1 - Y) \cdot \Delta\chi_{do}. \quad (2.68)$$

Since the blood vessels generally are embedded in the tissue matrix, the susceptibility difference between parenchyma and the blood, $\Delta\chi$, is particularly interesting for *in vivo* measurements. Assuming that the susceptibility of the tissue is approximately the same as for fully oxygenated blood, Eq. 2.68, together with Eq. 2.63, gives the following expression for the susceptibility difference between the tissue and the veins,

$$\Delta\chi = Hct \cdot (1 - Y) \cdot \Delta\chi_{ox} \approx Hct \cdot OEF \cdot \Delta\chi_{do} \quad (2.69)$$

Under assumption that Hct and $\Delta\chi_{do}$ are known parameters, this relation reduces the estimation of the oxygen extraction to a measurement of the volume susceptibility of the venous blood. Two values of $\Delta\chi_{do}$ appears in the literature. Weisskoff und Kiihne [1992] measured a value of $4\pi \cdot 0.18 \text{ ppm}$ while later Spees et al. [2001] obtained a value of $4\pi \cdot 0.27 \text{ ppm}$. The Hct in small vessels is assumed to be 85 % of that in larger vessels [An und Lin, 2000].

III

Materials and Methods

3.1 Modeling blood vessels

3.1.1 Single Vessel in Homogeneous Tissue

A single capillary embedded in the tissue can be approximated as an infinitely long, homogeneous, magnetic cylinder (Figure 3.1) with a susceptibility difference $\Delta\chi$ to the surrounding medium. Such a cylinder causes a frequency shift $\Delta\omega$ dependent on the vessel orientation θ and the cylinder radius R [Ogawa et al., 1993],

$$\Delta\omega = \begin{cases} \delta\omega \frac{R^2}{r^2} \cos 2\varphi \sin^2 \theta & r > R \\ \delta\omega \frac{1}{3} (3 \cos^2 \theta - 1) & r < R. \end{cases} \quad (3.1)$$

Here r and φ are the distance and the azimuthal angle in a plane orthogonal to the cylinder, as shown in Figure 3.1, and the value $\delta\omega$ is the characteristic frequency shift,

$$\delta\omega = \frac{\Delta\chi\gamma B_0}{2}, \quad (3.2)$$

which characterizes the maximum field offset at the surface of the cylinder. The magnitude of the field offset at the surface of the cylinder will only be dependent on $\Delta\chi$, not on the cylinder radius. The spatial extent of the field distortion, however, is proportional to the radius. In Figure 3.2 (a) the field distribution around a magnetized cylinder orientated perpendicular to the magnetic field can be seen.

An analytical expression for the MR signal from a voxel containing a single cylinder, occupying a volume fraction ζ of the total voxel volume, has been derived by Yablonskiy und Haacke [1994] and is given by,

$$S(t) = S(0) \cdot \left(1 - \frac{\zeta}{1-\zeta} \cdot f_c(\delta\omega_\theta \cdot t) + \frac{1}{1-\zeta} \cdot f_c(\zeta \cdot \delta\omega_\theta \cdot t) \right), \quad (3.3)$$

where $\delta\omega_\theta$ is the characteristic frequency shift for the cylinder, here defined as,

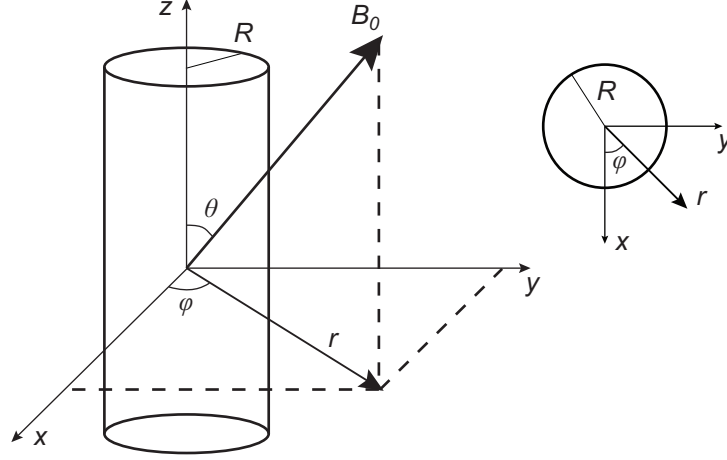


Figure 3.1. Single cylinder in an external magnetic field. (Figure adopted from Sedlacik [2007]

).

$$\delta\omega_\theta = \gamma \cdot \frac{\Delta\chi}{2} \cdot B_0 \cdot \sin^2 \theta, \quad (3.4)$$

and f_c is the characteristic function given by,

$$f_c(\varphi) = \int_0^1 du \cdot \frac{1 - J_0(\varphi \cdot u)}{u^2}, \quad (3.5)$$

where J_0 is the zeroth order Bessel function. This equation, however, is derived for single cylinder coaxial with a cylindrical voxel and is therefore not expected to be consistent with a measurement where square voxels are used. Sedlacik et al. [2007] performed numerical simulations and phantom measurements to investigate the signal behavior for arbitrary voxel geometry and found that even considering square voxels was not enough to simulate a real measurement. As mentioned in section 2.2.2.2, using a rectangular sampling window when sampling the k-space results in a sinc-shaped PSF, which has to be considered in the signal simulation.

An alternative mathematical expression for the MR signal from a voxel containing a single magnetized cylinder is given by [Sedlacik et al., 2007] (c.f. Eq. 2.26),

$$S(t) = \int_{\vec{r}} W(\vec{r}) \cdot S_0(\vec{r}) \cdot e^{-i \cdot \Delta\omega(\vec{r}) \cdot t} e^{-t/T2(\vec{r})} d\vec{r}, \quad (3.6)$$

where $W(\vec{r})$ is a weighting function used to describe the shape of the voxel. The weighting function for a cylindrical voxel, a square voxel, and a square voxel with PSF can be seen in Figure 3.2 (b-d). $S_0(\vec{r})$ is the local signal direct after excitation, which depends on the local spin density as well as on T1 and the sequence parameter used.

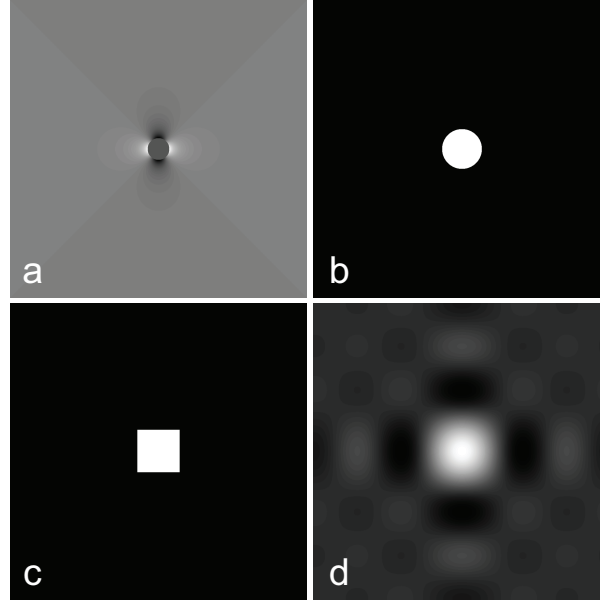


Figure 3.2. a) Field distribution around a magnetized cylinder oriented perpendicular to the main magnetic field, together with the weighting function (c.f. Eq. 3.6) for b) cylindrical voxel, c) quadratic voxel, and d) quadratic voxel with point spread function.

Partial Volume Effect

A partial volume effect arises when the imaging voxel contains more than one tissue type, e.g. tissues containing both water and fat, or blood vessels embedded in the tissue. The resulting voxel signal will then be a superposition of the signal from the different tissue types. For instance, the signal from a homogeneous voxel containing a single venous vessel, or a capillary network, occupying a volume fraction ζ , can be written as the sum of the signal originating from the intra and extra vascular space respectively,

$$\vec{S} = \zeta \cdot \vec{S}_{int} + (1 - \zeta) \cdot \vec{S}_{ext} \quad (3.7)$$

3.1.2 Vessel Network in Homogeneous Tissue

Analogous to using a single cylinder to simulate a single vessel, a collection of randomly oriented cylinders can be used to approximate a blood vessel network. When averaging over randomly spatially distributed and oriented cylinders, the histogram of the field distribution approaches a Lorentzian distribution and the signal decay is close to exponential. Since the extent of the field distortion is scaled down with the cylinder radius, the signal is independent on the size of the cylinders, and depends only on the susceptibility difference and the volume fraction occupied by the cylinders. However, this is only valid if spin motion during the experiment is neglected (e.i., no diffusion is present). The effect of diffusion is discussed in section 3.1.2.2.

The following model, derived by Yablonskiy und Haacke [1994], considers a macroscopically homogeneous voxel that does not contain large vessels or any other structures on the scale

of the voxel size. The statistical approach is justified by a vascular network formed by a large number of microscopic vessels inside the voxel. The capillary network is described as a set of statistically independent cylinders with random positions, orientations, and radii. The distributions of the cylinder positions and orientation are uniform. Furthermore, the smallness of the relative volume fraction of cylinders to the total voxel volume, ζ , is one of the basic assumptions of the statistical approach, and justifies the neglecting of intravascular signal contribution. In addition, the model is derived in the so-called static dephasing regime. The static dephasing regime assumes that the NMR signal dephasing due to susceptibility induced field inhomogeneities must occur before molecular diffusion averages out the phases. High magnetic fields, large $\Delta\chi$, and large vessels favor the static dephasing regime.

3.1.2.1 Statistical Averaging of Cylinders

The calculation of an analytical expression for the MR signal from a voxel containing a set of randomly distributed cylinders is based on statistical averaging. In this section, the derivation of the analytical expression is presented. The following equations were derived with reference to Yablonskiy und Haacke [1994]; Kiselev und Posse [1999]; Sedlacik [2007].

The MR signal from a voxel may be represented as,

$$S(t) = e^{-t/T_2} \int_{\vec{r}} S_0(\vec{r}) e^{-i \cdot \Delta\omega(\vec{r}) \cdot t} d\vec{r}, \quad (3.8)$$

where $S_0(\vec{r})$ is the basic signal fraction of each point, which depends on the local spin density as well as T_1 and the sequence parameters used, and $\Delta\omega(\vec{r})$ is the local deviation from the read out frequency. For a cylinder, $\Delta\omega(\vec{r})$ is given by Eq. 3.1. For the following derivations, only the external signal is considered, and a uniform spin distribution is assumed, in which case $S_0(\vec{r}) = S_{0,ext}$. The total influence on the signal from a given configuration of cylinders is the averaged effect over all N objects,

$$S_{ext}(t) = (1 - \zeta) \cdot S_{0,ext} \cdot e^{-t/T_2} \prod_{n=1}^N \langle \Psi_n \rangle. \quad (3.9)$$

In the static dephasing regime, the magnetization density as a function of time can be found from the Bloch equations,

$$\Psi = e^{-i \cdot \Delta\omega(\vec{r}) \cdot t}. \quad (3.10)$$

The averaged effect of each object on the external signal $\langle \Psi_n \rangle$ is calculated by integration over the orientation and position of the cylinder,

$$\langle \Psi_n \rangle = \int_0^\pi d\theta \frac{\sin \theta}{2} \int_0^{2\pi} d\varphi \int_R^\infty dr \frac{r}{A} \cdot e^{-i \cdot \Delta\omega(\vec{r}) \cdot t}. \quad (3.11)$$

The first integration represents the averaging over the cylinder tilt angle θ with isotropic distribution $(\sin \theta)/2$. Furthermore, the cylinder position is averaged by integration over

φ and r with uniform distribution $1/(A - \pi R^2)$ where A is the cross-sectional area of the voxel and πR^2 is the cross-sectional area of the cylinder [Kiselev und Posse, 1999]. The cylinder volume is excluded from the integration for calculation of the external signal. Equation 3.11 can be rewritten as,

$$\langle \Psi_n \rangle = 1 - \frac{\pi R^2}{A} \int_0^\pi d\theta \frac{\sin \theta}{2} \int_0^{2\pi} d\varphi \int_R^\infty dr \frac{r}{\pi R^2} \cdot \left(1 - e^{-i \cdot \Delta\omega(\vec{r}) \cdot t}\right). \quad (3.12)$$

If the volume fraction of the cylinder to the total volume is small,

$$\langle \Psi_n \rangle = 1 - \frac{\pi R^2}{A} \int_0^\pi d\theta \frac{\sin \theta}{2} \int_0^{2\pi} d\varphi \int_R^\infty dr \frac{r}{\pi R^2} \cdot \left(1 - e^{-i \cdot \Delta\omega(\vec{r}) \cdot t}\right) \approx 1, \quad (3.13)$$

Eq. 3.13 can be expressed as an exponential function,

$$\langle \Psi_n \rangle = \exp \left[-\frac{\pi R^2}{A} \int_0^\pi d\theta \frac{\sin \theta}{2} \int_0^{2\pi} d\varphi \int_R^\infty dr \frac{r}{\pi R^2} \cdot \left(1 - e^{-i \cdot \Delta\omega(\vec{r}) \cdot t}\right) \right] \approx 1. \quad (3.14)$$

Combining Eq. 3.14 with Eq. 3.9 yields the following signal equation,

$$\ln \left[\frac{S_{ext}}{(1 - \zeta) \cdot S_{0,ext} \cdot e^{-t/T^2}} \right] = -\zeta \int_0^\pi d\theta \frac{\sin \theta}{2} \int_0^{2\pi} d\varphi \int_R^\infty dr \frac{r}{\pi R^2} \cdot \left(1 - e^{-i \cdot \Delta\omega(\vec{r}) \cdot t}\right) \quad (3.15)$$

where $\zeta = \pi R^2 N/A$ is the total volume fraction occupied by the cylinders. Further calculations are enabled by the following substitution,

$$u = \frac{R^2}{r^2}, \quad (3.16)$$

which gives,

$$dr = -\frac{r^3}{2R^2} du. \quad (3.17)$$

Equation 3.15 may now be expressed as ($r = R \Rightarrow u = 1$, $r = \infty \Rightarrow u = 0$),

$$\ln \left[\frac{S_{ext}}{(1 - \zeta) \cdot S_{0,ext} \cdot e^{-t/T^2}} \right] = -\zeta \int_0^\pi d\theta \frac{\sin \theta}{2} \int_0^{2\pi} d\varphi \int_1^0 \frac{r^3}{-2R^2} du \frac{r}{\pi R^2} \cdot \left(1 - e^{-i \cdot \Delta\omega(\vec{r}) \cdot t}\right). \quad (3.18)$$

Using the variable substitution $r^4 = R^4/u^2$, the signal equation can be written as,

$$\ln \left[\frac{S_{ext}}{(1 - \zeta) \cdot S_{0,ext} \cdot e^{-t/T^2}} \right] = -\zeta \int_0^\pi d\theta \frac{\sin \theta}{2} \int_0^{2\pi} d\varphi \int_0^1 du \frac{1}{2\pi u^2} \cdot \left(1 - e^{-i \cdot \Delta\omega(\vec{r}) \cdot t}\right). \quad (3.19)$$

Hence, the external signal can be expressed as,

$$S_{ext} = (1 - \zeta) \cdot S_{0,ext} \cdot e^{-t/T^2} \cdot e^{-\zeta \cdot f_c(\delta\omega \cdot t)}, \quad (3.20)$$

where $f_c(\delta\bar{\omega} \cdot t)$ is the, so-called, characteristic function for a set of randomly distributed cylinders. The expression for this characteristic function has been further simplified by Yablonskiy und Haacke [1994] to allow faster numerical integration. The resulting equation is given by,

$$f_c(\delta\bar{\omega} \cdot t) = \frac{1}{3} \cdot \int_0^1 du \cdot (2 + u) \cdot \sqrt{1 - u} \cdot \frac{1 - J_0(1.5 \cdot \delta\bar{\omega} \cdot t \cdot u)}{u^2}, \quad (3.21)$$

where J_0 is the zeroth-order Bessel function. The, in the argument for f_c appearing, $\delta\bar{\omega}$ is the mean characteristic frequency shift for the cylinder system and is given by,

$$\delta\bar{\omega} = \frac{4\pi}{3} \gamma \cdot \Delta\chi \cdot B_0. \quad (3.22)$$

The signal equation in 3.20 does not have an analytical solution for a FID experiment. However, two distinct time periods of signal behavior have been identified. For short times, the signal amplitude was predicted to be Gaussian (quadratic exponential) suggesting a Gaussian field distribution inside the voxel. For long times the signal amplitude displays a linear exponential behavior, implying that the magnetic field in the voxel is Lorentz distributed;

$$S_t = (1 - \zeta) \cdot S_t(0) \cdot e^{-0.3 \cdot \zeta \cdot (\delta\bar{\omega} \cdot t)^2} \cdot e^{-t/T^2t} \quad |\delta\bar{\omega} \cdot t| < 1.5 \quad (3.23)$$

$$S_t = (1 - \zeta) \cdot S_t(0) \cdot e^{-\zeta(\delta\bar{\omega} \cdot t - 1)} \cdot e^{-t/T^2t} \quad |\delta\bar{\omega} \cdot t| > 1.5. \quad (3.24)$$

The characteristic time where the short-term asymptotic behavior changes to the long-term behavior is given by,

$$t_c = \frac{1.5}{\delta\bar{\omega}} \quad (3.25)$$

3.1.2.2 Diffusion

The previously mentioned tissue model is based on the assumption that spin motion due to self-diffusion, can be neglected during the experiment (static dephasing). This is valid when the spins can be assumed to remain in fixed positions and the field inhomogeneity they experience is time-invariant. The static dephasing assumption is valid if,

$$\delta\omega^{-1} << \frac{R^2}{D} \quad (3.26)$$

where $\delta\omega^{-1}$ is the characteristic signal decay time (c.f. Equation 3.2), R is the cylinder radius, and D is the apparent diffusion coefficient. D amount to about $207 \cdot 10^{-5} \text{ mm}^2/\text{s}$ for pure water at a room temperature of 21°C [Price et al., 1999]. A cylinder network with a susceptibility difference of 1 ppm to the surrounding media has a characteristic frequency shift of 200 Hz at 1.5 T (Eq. 3.2) and, hence, a characteristic signal decay time of 5 ms . This would correspond to a characteristic radius of $3.2 \text{ }\mu\text{m}$. To assure the static dephasing

regime, the cylinder radius has to be much larger than this, which is the case if the radius is on the order of hundreds of microns.

The measured diffusion coefficient in human brain tissue is smaller than that of free water due to the presence of cell walls and membranes. As a result of those barriers, the movement of water molecules cannot be described as free diffusion, and the measured diffusion coefficient is called apparent diffusion coefficient (ADC). The self-diffusion of water is about $80 \cdot 10^{-5} \text{ mm}^2/\text{s}$ for gray and $64 - 107 \cdot 10^{-5} \text{ mm}^2/\text{s}$ for white brain matter [Le Bihan et al., 1995]. The range of white matter diffusion coefficients results from the anisotropic diffusion, with higher diffusion along fibers and lower perpendicular to them [Hirsch et al., 1999]. Due to the lower diffusion coefficients *in vivo*, the static dephasing regime can be assumed for vessels much smaller than $100 \mu\text{m}$. It has been speculated that static dephasing under *in vivo* conditions can be assumed for a vessel radius down to $10 \mu\text{m}$ for $1.5 T$ [Yablonskiy und Haacke, 1994]. However, a comparison with Monte Carlo simulations show that this equality rather should be a simple inequality, $R > 10 \mu\text{m}$, and Kiselev und Posse [1999] concluded that the model can be applied with a reasonable accuracy to a radius of $25 \mu\text{m}$. The smallest capillaries in the brain have a radius of $6 - 8 \mu\text{m}$ [Duvernoy et al., 1981]. Boxerman et al. [1995] showed by means of simulations that diffusion would cause a reduction of the relaxation rate of about 15 % for a $5 \mu\text{m}$ vessel. Hence, the part of the capillaries with small radii causes a systematic underestimation of $\Delta\chi$, if this is not accounted for. An exact estimation of the uncertainties caused by diffusion *in vivo* has to consider the true amount of small vessels.

Kiselev und Posse [1999] extended the previously described tissue model to include diffusions effects. Allowing for molecular diffusion, the Bloch-Torrey equation has to be considered,

$$\frac{\partial \Psi}{\partial t} = D \Delta \Psi - i \Delta \omega(\vec{r}) \Psi. \quad (3.27)$$

In case of slow diffusion an approximate solution to Eq. 3.27 is given by [Kiselev und Posse, 1999],

$$\Psi = e^{-i \cdot \Delta \omega(\vec{r}) \cdot t - \frac{D}{3} [\nabla(\Delta \omega(\vec{r}))]^2 \cdot t^3}. \quad (3.28)$$

Statistical averaging of this function yields a characteristic function that not only depends on $\delta\omega \cdot t$ but on an additional, dimensionless parameter λ that in turn depends on the diffusion coefficient D and the cylinder radius R ,

$$\lambda = \frac{D}{R^2 \cdot \delta\omega}. \quad (3.29)$$

With the signal expression given by Eq. 3.20, the characteristic function, including diffusion, is given by,

$$f_c(\delta\omega \cdot t; \lambda) = \int_0^\pi d\theta \frac{\sin \theta}{2} \int_0^1 \frac{du}{u^2} \cdot \left[1 - \exp\left(\frac{4}{3} \lambda (\delta\omega \cdot t)^3 u^3 \sin^4 \theta\right) J_0((\delta\omega \cdot t) u \sin^2 \theta) \right], \quad (3.30)$$

where J_0 is the zero-order Bessel function. The, in the argument for f_c appearing, $\delta\omega$ is the characteristic frequency shift given by Eq. 3.2. The major problem using this model

for *in vivo* experiments is that the vessel radius distribution inside the voxel has to be known.

The effect of diffusion in a spin echo experiment is shown exemplary in Figure 3.3. The diffusion causes a decrease of the maximal signal intensity as well as a shift of the spin echo toward shorter echo times. The effect is not very pronounced for the FID signal. Hence, the effect can be reduced by choosing short echo times.

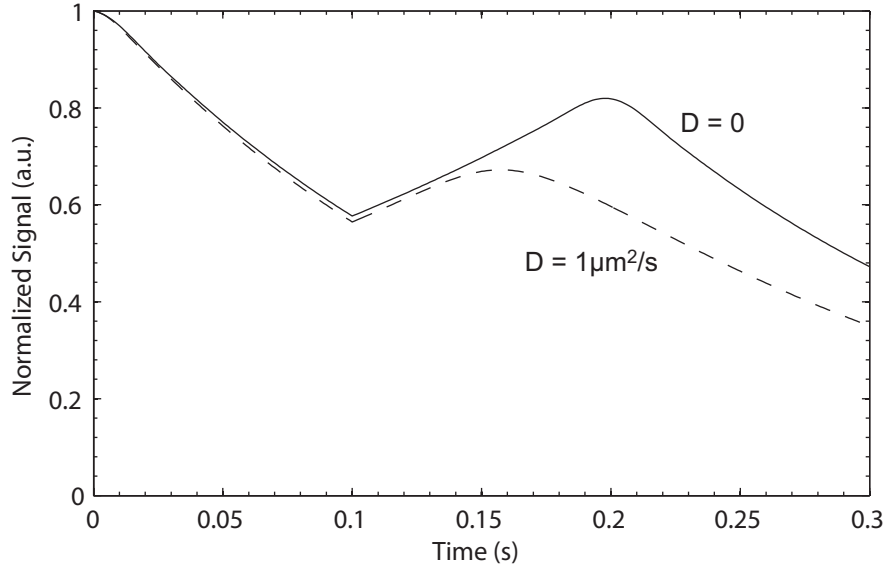


Figure 3.3. Signal time course in a spin echo experiment from a voxel containing a microvascular network with consideration of diffusion. In presence of diffusion (dashed line) the position of the spin echo is shifted toward shorter echo times and the maximal signal intensity at the spin echo is decreased compared to the case where no diffusion is present (solid line). The effect is more pronounced after the spin echo than for the FID part of the signal.

3.2 Measurement Techniques

3.2.1 MR Scanners

The measurements were carried out on two Siemens MR scanners situated at the German Cancer Research Center (DKFZ) in Heidelberg, Germany. One scanner has a magnetic field strength of 1.5 T (Magnetom Avanto, Siemens Medical Solutions, Erlangen) and the other has a magnetic field strength of 3 T (Magnetom Trio, Siemens Medical Solutions, Erlangen). All systems share the same sequence-developing environment named IDEA (Integrated Development Environment for Applications).

3.2.2 MR Sequences

The two fundamental types of MR pulse sequences, the spin echo and the gradient echo, were described in section 2.2.3. In this section, the specific sequences used in this work are presented. The sequences used in this work were either provided by Siemens or developed using a C++ based development environment provided by the MR device manufacturer (IDEA, Siemens, Erlangen).

3.2.2.1 CPMG

The standard technique to measure the R_2 relaxation rate in the presence of diffusion and magnetic field inhomogeneities is to use a Carr-Purcell-Meiboom-Gill (CPMG) sequence [Carr und Purcell, 1954; Meiboom und Gill, 1958]. The CPMG sequence is a spin echo sequence consisting of a 90° RF pulse followed by an echo train induced by successive 180° pulses. A 90° phase shift between the 90° and the subsequent 180° pulses is included to minimize effects of pulse imperfections.

3.2.2.2 Diffusion-weighted EPI

Diffusion-weighted images can be obtained by implementation of, so-called, diffusion gradients into the sequence. The diffusion gradients are a pair of bipolar gradients switched before the signal readout. The process of diffusion-weighted imaging is described briefly below.

After excitation, all spins precess with the same frequency and have the same phase. During the switching of the first diffusion gradient, the spins located at different positions experience a different magnetic field, and therefore precess with different frequencies. After the gradient is switched off, again all spins precess with the same frequency, but they now have different phases. For stationary spins, the switching of a second gradient with inverted polarity results in a total rephasing, i.e., all spins once again have the same phase. However, if an incoherent motion of the water molecule is present during the time between the gradients, the molecule experiences another magnetic field during the second gradient switching and no complete rephasing is achieved. Hence, a diffusion-weighted signal can be obtained.

The amount of diffusion weighting is determined by the strength and the duration of the diffusion gradients as well as on the distance between them. In order to measure the ADC, usually two scans are performed, one with diffusion weighting and one without. By making a linear regression to the logarithm of the normalized signal as a function of the strength of the diffusion weighting (so-called b-value), the ADC can be found from the slope.

Diffusion gradients are commonly implemented in an EPI sequence [Mansfield, 1977]. The important feature of the EPI sequence is the extremely short measurement time which helps to reduce errors due to pulsation effects. During an EPI scan, the whole k-space is sampled after one single RF excitation. After the excitation, an outer point in k-space is reached by switching of one gradient in frequency direction and one gradient in phase

direction. After the first k-space line is read, a small phase gradient is used to reach the next line in k-space which is read “backwards”, using a read out gradient with inverted polarity. This procedure continues until the whole k-space is sampled. The effective TE is defined as the time when the k-space center is sampled.

3.2.2.3 Gradient Echo Sampled Spin Echo (GESSE)

In section 3.1.2, a theory describing the MR signal over time as a function of the frequency shift induced by deoxygenated blood in a capillary network embedded in a tissue matrix was presented. In order to estimate the frequency shift (i.e., the tissue oxygenation), knowledge of the MR signal intensity as a function of time in the vicinity of a spin echo is required. This can be achieved by a, so-called, gradient echo sampled spin echo (GESSE) sequence as proposed by Yablonskiy und Haacke [1997]. The GESSE sequence is a slightly changed version of the GESFIDE (Gradient Echo Sampling of FID and Echo) presented by Ma und Wehrli [1996], which can be used for simultaneous measurement of $R2$ and $R2^*$. The GESSE sequence is a standard spin echo sequence combined with a multi contrast gradient echo sequence, as shown in Figure 3.4. A large number of successive gradient echoes are generated before and after the echo time of the single spin echo sequence, resulting in a series of image contrasts, each with different echo time, which renders the rephasing and dephasing parts of the spin echo signal. The refocusing of the magnetization

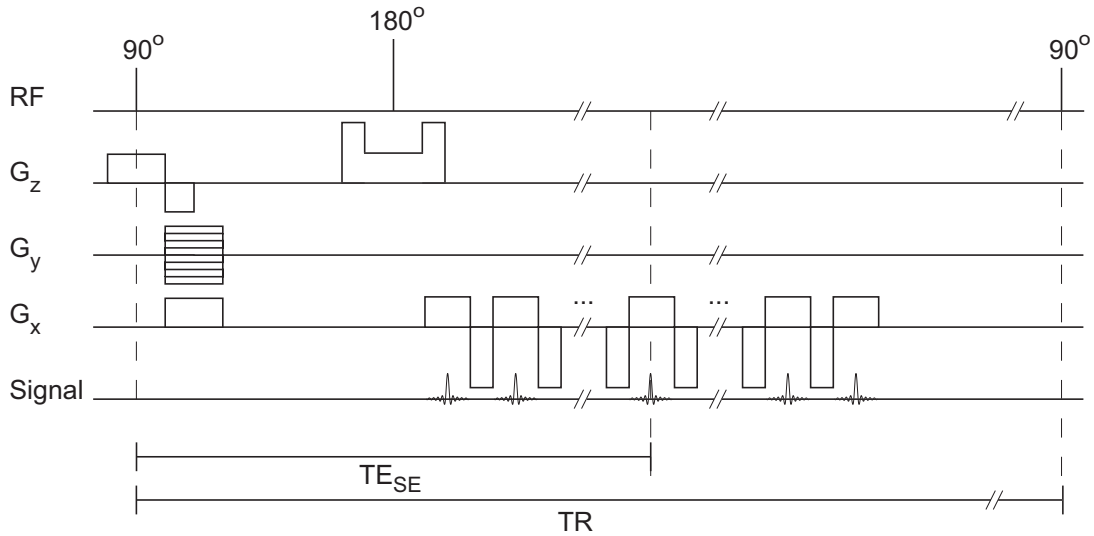


Figure 3.4. GESSE Sequence. Exemplary scheme of the implemented gradient echo sampled spin echo sequence (GESSE). The spin echo occurs at a time TE_{SE} which coincide with one of the gradient echoes.

using a 180° -pulse, however, is not always complete. An incomplete refocusing entails a mixing of $R2^*$ and $R2$ for the signal development between the refocusing pulse and the spin echo [Ma und Wehrli, 1996], which is not desirable since the deciphering of the oxygenation is dependent on a clear separation of those two relaxation rates. Therefore, spoiler gradients, that dephase the $R2^*$ -component, are switched in slice selection direction

before and after the 180° pulse.

A mono directional readout, i.e., always with the same gradient polarity, is used in order to minimize effects of phase shifts in k-space [Haacke et al., 1999]. The minimum time interval between two adjacent echoes depends on the maximum gradient strength (G_{max}) and maximum slew rate for the system used, as well as the resolution (Δx) and bandwidth (BW) chosen for the measurement [Bongers, 2004],

$$\Delta TE_{min} = \frac{1}{BW} + \frac{1}{\gamma \cdot \Delta x \cdot G_{max}} + \frac{3G_{max}}{\text{SlewRate}} + \frac{BW}{\gamma \cdot \Delta x \cdot \text{SlewRate}}. \quad (3.31)$$

To realize a smaller ΔTE while keeping the resolution constant, the bandwidth has to be increased resulting in a poorer SNR.

3.2.3 Measurement Phantoms

3.2.3.1 Single Cylinder Phantoms

Custom-built phantoms (Figure 3.5) with two different string diameters ($245 \mu m$ and $194 \mu m$) were used for the single string measurements. Four phantoms with 1, 3, 5, and, 7 g/l $NiSO_4 \cdot 6H_2O$ and 5 g/l $NaCl$ were constructed.

All single string scans were performed with a gradient echo sampled spin echo (GESSE) sequence (chapter 3.2.2.3). Scan parameters can be seen in Table 3.1 together with the string data. All measurements were performed at the 1.5 T scanner using a small loop coil and with $TR = 1000 ms$, and a B_0 to string angle of $\pi/2$. A 256×256 matrix and a slice thickness of 3 mm were used for both string diameters.



Figure 3.5. Single String Phantom. The singles string phantoms are constructed of polyamide strings, with two different string diameters ($245 \mu m$ and $194 \mu m$), in a $NiSO_4$ solution

Table 3.1. Sequence parameters used for the single string phantom measurements. ζ is the calculated relative volume fraction for each string diameter.

String diameter (μm)	FOV (mm)	ΔTE (ms)	Bw (Hz/px)	ζ (%)
245	100	6.0	340	30.9
194	82	7.0	280	28.8

3.2.3.2 Cylinder Network Phantoms

A measurement phantom used to investigate the practical influence of diffusion in a cylinder network should reflect the properties of the model, i.e., statistically distributed and randomly oriented cylinders in a homogeneous medium. The model proposed by [Yablonskiy und Haacke, 1994] predicts a signal that is independent on the capillary radius. Schröder [2005] showed in phantom experiment that this is not true for small radii. One probable explanation is that diffusion plays an important role in the signal formation, especially for small radii. In order to investigate the diffusion effect further, measurement phantoms were constructed which aimed to simulate capillary networks of different vessel radii. The phantoms are a further development of the, in this working group, previously developed phantoms, and is constructed of randomly coiled polyamide strings immersed in a $NiSO_4$ solution. Monofilamentous polyamide strings were used (Polyamide 6-6.6 black, Fa. Krahmer GmbH, Buchholz). The string diameter was in the range of $27 - 245 \mu m$ which covers the largest part of the capillary diameters that exist *in vivo*. The string was immersed in a solution composed of $NiSO_4 \cdot 6H_2O$ and $NaCl$. $NiSO_4$ was chosen due to its paramagnetic properties. Polyamide is slightly more diamagnetic than water and adding $NiSO_4$ to the water results in a more paramagnetic solution. Hence, the higher the $NiSO_4$ concentration, the larger susceptibility difference between the strings and the solution. Furthermore, the T2 of the $NiSO_4$ solution corresponds roughly to that *in vivo*, at a susceptibility difference expected *in vivo*.

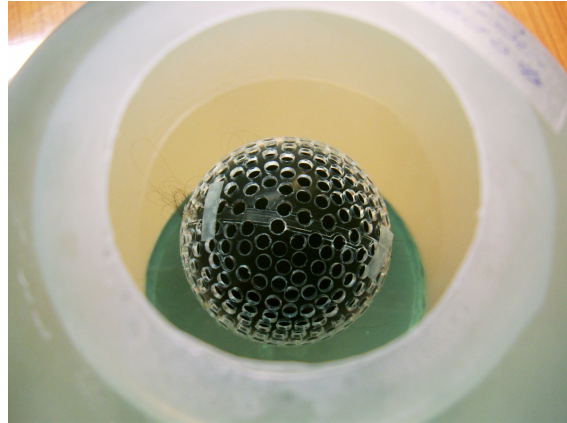


Figure 3.6. String network phantom. The spherical compartment contains a randomly coiled polyamide string of a certain diameter. The whole phantom is filled with a $NiSO_4$ solution.

Since the method aims to measure the relatively small field inhomogeneities that are caused by the strings, it is very important to avoid background field inhomogeneities. The phantoms were constructed using a completely spherical geometry, which prevent distortions of the magnetic field inside the probe. Hollow plastic balls with a diameter of 150 mm were used as outer containers. Smaller plastic balls, with a diameter of 48 mm , were perforated, to allow inflow of liquid, and used as an inner containers. The inner container was filled with randomly coiled polyamide stings (Figure 3.6). The string radius, the volume fraction of the inner container occupied by polyamide strings and the $\text{NiSO}_4 \cdot 6\text{H}_2\text{O}$ concentration in respective phantom are presented in Table 3.2.

Table 3.2. String network phantom specifications.

Phantom	String diameter	Volume fraction	Concentration NiSO_4
I	$27\text{ }\mu\text{m}$	2 %	4.00 g/l
II	$63\text{ }\mu\text{m}$	3 %	3.75 g/l
III	$89\text{ }\mu\text{m}$	5 %	3.00 g/l
IV	$245\text{ }\mu\text{m}$	3 %	3.00 g/l

When the phantoms are filled with the NiSO_4 solution, air bubbles get trapped in the string filled compartments. Those bubbles cause unwanted magnetic field inhomogeneities if present, and must be removed. The removal is achieved in a degassing process where the phantom is placed in strong vacuum during a certain time period. The higher the partial vapor pressure the more gas can be solved in a liquid. By lowering of the atmospheric pressure, the thermal equilibrium at the boundary between liquid and air is disturbed. To restore it, solved gases go up in the gas phase. Since those continuously are pumped of, a complete degassing of the liquid can be achieved.

For the phantom measurements with the string network phantoms, two different GESSE scans were used. Both scans have a distance between two adjacent echoes of 1.6 ms and a TR of 2000 ms . The first sequence variant has the spin echo positioned at the 7th echo with an echo time of 37 ms and the second sequence variant has the spin echo positioned at the 16th echo with an echo time of 68 ms . Measurements were performed at both 1.5 T and 3 T using a standard head coil. All are sequence parameters are shown in Table 3.3 and Table 3.4.

Table 3.3. Summary of the GESSE sequences used for the network phantom measurements

Sequence variant	Number of Spin echo	Echo Time (ms)	ΔTE (ms)	Number of Echoes
1	7	37	1.6	32
2	16	68	1.6	32

Table 3.4. Sequence parameters used for all network phantom measurements

Field of View (mm)	192
Matrix	64×64
Resolution (mm ²)	3.0×3.0
Slice Thickness (mm)	6
TR (ms)	2000
Bandwidth (Hz/pixel)	1530
Number of Acquisitions	16
Measurement Time (minutes)	34 : 08

3.2.3.3 Calculation of the susceptibility of $NiSO_4$ solutions

In Schenk [1996], a reference value for the susceptibility of $NiCl_2$ in water can be found. This value can be used to calculate the expected susceptibility of the $NiSO_4 \cdot 6H_2O$ solutions used during the measurements in this work. The mole mass and density of $NiCl_2$ and $NiSO_4$, anhydrous and hexahydrate, can be seen in Table 3.5.

The magnetic susceptibility of an aqueous solution with 23.15 wt. % $NiCl_2$ at 20° is 116 ppm and the density of such a solution is 1.26 g/cc. Hence, there are $1.26 \cdot 0.2315 = 0.29$ g/cc $NiCl_2$ in the solution. Using the mole masses of $NiCl_2$ and $NiCl_2 \cdot 6H_2O$ from Table 3.5, the corresponding concentration of $NiCl_2 \cdot 6H_2O$ can be calculated,

$$NiCl_2 \cdot H_2O \text{ (g/l)} = \rho_{NiCl_2} \text{ (g/cc)} \frac{M_{NiCl_2 \text{ hexahydr}} \text{ (g/mol)}}{M_{NiCl_2 \text{ anhydr}} \text{ (g/mol)}} \cdot 1000. \quad (3.32)$$

A specific concentration of $NiCl_2 \cdot 6H_2O$ can be recalculated into concentration of $NiSO_4 \cdot 6H_2O$ using,

$$C_{NiCl_2} \text{ (g/l)} = \frac{C_{NiSO_4} \text{ (g/l)}}{M_{NiSO_4} \text{ (g/mol)}} \cdot M_{NiCl_2} \text{ (g/mol)}. \quad (3.33)$$

Using the susceptibility of water of -9.04 ppm, the susceptibility of aqueous solutions with different $NiSO_4 \cdot 6H_2O$ concentrations can be calculated. Calculated susceptibilities can be seen in Table 3.6.

Table 3.5. Mole mass and density of some substances.

Substance	Molecular weight (g/mole)	Density (g/cc)
$NiSO_4 \cdot 6H_2O$	262.85	2.07
$NiSO_4$	154.75	3.68
$NiCl_2 \cdot 6H_2O$	237.68	1.92
$NiCl_2$	129.60	3.55

Table 3.6. Calculated susceptibilities of solutions with different $NiSO_4 \cdot 6H_2O$ concentrations.

$[NiSO_4 \cdot 6H_2O]$ (g/l)	χ (ppm)
1.0	-8.82
2.0	-8.61
3.0	-8.40
4.0	-8.18
5.0	-7.97

3.3 Evaluation Techniques

3.3.1 Macroscopic Inhomogeneity Correction

The modeling of the blood vessels described in section 3.1 assumes that deoxyhemoglobin is the only source of magnetic field inhomogeneities that influence the MR signal formation (except the fluctuating microscopic field inhomogeneities that causes T2 relaxation). In general, this is not true. Additional macroscopic field inhomogeneities can be present due to imperfections in the main magnetic field, or can be caused by tissue-air interfaces. Those inhomogeneities will affect the signal as well, and may influence the parameter quantification if they are not properly acknowledged.

The total magnetic field can be calculated as the sum of the magnetic field caused by the deoxyhemoglobin (B_{Hb}) and the macroscopic field (B_{macro}),

$$B_s = B_{Hb} + B_{macro} \quad (3.34)$$

The signal equation (cf. Eq. 2.30) is then,

$$S(t) \propto \int_V M_{xy}(t_0) e^{i\gamma \cdot (B_{Hb}(\vec{r}) + B_{macro}(\vec{r})) \cdot t} \cdot e^{-t/T_2} d\vec{r}. \quad (3.35)$$

Because of the difference in spatial scale of the macroscopic and mesoscopic field inhomogeneities, the total signal can be represented as a product of the signal that would exist in the absence of macroscopic field inhomogeneities, multiplied with a function $F(t)$, which represents contributions to the signal attenuation caused by macroscopic field inhomogeneities,

$$F(t) = \frac{1}{V} \int_V e^{i\gamma \cdot B_{macro}(\vec{r}) \cdot t} \cdot d\vec{r}. \quad (3.36)$$

Hence, if the magnetic field distribution inside the voxel is known, Eq. 3.36 can be solved, and the macroscopic part of the signal can be removed.

As mentioned in section 2.1.6, the measured signal can be expressed as a complex quantity (cf. Eq. 2.25),

$$M_{xy}(\vec{r}, t) = |M_{xy}(\vec{r}, t)| \cdot e^{i\phi(\vec{r}, t)}, \quad (3.37)$$

where t is the time from the center of the excitation pulse. The phase, ϕ , is linearly related to the intra-voxel mean magnetic field [Bonny et al., 2000],

$$\phi(\vec{r}, t) = -\gamma \Delta B(\vec{r}) \cdot t + \phi_0(\vec{r}) = -\gamma (B_{macro}(\vec{r}) - B_{rec}) \cdot t + \phi_0(\vec{r}), \quad (3.38)$$

where ϕ_0 is the phase at $t = 0$, and γB_{rec} is the readout frequency used for detection. Hence, sampling of the time course of the complex MR signal can provide information about the field inhomogeneities, $B_{macro}(\vec{r})$.

When the inhomogeneities are small compared to the main magnetic field, the macroscopic field can be described as a Taylor series,

$$B_{macro}(r) = B_{macro}^0 + \frac{\partial B_{macro}(r_0)}{\partial r} (r - r_0) + \frac{1}{2} \frac{\partial^2 B_{macro}(r_0)}{\partial r^2} (r - r_0)^2 + \dots \quad (3.39)$$

The constant term leads to a constant phase in the measured signal, but does not cause any phase dispersion. The higher order terms, however, give rise to a dephasing of the signal. The main contribution comes from the linear term, and therefore the macroscopic field inhomogeneities can be modeled as a linear field across the voxel of interest. Such a gradient causes a sinc-shaped signal decay (here in x-direction) [Haacke et al., 1999],

$$F_x(t) = \text{sinc}(\gamma \cdot G_{macro,x} / 2 \cdot \Delta x \cdot TE). \quad (3.40)$$

B_{macro} can be estimated by means of linear regression to the phase evolution over time,

$$B_{macro} = \frac{1}{\gamma} \frac{d\phi}{dt}. \quad (3.41)$$

This method, where several echo times are used and the phase difference between the measurements are considered, instead of using the phase of one measurement, reduces the influence of hardware imperfections such as gradient delays or phase errors of array coils.

Gradients in all spatial directions can be calculated by fitting the B_{macro} map for each voxel in the original sequence into a polynomial model taking also the quadratic terms into consideration. The total correction function is then the product of the correction functions (Eq. 3.40) for all three spatial dimensions,

$$F_{tot} = F_x \cdot F_y \cdot F_z, \quad (3.42)$$

using the calculated gradients and the dimensions and echo times for the original sequence.

The distribution $B_{macro}(\vec{r})$ (c.f. Eq. 3.36) inside a voxel in the GESSE measurement was estimated using phase maps acquired with a high-resolution 3D multi echo GRE pulse sequence, where the signal loss due to macroscopic inhomogeneities can be assumed negligible. The standard technique for multi echo acquisitions (e.i., T2* GRE [Gati et al., 1997]) generally uses both positive and negative read out gradients. The presence of macroscopic field gradients, however, would differently distort images collected in the presence of positive and negative readout gradients [Schmitt et al., 1998].

The signal was sampled only in the presence of positive readout gradients to avoid phase errors caused by the alternation of the read gradient polarity. B_{macro} was estimated by

means of linear regression to the phase evolution over time for each voxel of the GRE images. Gradients in all spatial directions were calculated by fitting the B_{macro} map for each GESSE voxel into a quadratic polynomial model using base functions x , y , z , xy , yz , xz , $x^2 - y^2$, and $z^2 - x^2 - y^2$. The correction function was calculated according to Eq. 3.42, using the calculated gradients and the dimensions and echo times for the GESSE sequence. The echo times for the 3D GRE sequence were selected so that fat and water were in phase. For both $3T$ and $1.5T$ systems, 5 echoes were used with a time difference between two subsequent echoes (ΔTE) of $9.52ms$. Since the slice thickness typically is much larger than the in-plane resolution, the largest inhomogeneity effect will be found in slice selection direction. In order to perform inhomogeneity correction in slice selection direction, the slice thickness has to be accurately known. The requested slice thickness was monitored using slice profile images, acquired with a spin echo sequence where the readout analog-to-digital converter is placed along the slice select direction.

The discrete and wrapped nature of phase images can spoil the reconstruction of the field inhomogeneity and gradient maps. Hence, a 3D phase unwrapping [Abdul-Rahman et al., 2007] was applied to all acquired 3D data sets. Furthermore, since the signal is sampled at certain echo times with a constant echo distance ΔTE , the measurable range of frequency offsets is limited by $\pm(2 \cdot \Delta TE)^{-1}$ (cf. Eq. 2.52 and 2.53). The assumption that this bandwidth is enough to map the magnetic field inhomogeneities without aliasing is equivalent to considering that the signal phase jump between two adjacent echoes is less than π . Since it cannot be assumed that this is always the case, phase unwrapping of the phase-time course was performed, using the built in MATLAB function *unwrap*.

3.3.2 Single Cylinder Measurements

Since the integral in Eq. 3.6 does not have an analytical expression for other voxel geometries than cylindrical (Eq. 3.3), numerical simulations have to be performed. The signal of a MR voxel containing a single cylindrical vessel can be numerically simulated using a large matrix where every matrix element, n , represents a small spin packet. The value of $\Delta\omega(\vec{r})$ can be calculated for every matrix point using Eq. 3.1. The complex values of the matrix points are then added together to get the total signal from the voxel at a certain echo time TE ,

$$S(TE) = \sum_{n=1}^N W_n \cdot S_{0,n} \cdot e^{-i\Delta\omega_n \cdot TE - TE/T_{2,n}}. \quad (3.43)$$

According to the theory, the cylinder has to be positioned in the center of the voxel. This may not always be the situation in a real measurement. To solve this problem, Sedlacik et al. [2007] proposed a method where a phase gradient is applied in the k-space before reconstruction. According to the Fourier transform shift theorem, a shift in one domain leads to a linear phase change in the other domain, and vice versa. Hence, a subvoxel shift can be achieved that positions the cylinder in the center of the voxel. The shift is applied until the symmetry of the signal in the neighboring voxels indicates that the string is located in the center of the voxel.

To obtain the susceptibility difference between the cylinder and the surrounding medium,

the numerical simulation of the signal behavior for a square voxel with PSF is fitted to the measured signal curve in an iterative manner. The measured signal is normalized to a homogeneous area near the evaluated voxel prior to the curve fitting in order to eliminate the effect of T_2 decay. Hence, T_2 is set to one for all matrix elements. Furthermore, S_0 is set to one outside the cylinder and to zero inside the cylinder. The SNR for each measurement point is estimated as the standard deviation of the signal in the homogeneous ROI, and used as weighting factors during the curve fitting procedure. All evaluations were performed using the MATLAB *lsqcurvefit* function and self-written MATLAB code. A non-linear Levenberg-Marquardt algorithm was used for optimization. No corrections for the angle were performed subsequent to the measurements, hence all signals were computed for a vessel oriented perpendicular to \vec{B}_0 ($\theta = 90^\circ$). Due to the restricted spatial resolution of the whole-body scanner, the smallest string diameter examined with this method was $194 \mu m$.

3.3.3 Cylinder Network Measurements

In order to obtain a quantitative measure of Y , $\delta\omega$ has to be extracted from Eq. 3.20. The characteristic function that appears in the equation does not have an analytical solution. Hence, one has to use either the analytical expressions that are available for the asymptotic forms of the characteristic function or numerical methods in order to extract the desired parameter.

3.3.3.1 Analytical method

One technique to estimate $\delta\omega$ is to use the analytical expressions that exist for the asymptotic forms of Eq. 3.20. Combining Eq. 2.32 with Eq. 3.24 yields the following expression for the reversible relaxation rate ($R_2' = 1/T_2'$),

$$R_2' = \zeta \cdot \delta\bar{\omega} = \zeta \cdot \frac{4\pi}{3} \Delta\chi \cdot B_0. \quad (3.44)$$

Hence, there is a direct relationship between the reversible relaxation rate and the induced frequency shift. The latter part of the equation above, obtained by using the expression for $\delta\bar{\omega}$ given by Eq. 3.22, displays R_2' as a function of $\zeta \cdot \Delta\chi$. Thus, once R_2' and ζ are known, the mean susceptibility difference is known and Y can be calculated according to Eq. 2.69.

Both R_2' and ζ can be estimated if the MR signal-time course is sampled using the GESSE sequence (section 3.2.2.3). By measuring the long time asymptotic forms, before and after a spin echo, respectively, R_2' can be estimated. In case of a spin echo, the argument in Eq. 3.24 has to be replaced by $t - TE$. Using R_2' as above, the signal equation for the long time asymptotic form can be written as,

$$S_t = (1 - \zeta) \cdot S_t(0) \cdot e^\zeta \cdot e^{-R_2' \cdot |t - TE|} \cdot e^{-R_2 \cdot (t - TE)}. \quad (3.45)$$

This depicts that the signal decay in the vicinity of a spin echo is dependent on the phase dispersion due to magnetic inhomogeneities while the signal amplitude at the spin echo is

thoroughly unaffected by those inhomogeneities. Before the spin echo, the reversible and irreversible relaxation counteracts each other whereas after the spin echo their effect is adding up. Consequently, measuring the relaxation rate before the spin echo would give a measure of $R2_t - R2'$ and measuring the relaxation rate after the spin echo would give a measure of $R2_t + R2'$. When combining those two relaxation rates, both $R2_t$ and $R2'$ can be calculated. Furthermore, the dependence of the long time behavior on ζ allows one to extract information on the volume fraction occupied by the susceptibility inclusions in a tissue matrix. By placing $t = \text{TE}$ into Eq. 3.45, the volume fractions of the susceptibility inclusions can be found as,

$$\zeta = \ln(S_{\text{extrapolated}}(\text{TE}_{\text{SE}})/S(\text{TE}_{\text{SE}})). \quad (3.46)$$

When both $R2'$ and ζ are known, Y can be calculated according to,

$$Y = 1 - \frac{3}{4\pi\gamma B_0} \cdot \frac{R2'}{\zeta} \cdot \frac{1}{\Delta\chi_{do}} \quad (3.47)$$

However, fitting the signal time course before and after the spin echo independently, even though the parameters have a clear dependence can give rise to unnecessary unstable parameter estimation. Bongers [2004] proposed a modified version of the analytical approach where the two asymptotes is fitted simultaneously. Using this combined method, one fit parameter can be eliminated and the true extrapolation is avoided, which make the method more robust. Bongers [2004] found that for the same SNR, the combined method reduces the parameter error by 30 – 50 % compared to the independent analytical method.

3.3.3.2 Numerical method

An alternative approach to the analytical method of using the asymptotic forms of the signal is to numerically calculate the signal and, in an iterative manner, fit the sampled data to the whole signal model. By doing so, no restriction to the simplified two-compartment model is required, but models that are more realistic can be used since analytical expressions for the long and short time asymptotes are no longer needed. He et al. [2008] extended the previously described model to incorporate the multi-component MR behavior of brain tissue. The extended model includes contributions from parenchymal tissue (gray and white matter), cerebrospinal fluid (CSF), or interstitial fluid (ISF) and intravascular blood.

The parenchymal signal is the signal given by Eq. 3.20 but now with $\zeta = \kappa + \zeta'$ where κ and ζ' is the signal fraction from ISF/CSF and blood at the spin echo, respectively.

The extra cellular fluid (ISF and CSF) might have a frequency (Δf) and phase (φ) shift from the parenchyma signal and hence this part of the signal is given by,

$$S_e(t) = \kappa \cdot S_0 \cdot e^{-R2_e \cdot t - 2\pi i \cdot \Delta f \cdot t - i\varphi}, \quad (3.48)$$

where $R2_e$ is the transverse relaxation rate for ISF/CSF.

The intravascular blood signal can be modeled as [Sukstanskii und Yablonskiy, 2001],

$$S_b(t) = \zeta' \cdot S_0 \cdot \left(\frac{\pi}{3 \cdot |\delta\bar{\omega} \cdot t|} \right)^{1/2} e^{i \cdot \delta\bar{\omega} \cdot t/2 - R2_b \cdot t} \cdot \left[C \left(|3\delta\bar{\omega} \cdot t/2|^{1/2} \right) - i \cdot \text{sign}(t) \cdot S \left(|3\delta\bar{\omega} \cdot t/2|^{1/2} \right) \right]. \quad (3.49)$$

The functions $C(x)$ and $S(x)$ are the Fresnel cosine and sine integral functions, sign is a sign function which equals -1 for negative arguments and $+1$ for positive arguments. The transverse relaxation rate for blood depends on the blood oxygen saturation and is, at $3T$, given by [He und Yablonskiy, 2007],

$$R2_b = 5.0 + 173 \cdot (1 - Y)^2. \quad (3.50)$$

The total voxel signal is given as the sum of all the contributions,

$$S(t) = S_t(t) + S_e(t) + S_b(t). \quad (3.51)$$

The evaluation of the signal measured with the network phantoms, were performed using MATLAB *lsqcurvefit* with a non-linear Levenberg-Marquardt algorithm and self-written MATLAB code.

3.3.3.3 Error estimation

Signal noise is one of the limiting factors for parameter estimation. The signal noise originates mainly from random fluctuations in the receiving coil and inductive losses in the sample, and can be described by a Gaussian distribution. However, by taking the magnitude of the real and imaginary part of the signal, the noise is no longer Gaussian but rather described by a Rician distribution. For large SNR the Rician distribution approaches the Gaussian distribution and, hence, a Gaussian noise can be assumed in image regions with large SNR. In image regions where only noise is present, a special case of the Rician distribution, the Rayleigh distribution, is obtained. The mean, \bar{M} , and the variance, σ_M^2 , for this distribution is associated with the standard deviation of the Gaussian distribution, σ [Gudbjartsson und Patz, 1995],

$$\bar{M} = \sigma \sqrt{\frac{\pi}{2}}, \quad (3.52)$$

$$\sigma_M^2 = (2 - \pi/2)\sigma^2. \quad (3.53)$$

Hence, the uncertainty in a single measurement point can be obtained by measuring the mean signal, or the variance, in a signal free ROI in the image.

IV

Results

IN SECTION 3.3.3, methods were presented that allow quantitative estimations of the oxygen extraction in brain tissue. In the following sections, the evaluation of the methods is presented. Non-static dephasing conditions were simulated in phantom experiments. Diffusion effects were investigated and compared with the theory. Furthermore, the stability of the evaluation techniques was tested by means of simulations. Finally, the practical use was considered using *in vivo* measurements.

4.1 Phantom Measurements

4.1.1 Macroscopic inhomogeneities

Tissue oxygenation measurements using MRI are equivalent with the problem of estimating the volume susceptibility of the venous blood. The volume susceptibility of the venous blood can be determined by measuring the field distortion introduced by the paramagnetic vessels. This is performed by evaluation of the MR signal decay over time. However, any other source of inhomogeneities affects the signal as well, and their susceptibility effects add to the desired effect and, thus, spoil the estimation. The modeling of macroscopic field inhomogeneities was described in section 3.3.1.

The correction method was tested in phantom measurements. A syringe containing water doped with contrast agent was attached to the bottom of a bottle phantom, inducing macroscopic field inhomogeneities. The dimensions of the 3D GRE voxels was chosen smaller than the dimensions of the GESSE voxels, i.e. $1 \times 1 \times 2 \text{ mm}^3$. A TR of 100 ms , and a flip angle of 20° was used.

An original GESSE magnitude image can be seen in Figure 4.1 (a), together with the inhomogeneity corrected image (b) and the calculated correction function (c). The signal obliteration in the center of the phantom caused by the contrast agent is fully corrected for in the corrected magnitude image (b). In Figure 4.2, the natural logarithm of the signal-time development for the pixel marked with a blue ROI in Figure 4.1 can be seen, before

and after correction. Since the phantom contains pure water doped with $NiSO_4$ and $NaCl$, a mono-exponential decay is expected. Before correction, the signal decays much faster than would be expected by pure T2 decay, and not in a mono-exponential manner. After the correction, however, a more mono-exponential decay is present, indicating that the macroscopic inhomogeneity correction was successful. For all GESSE measurements presented in this work, an accompanying 3D GRE scan was acquired and used to calculate a correction function with the approach presented in section 3.3.1. The macroscopic inhomogeneity correction was applied before further evaluation.

4.1.2 Single Cylinder

The network phantoms mentioned in section 3.2 were constructed using polyamide strings and a $NiSO_4$ solution. In order to verify the results obtained with the network phantoms, independent measurements of the magnetic susceptibility difference between the polyamide string and $NiSO_4$ solutions of different concentrations were carried out. The measurements were performed using the single polyamide string phantoms presented in section 3.2.3.1, according to the method presented in Sedlacik et al. [2007] (c.f. section 3.1.1).

Single string measurements were performed for a $NiSO_4 \cdot 6H_2O$ concentration of 1, 3, 5 and 7 g/l. In Figure 4.3, the measured signal curves, normalized to a surrounding homogeneous ROI, for each $NiSO_4$ concentration can be seen together with the fitted signal curves. The large uncertainty of the last measurement points for the 5 g/l and 7 g/l measurements arises due to extremely low SNR. Those points, however, become a very low weighting factor during curve fitting due to their large relative error. The signal decay is almost identical for the two different string diameters, which is expected since the relative volume fraction is nearly the same. The obtained calibration curves for the susceptibility difference between strings and solution as a function of $NiSO_4 \cdot 6H_2O$ concentration are shown in Figure 4.4 (a). A strong linear relationship exists for both string diameters. However, the absolute susceptibility difference differs for the two string types for a given $NiSO_4 \cdot 6H_2O$ concentration. The calibration curve for R2, measured with the CPMG sequence at 3 T, as a function of $NiSO_4 \cdot 6H_2O$ concentration can be seen in Figure 4.4 (b).

The aim of the single string measurements was to characterize the network phantoms. In Table 4.1, the specifications for the four network phantoms as obtained from the single string measurements are shown. The R2 for each network phantom was measured at 3 T and 1.5 T using the CPMG sequence. The R2 value obtained at 3 T was converted to a $NiSO_4 \cdot 6H_2O$ concentration using the R2 calibration curve (Figure 4.4). This step was performed because uncertainties in the $NiSO_4$ concentration are introduced during the phantom filling and degassing process. The obtained $NiSO_4 \cdot 6H_2O$ concentration, however, was comparable to the projected ones. The susceptibility difference between the polyamide strings and the surrounding solution could be subsequently established for each phantom using the calculated $NiSO_4 \cdot 6H_2O$ concentrations and the $\Delta\chi$ calibration curve. The $\Delta\chi$ values obtained with the single string method differ somewhat for the two string diameters used. In Table 4.1 the reference $\Delta\chi$ for each phantom is specified as the range between the two calibration curves.

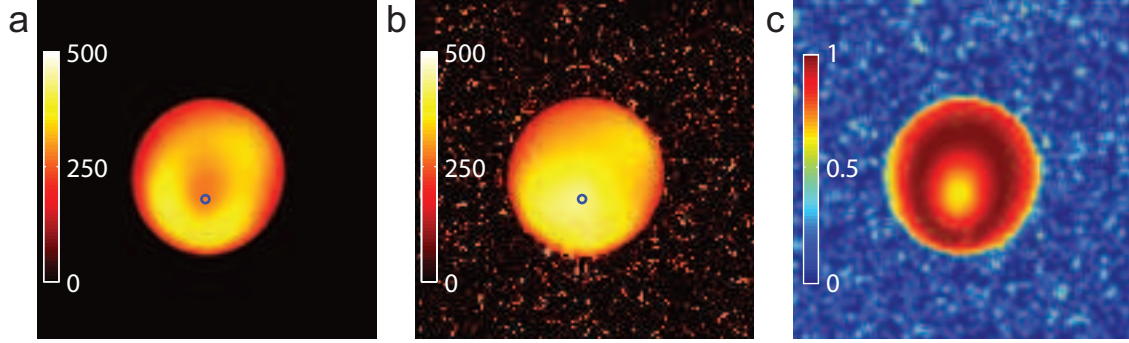


Figure 4.1. Macroscopic inhomogeneity correction. A syringe containing contrast agent doped water induces macroscopic field inhomogeneities. **a)** The macroscopic field inhomogeneities cause signal cancellation in the center of the phantom in the uncorrected GESSE image. **b)** After the macroscopic inhomogeneity correction is applied, the signal obliteration has vanished. **c)** The calculated correction function is the product of the correction of the macroscopic field inhomogeneities in all three spatial direction, here shown exemplarily.

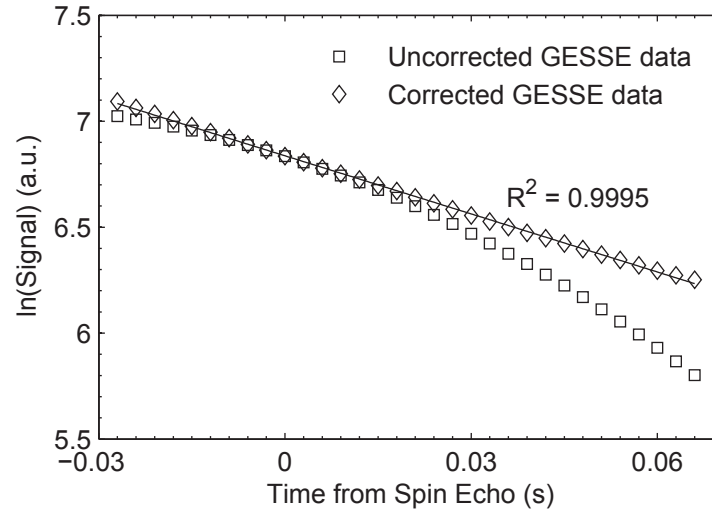


Figure 4.2. Uncorrected and macroscopic inhomogeneity corrected signal. Natural logarithm of the signal intensity over time in a ROI positioned in an inhomogeneous region of the phantom. In absence of macroscopic field inhomogeneities, a mono-exponential behavior is expected due to the T2 decay. Before the correction (squares), the signal-time course clearly deviates from the expected mono-exponential behavior. The solid line represents a linear regression to all measured points after macroscopic inhomogeneity correction. After correction, the signal shows a mono-exponential decay

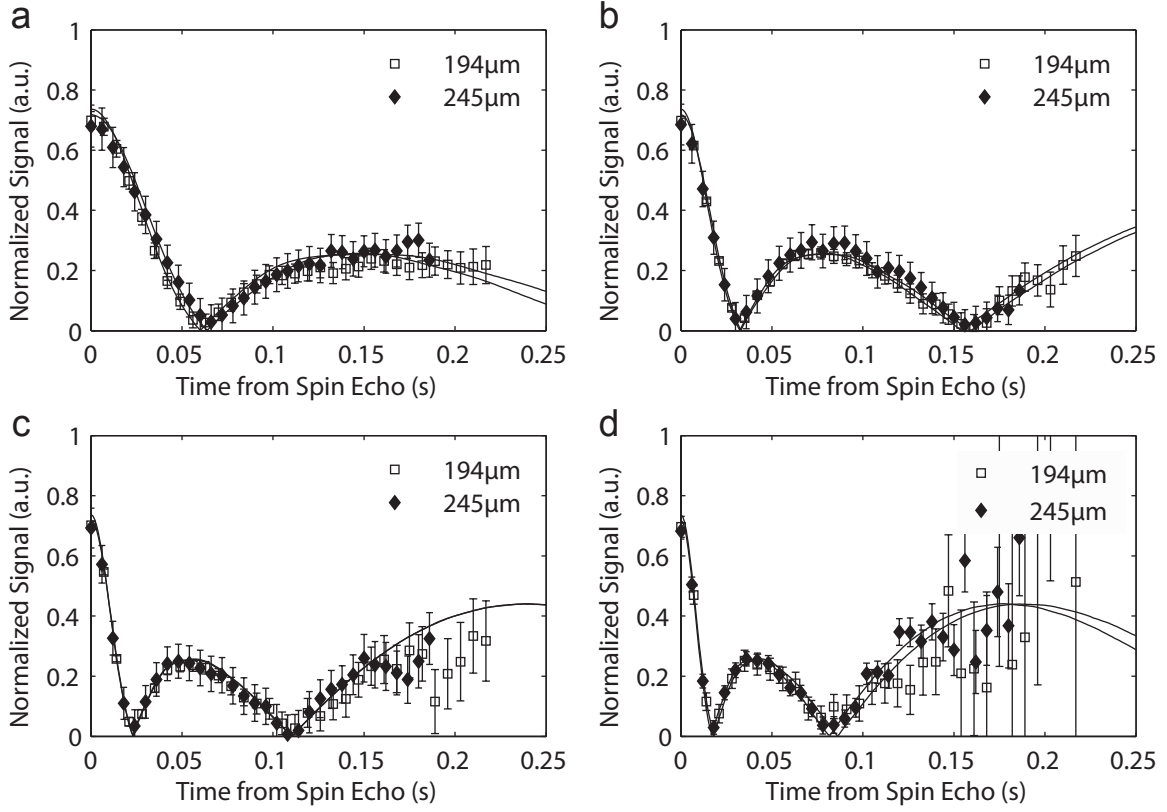


Figure 4.3. Measured signal from voxels containing a single polyamide string surrounded by **a)** $1\text{ g/l NiSO}_4 \cdot 6\text{H}_2\text{O} + 5\text{ g/l NaCl}$, **b)** $3\text{ g/l NiSO}_4 \cdot 6\text{H}_2\text{O} + 5\text{ g/l NaCl}$, **c)** $5\text{ g/l NiSO}_4 \cdot 6\text{H}_2\text{O} + 5\text{ g/l NaCl}$ and **d)** $7\text{ g/l NiSO}_4 \cdot 6\text{H}_2\text{O} + 5\text{ g/l NaCl}$. The signal is normalized to a homogeneous ROI to eliminate the T2 signal decay. The uncertainties in each measurement point are obtained from the standard deviation of the signal in a homogeneous ROI in the phantom. The susceptibility difference between a single string and the surrounding solution is obtained by fitting the simulated signal decay to the measured signal. The fitted signal is marked as black solid lines, and agrees well with the measured signal for all measurements.

Table 4.1. Network phantoms specifications as obtained from the single string measurements

String diameter (μm)	$R2^a$ at 1.5 T (s^{-1})	$R2^a$ at 3 T (s^{-1})	Concentration NiSO_4^b (g/l)	$\Delta\chi^c$ (ppm)
27	10.84	13.56	4.11	1.19 – 1.28
63	10.20	12.43	3.76	1.11 – 1.20
89	8.18	10.06	3.01	0.95 – 1.03
245	8.54	10.28	3.08	0.96 – 1.04

^a Measured with the CPMG sequence.

^b $\text{NiSO}_4 \cdot 6\text{H}_2\text{O}$ concentration calculated using the R2 calibration curve.

^c The range of $\Delta\chi$ values corresponds to the distance between the two calibration curves measured using a $194\text{ }\mu\text{m}$ string and a $245\text{ }\mu\text{m}$ string respectively.

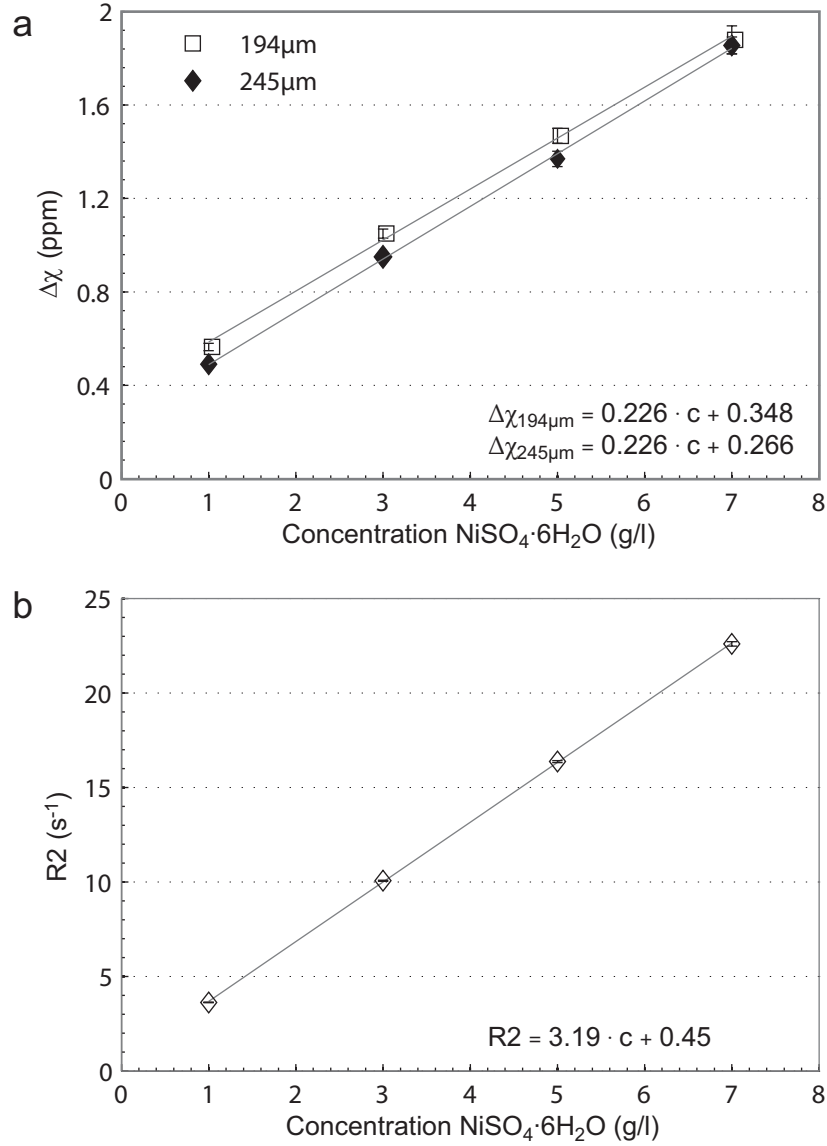


Figure 4.4. **a)** Calibration curve of susceptibility difference ($\Delta\chi$) as a function of NiSO_4 concentration, obtained with single string measurements using a string diameter of 194 μm and 245 μm . A linear relationship between $\Delta\chi$ and the $\text{NiSO}_4 \cdot 6\text{H}_2\text{O}$ concentration was found for both string diameters. The $\Delta\chi$ obtained for the thinner string was approximately 0.1 ppm larger than the $\Delta\chi$ obtained for the thicker string for all NiSO_4 concentrations. **b)** Calibration curve of R_2 as a function of NiSO_4 concentration. The R_2 values were measured at 3T using a CPMG sequence with 12 echoes. Error bars are smaller than symbols when not visible.

4.1.3 Network Phantom

The single string measurements aimed to produce calibration curves that can be used to characterize the cylinder network phantoms. When the susceptibility difference between the polyamide strings and the $NiSO_4$ solution in the network phantoms is known, they can be used to examine the theoretical models. All phantom measurements were performed using the custom-built network phantoms as presented in section 3.2.

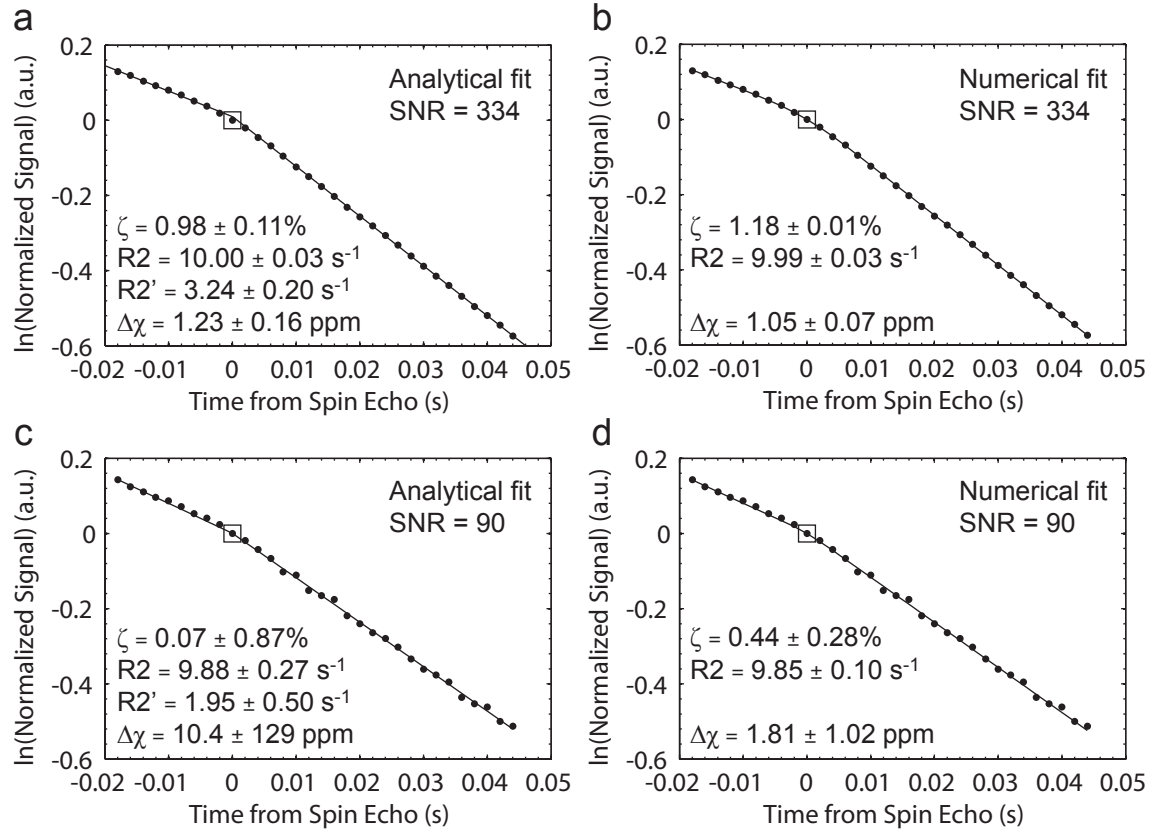


Figure 4.5. Evaluation of signal from one voxel in the string filled compartment in the cylinder network phantom with a string diameter of $245 \mu m$. The spin echo is emphasized with a black unfilled square. **a)** SNR of 334 and analytical evaluation method. A susceptibility difference ($\Delta\chi$) comparable to the expected value of 1 ppm is obtained. The parameter estimation is stable. **b)** SNR of 334 and numerical evaluation method. A $\Delta\chi$ very close to the expected value of 1 ppm is obtained. The parameter estimation is more stable than when the analytical evaluation method is used at the same SNR. **c)** SNR of 90 together with the analytical evaluation method. A relative volume fraction (ζ) very close to zero and with large uncertainty is obtained. This is reflected in the calculated $\Delta\chi$ which is much larger than the expected value and has a relative parameter error of 1240%. **d)** SNR of 90 and numerical evaluation method. The obtained $\Delta\chi$ deviates from the expected value. Although the relative parameter error of 56% is high it is substantially smaller than for the analytical method at the same SNR.

4.1.3.1 Evaluation Technique

In section 3.3.3, two evaluation techniques for data sampled with a GESSE sequence were mentioned. The analytical method takes advantage of the asymptotic forms that exist for the characteristic function for long and short echo times. In contrast, with the numerical method, the signal is calculated numerically and fitted to the measured points in an iterative manner.

In Figure 4.5, the voxel signal measured with a GESSE sequence and the $245\ \mu\text{m}$ cylinder network phantom is shown for a SNR of 334 (upper row) and a SNR of 90 (lower row). The fitted curves obtained with the analytical method are shown in (a) and (c), together with the fitting results. The combined analytical method yields reasonable results in case of higher SNR, where the achieved susceptibility difference is on the same order as the expected value of about $1\ \text{ppm}$. However, when the SNR is low the evaluation shows extremely unstable results. The volume fraction is now very close to zero and has a huge uncertainty that is reflected by the enlarged susceptibility difference achieved and its enormous relative parameter error of approximately 140 %. The fits to the same signal data, when using the numerical method are shown in Figure 4.5 (b) and (d), for the higher and lower SNR, respectively. At high SNR, the numerical method yields more accurate results than the analytical method. However, the largest difference is seen in case of low SNR. Even though the estimated $\Delta\chi$ deviates from the true value, the stability compared to the analytical method is substantially improved. This speaks in favor for the numerical method. Besides, it is not straightforward to derive asymptotic forms for more complex models including diffusion, intravascular signal or a multi-compartment system. Since the aim of this thesis is to investigate the possibility to quantify the BOLD effect under non-static dephasing conditions, a model including diffusion effects has to be accessible. Consequently, the numerical method is the better choice for further investigation.

4.1.3.2 Network phantom measurement

The effect of diffusion is assumed large for small cylinder diameters, long echo times and low field strengths. GESSE scans were made with all four string network phantoms at both $3\ T$ and $1.5\ T$. The high-resolution 3D GRE images, also used for inhomogeneity correction, were used to define ROIs inside the string-containing compartment of the phantoms. The average signal in each ROI was used for evaluation. All measured signal curves along with the evaluated parameter when three ($\Delta\chi$, ζ and R_2), two ($\Delta\chi$ and ζ or $\Delta\chi$ and R_2) and one ($\Delta\chi$) fit parameter is used can be found in Appendix A.

Figure 4.6 (a-b) shows typical magnitude and phase images, acquired with the high-resolution 3D GRE sequence. The evaluation ROI is marked with a yellow circle. Figure 4.6 (c) shows the signal curves measured using the $89\ \mu\text{m}$ network phantom at $3\ T$ for the shorter and the longer spin echo time (TE_{SE}). The shape of the signal curves measured at different echo times can be compared if the signal curves are normalized to the spin echo signal and plotted against the time from spin echo. The resulting plot is shown in Figure 4.6 (d). According to the static dephasing theory, the signal decay around a spin echo should be independent of the echo time. As seen in Figure 4.6 (d) there is a clear

difference in signal decay between two measured signal curves, both before and after the spin echo. The difference, however, is more pronounced before the spin echo. This effect was seen for all network phantoms and was more pronounced for smaller string diameters. The diffusion model predicts similar unsymmetrical signal decay dependent on the echo time. Hence, the effect seen in the phantom measurements is likely to be a diffusion effect.

All phantom measurements were evaluated using both the static dephasing model and the water diffusion model. The $\Delta\chi$ and ζ values obtained from the evaluation using three fit parameters ($\Delta\chi$, ζ and R2) are shown in the upper half of Table 4.2. The ADC measured with the diffusion weighted EPI was used as input to the water diffusion model, together with the string radius as specified from the manufacturer. Hence, both models have the same number of free parameters.

Examination of the results obtained with the static dephasing model reveals that only large string diameters in combination with a short echo time results in $\Delta\chi$ values comparable to the $\Delta\chi$ known from the single string measurements. For smaller string diameters and longer echo time, the deviation from the expected parameter values is substantial. In general, the obtained $\Delta\chi$ values are lower than anticipated. The results are somewhat closer to the expected values for the measurements performed at lower field strength. The errors displayed in the table are the standard deviation obtained using MATLAB function *nlparci*.

The $\Delta\chi$ values obtained for small string diameters using the static dephasing model are obviously incorrect. If this is due to the effect of diffusion, accurate results should be obtained when the evaluation is performed using the water diffusion model. The parameters estimated using the water diffusion model can be seen in the lower half of Table 4.2 for both 3 T and 1.5 T. Surprisingly, the evaluation using the water diffusion model does not yield any reasonable results except for the measurements performed with the 245 μm phantom. In general, $\Delta\chi$ is underestimated for the measurement with a shorter spin echo time and overestimated for the measurement with a longer spin echo time.

To conclude, for all network phantoms with strings thinner than 245 μm , the evaluation of the measured data using the static dephasing model yields incorrect values of $\Delta\chi$. However, if the water diffusion model is used, the evaluation still fails. Either the water diffusion model is incapable of describing the measurement system or there is some great instability in the evaluation method.

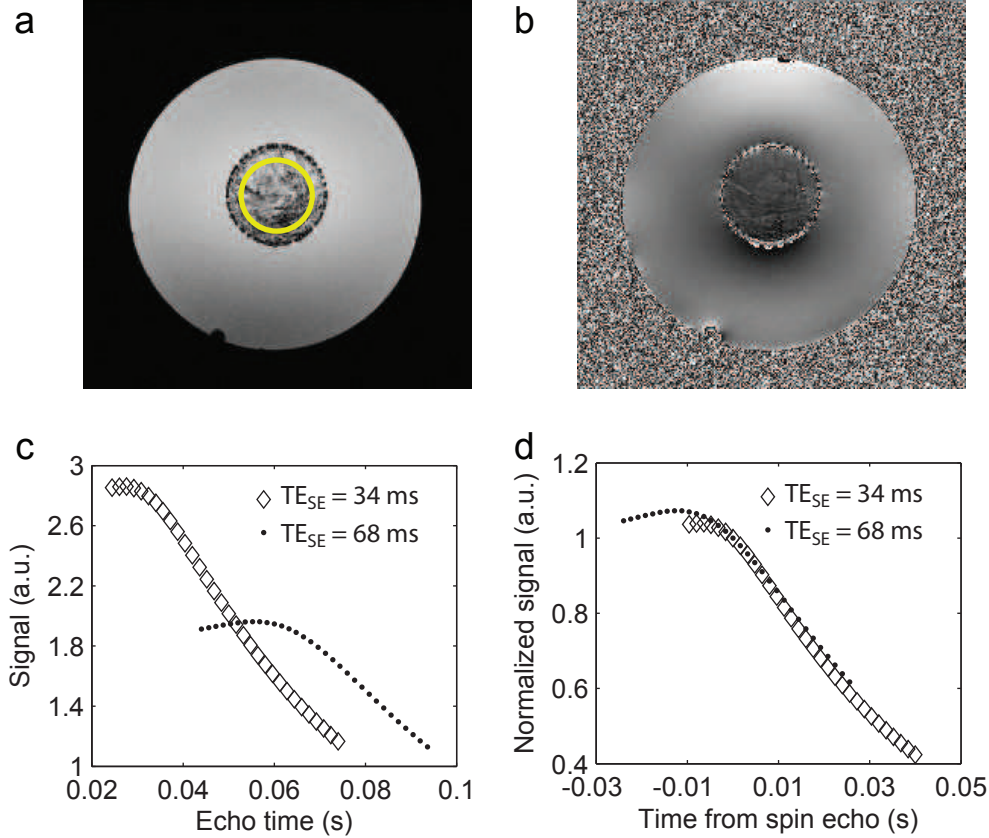


Figure 4.6. Measurement using the $89\mu\text{m}$ phantom. **a)** 3D GRE magnitude image with evaluation ROI marked as a yellow circle. The inhomogeneous packing of the polyamide strings is visualized by the varying signal intensity in the ROI. Darker areas represent regions with higher volume fraction of polyamide strings. **b)** The to (a) corresponding 3D GRE phase image. **c)** Signal as function of echo time, measured with the GESSE sequence using one shorter spin echo time (TE_{SE}) of 34 ms and one longer TE_{SE} of 68 ms . **d)** The measured signal shown in (c), but now normalized at the spin echo signal intensity and plotted against the time from the spin echo. A clear deviation between the two signal curves can be seen, which is not in agreement with the static dephasing model. Since the water diffusion model predicts such an unsymmetrical signal behavior, the effect is likely to be a diffusion effect. Absence of error bars indicates that the standard error interval was smaller than the size of the data symbol.

Table 4.2. $\Delta\chi$ and ζ values obtained when evaluating the network phantom measurements using the static dephasing (SD) model and the water diffusion (WD) model.

B_0 (T)	Model ^a	Echo Time	String diameter							
			245 μm		89 μm		63 μm		27 μm	
			$\Delta\chi$ (ppm)	ζ (%)	$\Delta\chi$ (ppm)	ζ (%)	$\Delta\chi$ (ppm)	ζ (%)	$\Delta\chi$ (ppm)	ζ (%)
3.0	SD	34 ms	1.014 \pm 0.021	3.20 \pm 0.08	0.855 \pm 0.021	5.30 \pm 0.15	0.619 \pm 0.027	6.68 \pm 0.35	0.544 \pm 0.024	3.63 \pm 0.19
		68 ms	0.766 \pm 0.023	4.10 \pm 0.15	0.473 \pm 0.050	9.91 \pm 1.59	0.353 \pm 0.064	11.72 \pm 3.63	0.219 \pm 0.109	12.15 \pm 11.56
1.5	SD	34 ms	0.930 \pm 0.012	4.83 \pm 0.07	0.962 \pm 0.015	5.00 \pm 0.10	1.103 \pm 0.025	3.89 \pm 0.10	0.899 \pm 0.044	2.66 \pm 0.16
		68 ms	0.925 \pm 0.038	4.14 \pm 0.26	0.724 \pm 0.121	7.07 \pm 1.99	0.669 \pm 0.150	6.90 \pm 2.68	0.492 \pm 0.136	7.06 \pm 3.64
3.0	WD	34 ms	1.089 \pm 0.040	3.02 \pm 0.13	0.771 \pm 0.051	7.21 \pm 0.56	0.377 \pm 0.005	15.66 \pm 0.23	3.000 \pm 2.152	0.90 \pm 0.79
		68 ms	1.097 \pm 0.032	2.95 \pm 0.09	2.076 \pm 0.198	2.16 \pm 0.23	2.760 \pm 0.343	1.24 \pm 0.17	2.996 \pm 0.574	0.59 \pm 0.13
1.5	WD	34 ms	0.900 \pm 0.006	5.23 \pm 0.04	0.708 \pm 0.005	8.60 \pm 0.08	0.665 \pm 0.008	9.09 \pm 0.12	3.000 \pm 2.195	1.25 \pm 1.14
		68 ms	0.903 \pm 0.038	4.50 \pm 0.28	2.923 \pm 0.481	1.49 \pm 0.27	3.000 \pm 0.372	1.32 \pm 0.18	3.000 \pm 1.069	0.92 \pm 0.36
Reference values ^b			0.96 – 1.04	3	0.95 – 1.03	5	1.11 – 1.20	3	1.19 – 1.28	2

^a Theoretical model used for the evaluation. SD - Static dephasing model, WD - Water diffusion model.

^b Reference values for $\Delta\chi$ as obtained in the single string measurement.

Resemblance between measured and theoretical signal curves

To investigate the evaluation method further, the root mean squared error (RMSE) between a measured signal curve and a set of theoretical curves was calculated. Theoretical signal curves were computed, with the static dephasing model and the water diffusion model, by changing ζ from 0 to 10 % in steps of 0.05 % and $\Delta\chi$ from 0.5 to 2 ppm in steps of 0.0075 ppm. The similarity between every theoretical signal curve and the measured signal curve was examined by calculation of the RMSE. A low RMSE value indicates that the calculated signal curve is very similar to the measured signal curve. The result can be seen in Figure 4.7 for the signal curve measured with the 245 μm phantom at 3 T, using an echo time of 37 ms. Figure 4.7 (a) shows the natural logarithm of the RMSE between the measured signal curve and theoretical signal curves calculated with the water diffusion model and a number of combinations of ζ and $\Delta\chi$. The expected parameter set ($\zeta = 3\%$ and $\Delta\chi = 1\text{ ppm}$) is marked with a white cross. The corresponding RMSE plot when the water diffusion model is used to calculate the signal curves can be seen in Figure 4.7 (b). Figure 4.7 (c) shows the RMSE profiles at the relative volume fraction marked with a black, dashed line in (a) and (b). Using a large string diameter and short echo time, no large diffusion effect is expected. Not surprisingly, the RMSE plots for the static dephasing model and the water diffusion model are almost identical. Furthermore, the minimum RMSE at a relative volume fraction of 3 % is located at a $\Delta\chi$ of 0.99 ppm and 1.00 ppm for the static dephasing method and the water diffusion method, in that order. Those values are close to the expected value of approximately 1 ppm, indicating that both models manage to describe this system well.

Figure 4.8 shows the RMSE plots for a measurement performed at 1.5 T using the 27 μm phantom and an spin echo time of 68 ms. Under those conditions, the effect of diffusion should be extensive. Figure 4.8 (a-b) shows the corresponding RMSE plots for the static dephasing model and the water diffusion model, respectively. The expected volume fraction of 2 % is marked with a dashed line. Now, a large discrepancy between the two RMSE plots is present. The plot for the water diffusion model is similar to the ones obtained for the 245 μm phantom whereas for the static dephasing model, the valley of low RMSE is shifted to smaller values of ζ . When studying those RMSE plots, it is straightforward to conclude that if the static dephasing model is used for evaluation, accurate results will never be achieved. In Figure 4.8 (c) the corresponding RMSE profiles are shown. At the expected volume fraction of 2 %, the static dephasing model has a RMSE minimum at a $\Delta\chi$ of 0.53 ppm while the water diffusion model has its minimum at a $\Delta\chi$ of 1.22 ppm. The latter is in good agreement with the expected value. Hence, the water diffusion model appears to be able to predict the measured signal curve. However, studying the RMSE plots, a dark band, representing low RMSE values appears across the plots, providing an explanation for the evaluation failure. All signal curves located in this valley are very similar to the measured signal curve. Furthermore, the RMSE intensity along this track is not continuous but darker spots can be seen along the line, indicating local RMSE minimum. The position of those minima is presumably dependent on the image noise and, hence, the value obtained at evaluation can turn up as whichever value located in or in the vicinity of the valley.

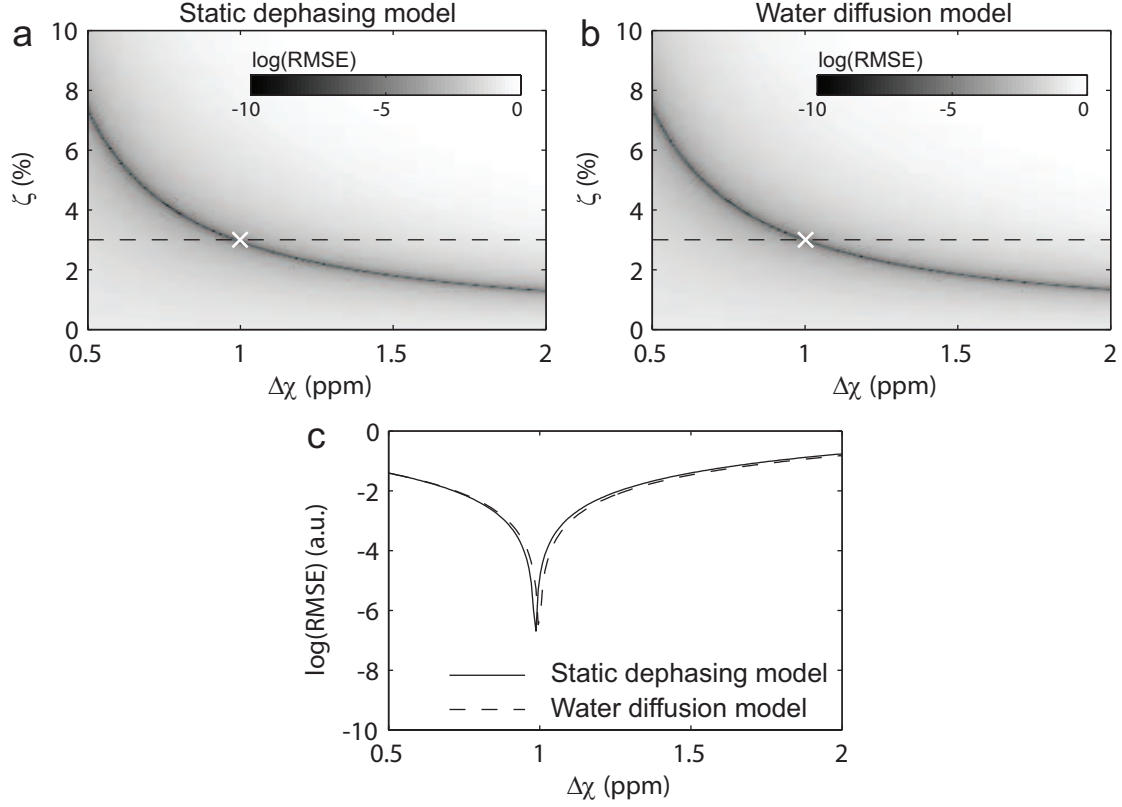


Figure 4.7. RMSE plots for the $245\,\mu\text{m}$ phantom using a short echo time. **a)** Natural logarithm of the root mean squared error (RMSE) between the measured signal curve and theoretical signal curves calculated using the static dephasing model. The expected set of ζ (3%) and $\Delta\chi$ (1 ppm) is marked with a white cross. A low RMSE value at a certain combination of ζ and $\Delta\chi$ indicates that the signal curve calculated using those parameter values is similar to the measured signal curve. A curved band of low RMSE values can be seen across the plot indicating a set of curves almost identical to the measured signal curve. Along this band, local minima with lower RMSE than at the expected set of ζ and $\Delta\chi$ can be seen. At evaluation, the curve fitting routine searches for the point with the lowest RMSE. Hence, this band of low RMSE values with local minima explains the incorrect outcome of the evaluation of the phantom measurements. **b)** Natural logarithm of the root mean squared error (RMSE) between the measured signal curve and theoretical signal curves calculated using the water diffusion model. The expected set of ζ (3%) and $\Delta\chi$ (1 ppm) is marked with a white cross. Using the water diffusion model results in essentially the same RMSE plot as for the static dephasing model (a) indicating that the effect of diffusion the signal formation is minimal as expected for a large string diameter and short echo time. The same band of low RMSE values is seen across the plot demonstrating that it is difficult to achieve simultaneous estimation of ζ and $\Delta\chi$. **c)** Profiles of the natural logarithm of the root mean squared error RMSE at the volume fraction of 3% marked with a black, dashed line in (a) and (b), for the static dephasing model (solid line) and the water diffusion model (dashed line). For a fixed ζ of 3%, there is a clear RMSE minimum at a $\Delta\chi$ corresponding to the expected value of 1 ppm. This indicates that both models manage to describe the system well

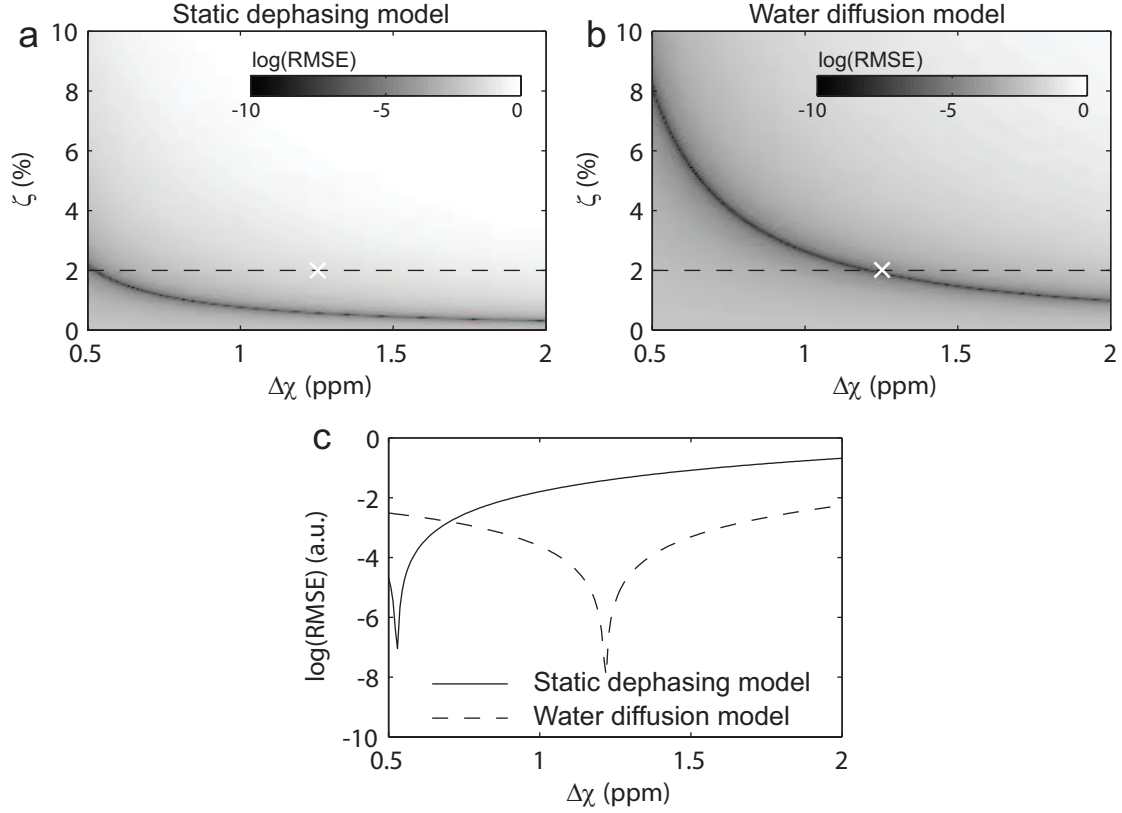


Figure 4.8. RMSE plots for the $27 \mu\text{m}$ phantom using a long echo time. **a)** Natural logarithm of the root mean squared error (RMSE) between the measured signal curve and theoretical signal curves calculated using the static dephasing model. The expected set of ζ (2 %) and $\Delta\chi$ (1.25 ppm) is marked with a white cross. A low RMSE value at a certain combination of ζ and $\Delta\chi$ indicates that the signal curve calculated using those parameter values is similar to the measured signal curve. A curved band of low RMSE values can be seen across the plot indicating a set of curves almost identical to the measured signal curve. However, none of the low RMSE values correspond to a signal curve calculated using the expected parameter set. This shows that the static dephasing model does not manage to describe the measured curve. Hence, a correct outcome of the evaluation will never be achieved when the static dephasing model is used. This is expected since a substantial diffusion effect is predicted for small string diameters and large spin echo times. **b)** Natural logarithm of the root mean squared error (RMSE) between the measured signal curve and theoretical signal curves calculated using the water diffusion model. The expected set of ζ (2 %) and $\Delta\chi$ (1.25 ppm) is marked with a white cross. A large discrepancy between the two RMSE plot calculated using the static dephasing model and the water diffusion model is present. The water diffusion model has a low RMSE for the expected parameter set, indicating that this model manage to describe the measured signal curve well. However, the band of low RMSE values with local minima precludes a simultaneous estimation of ζ and $\Delta\chi$. **c)** Profiles of the natural logarithm of the root mean squared error RMSE at the volume fraction of 2 %, marked with a black, dashed line in (a) and (b), for the static dephasing model (solid line) and the water diffusion model (dashed line). For a fixed ζ of 2 %, clear RMSE minima can be found for both models. The $\Delta\chi$ value corresponding to those RMSE minima, however, differs for the two models. In contrast to the static dephasing model, the water diffusion model has a RMSE minimum at a $\Delta\chi$ value very close to the expected value of 1.25 ppm, indicating that this model manage to describe the system well.

Reduced number of fit parameters

The band of low RMSE values indicating similar signal curves is relatively narrow. Hence, if $\Delta\chi$ or ζ is previously known, it should be possible to accurately estimate the other of the two parameters. In Table 4.3, the results when evaluating the network phantom measurements using the expected value of ζ as fix parameter are presented. Now the obtained $\Delta\chi$ values are much closer to the reference values. When using the static dephasing model, the obtained $\Delta\chi$ values are in general lower than the reference value. On the contrary, when using the water diffusion model the obtained $\Delta\chi$ values are rather a bit higher than the expected values. The deviation from the expected $\Delta\chi$ is larger for smaller string diameters. The $\Delta\chi$ values obtained for the $245\ \mu\text{m}$ phantom are not as close to the expected values as when both ζ and $\Delta\chi$ were used as fit parameters (Table 4.2). The simultaneous fit of ζ and $\Delta\chi$ for the short echo time both resulted in volume fractions larger than 3%. Hence, the incorrect result when using a fix ζ could be a consequence of that the imaging slice during the measurement at the $1.5\ T$ system was positioned so that the volume fraction of strings inside the ROI was somewhat higher than the anticipated 3%. When using a fix volume fraction of 4% a $\Delta\chi$ of $1.11\ \text{ppm}$ is obtained for both the static dephasing model the water diffusion model for the shorter echo time. For the longer echo time the corresponding $\Delta\chi$ values are $0.94\ \text{ppm}$ for the static dephasing model and $0.98\ \text{ppm}$ for the water diffusion model. Those values agree well with the expected $1\ \text{ppm}$. However, this further illustrates the instability of the evaluation method and how important it is to have previous knowledge of the exact value of ζ .

Table 4.3. $\Delta\chi$ values obtained when evaluating the network phantom measurements using a fixed value of ζ , for both the static dephasing (SD) model and the water diffusion (WD) model.

B ₀ (T)	Model ^a	Echo Time	String diameter			
			245 μm	89 μm	63 μm	27 μm
			Δχ (ppm)	Δχ (ppm)	Δχ (ppm)	Δχ (ppm)
3.0	SD	34 ms	1.068 ± 0.005	0.894 ± 0.005	1.191 ± 0.036	0.881 ± 0.023
		68 ms	0.996 ± 0.008	0.770 ± 0.014	0.911 ± 0.026	0.648 ± 0.019
1.5	SD	34 ms	1.359 ± 0.034	0.960 ± 0.006	1.361 ± 0.019	1.128 ± 0.024
		68 ms	1.148 ± 0.007	0.893 ± 0.009	1.126 ± 0.020	1.036 ± 0.018
3.0	WD	34 ms	1.093 ± 0.006	1.044 ± 0.010	1.552 ± 0.034	1.567 ± 0.050
		68 ms	1.076 ± 0.003	0.972 ± 0.011	1.240 ± 0.019	0.989 ± 0.030
1.5	WD	34 ms	1.404 ± 0.034	1.122 ± 0.021	1.774 ± 0.043	2.053 ± 0.086
		68 ms	1.211 ± 0.007	1.007 ± 0.015	1.440 ± 0.024	1.474 ± 0.062
Reference values ^b			0.96 – 1.04	0.95 – 1.03	1.11 – 1.20	1.19 – 1.28

^a Theoretical model used for the evaluation. SD - Static dephasing model, WD - Water diffusion model.

^b Reference values for $\Delta\chi$ as obtained in the single string measurement.

4.2 Simulations

TO INVESTIGATE THE stability of the evaluation method, simulations were performed. Non-static dephasing data, i.e., data calculated with the water diffusion model, were evaluated using the static dephasing model. The result was explored to establish if the pattern observed in the phantom measurements could be associated with diffusion. Furthermore, as seen in the previous chapters several set of ζ and $\Delta\chi$ yields very similar signal curves. This causes problems since the evaluation process is based on non-linear, least square curve fitting. The parameters that affect the appearance of the static dephasing signal curve, apart from $\Delta\chi$ and ζ , are the relaxation rate R2, the sequence parameters chosen for the GESSE scan and the SNR. Next, the influence of those parameters is investigated.

4.2.1 Static Evaluation of Non-static dephasing Data

Theoretical signal curves were calculated using the water diffusion model and the parameters expected in the phantoms (c.f. Table 3.2 and Table 4.1). An ADC of $2.1 \cdot 10^{-9} m^2/s$ was used for all calculations. The diffusion influenced signal curves were subsequently evaluated using the static dephasing model. The results from the evaluation using both $\Delta\chi$ and ζ as fit parameters can be seen Table 4.4. Table 4.5 shows the obtained $\Delta\chi$ when ζ is used as a fix parameter.

The values obtained for the long spin echo time sequence are very consistent with the corresponding values obtained at evaluation of the network phantom measurements. For the short spin echo time sequence, however, $\Delta\chi$ is overestimated when evaluating the simulated data in contrast to the evaluation of the measured data where $\Delta\chi$ in general was underestimated. Using a fixed value of ζ results in $\Delta\chi$ values lower than the true value. The deviation is larger for smaller string diameters. Those results are fairly consistent with the outcome of the phantom measurements. However, there is a difference between the results obtained with the sequence using a longer spin echo time and the results obtained with the sequence using a shorter spin echo time. In the next section, the dependence of the stability of the parameter evaluation on SNR and sequence parameters used is examined.

The simulated non-static dephasing data together with the parameters obtained from the evaluation using the static dephasing model can be found in Appendix B.

4.2.2 Dependence on SNR and Sequence Parameters

Figure 4.9 shows surface plots of the RMSE between a signal curve calculated using $\Delta\chi = 0.58 ppm$ and $\zeta = 3\%$ at $3T$ and all other curves with $\Delta\chi = 0 - 1.2 ppm$ and $\zeta = 0 - 10\%$. A $\Delta\chi$ of $0.58 ppm$ corresponds to a oxygenation saturation of about 50% *in vivo*, which approximately is the level that is expected in the brain. Furthermore, a volume fraction of about 3% is the value found in gray matter. The RMSE plot is shown for an ideal case, where no signal noise is present. In a linear scale, it is not possible to detect a clear minimum. However, observing the logarithmic values, a narrow peak corresponding to the

true parameter set is clearly visible. As seen in the phantom measurements, this peak will be masked in case of signal noise, and the minimum RMSE will be found somewhere else in the valley. The statistical errors in the parameter estimation will be dependent on the signal noise and possibly on the sequence parameters used.

Table 4.4. $\Delta\chi$ and ζ values obtained when evaluating calculated non-static dephasing data using the static dephasing (SD) model.

B_0 (T)	Echo Time	String diameter			
		$245\ \mu m$		$89\ \mu m$	
		$\Delta\chi$ (ppm)	ζ (%)	$\Delta\chi$ (ppm)	ζ (%)
3.0	34 ms	0.961 ± 0.015	3.06 ± 0.06	0.935 ± 0.055	4.51 ± 0.31
	68 ms	0.742 ± 0.029	3.92 ± 0.19	0.440 ± 0.091	11.38 ± 3.72
1.5	34 ms	1.018 ± 0.009	2.84 ± 0.03	1.226 ± 0.041	3.27 ± 0.13
	68 ms	0.976 ± 0.061	2.96 ± 0.28	0.734 ± 0.260	6.73 ± 4.02
Reference values		1.000	3.00	1.000	5.00

B_0 (T)	Echo Time	String diameter			
		$63\ \mu m$		$27\ \mu m$	
		$\Delta\chi$ (ppm)	ζ (%)	$\Delta\chi$ (ppm)	ζ (%)
3.0	34 ms	1.000 ± 0.085	2.65 ± 0.26	1.121 ± 0.181	1.17 ± 0.22
	68 ms	0.336 ± 0.128	11.60 ± 7.65	0.214 ± 0.251	15.83 ± 35.71
1.5	34 ms	1.525 ± 0.090	1.60 ± 0.11	2.069 ± 0.338	0.55 ± 0.10
	68 ms	0.663 ± 0.287	5.31 ± 4.00	0.570 ± 0.603	4.23 ± 8.07
Reference values		1.150	3.00	1.250	2.00

Table 4.5. $\Delta\chi$ values obtained when evaluating theoretical non-static dephasing data using the static dephasing (SD) model and a fix value of ζ .

B_0 (T)	Echo Time	String diameter			
		$245\ \mu m$	$89\ \mu m$	$63\ \mu m$	$27\ \mu m$
		$\Delta\chi$ (ppm)	$\Delta\chi$ (ppm)	$\Delta\chi$ (ppm)	$\Delta\chi$ (ppm)
3.0	34 ms	0.974 ± 0.003	0.856 ± 0.011	0.899 ± 0.016	0.716 ± 0.024
	68 ms	0.924 ± 0.008	0.784 ± 0.022	0.839 ± 0.033	0.756 ± 0.047
1.5	34 ms	0.971 ± 0.004	0.864 ± 0.018	0.903 ± 0.027	0.688 ± 0.039
	68 ms	0.964 ± 0.006	0.880 ± 0.019	0.937 ± 0.027	0.880 ± 0.041
Reference values		1.000	1.000	1.150	1.250

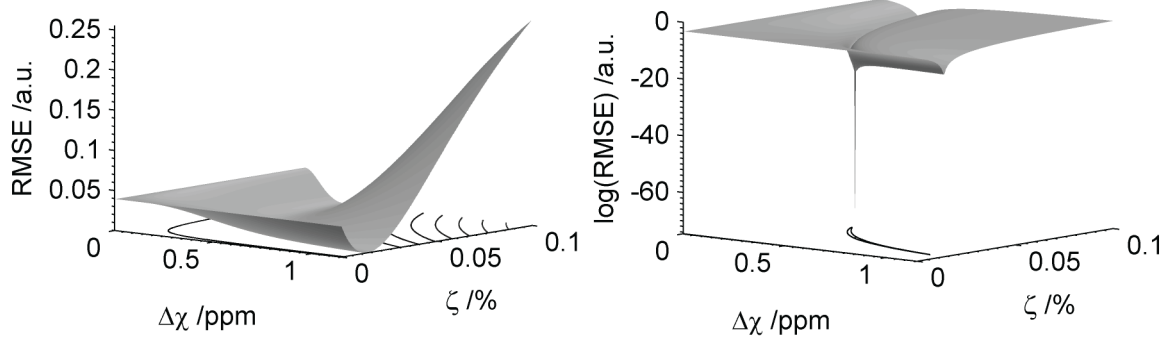


Figure 4.9. Surface plots of root mean squared errors (RMSE) between the signal curve obtained with $\Delta\chi = 1 \text{ ppm}$, $\zeta = 3 \%$ and $R2 = 10 \text{ s}^{-1}$ at $3T$, and all other curves for $\zeta = 0 - 0.1 \%$ and $\Delta\chi = 0 - 2 \text{ ppm}$ in a) linear scale, and b) log-scale.

The choice of sequence parameters could be essential for the outcome of the measurement. For example, it has been previously shown [Bongers, 2004] that a long spin echo time, i.e., compared to $T2^*$, results in more accurate parameter estimation. Using a longer spin echo time results in a more prominent susceptibility weighting, and when using the analytical evaluation method, it allows for larger fitting intervals. However, when using the numerical evaluation method, there is no need to sample the long time asymptote before the spin echo. Hence, there could be a disadvantage to use a longer spin echo time since the SNR is decreasing with increasing spin echo time. During previous attempts to map the oxygen extraction using the method presented in this work, a variety of sequence parameters has been used. However, no definite solution to the optimal sequence parameters has been presented.

To investigate the dependence of the sequence parameters on the possibility to separate $\Delta\chi$ and ζ , without influence of diffusion effects, the static dephasing model was adopted. The MR signal-time development was calculated according to Eq. 3.20 with $\Delta\chi$ set to 0.58 ppm, a ζ of 0.03 and a $R2$ of 12 s^{-1} . Fifteen sequence parameter setups were implemented. The total number of echoes was set to 32 or 64. The number of the gradient echo that coincides with the spin echo was chosen to 8, 12, or 16 in case of 32 echoes, and 8, 16 or 24 in case of 64 echoes. Furthermore, the distance between two adjacent echoes was 2 or 4 ms when 32 echoes was used and 1, 2 or 4 when 64 echoes was used. Noise corresponding to a SNR between 100 and 600 (varied in steps of 100) was added to the calculated signal, which was subsequently evaluated using least square curve fitting. The evaluation was performed using three ($\Delta\chi$, ζ and $R2$), two ($\Delta\chi$ and ζ) and one ($\Delta\chi$) fit parameters. The parameters that were not fitted were given to the fitting routine. The procedure was repeated 500 times for every parameter set.

Dependence on spin echo position

In Figure 4.10, the effect of shifting the position of the spin echo is demonstrated. The results correspond to a GESSE measurement, sampling 64 echoes at an echo distance of 2 ms with the spin echo number chosen to be 8, 16 and 24. The SNR was set to 200. Every point in the scatter plots represents a parameter set obtained when one noisy signal was evaluated. A distribution of parameters is obtained, with the parameter sets located near the valley of low RMSE values. When the number of the spin echo is increased, the obtained parameters are positioned closer toward the bottom of the corresponding valley indicating that the relation between $\Delta\chi$ and ζ can be established with increased confidence. However, when looking at the histogram of the obtained $\Delta\chi$ values, the distribution of the parameter does not show any considerable difference when changing the number of the spin echo. If a Gaussian function is fitted to the obtained $\Delta\chi$ distribution, the standard deviation is 0.13 ppm when the number of the spin echo is 8, 0.11 ppm when the spin echo is the 16th echo, and 0.12 ppm when spin echo is assigned to the 24th echo. This corresponds to a relative parameter error of $18 - 22\%$. To conclude, when both $\Delta\chi$ and ζ are used as fit parameters, the relative parameter error is insensitive to the position of the spin echo. However, if one of the parameters is known, increasing the number of the spin echo will cause a reduction of the uncertainty in the estimation of the other parameter. In the results shown here, the SNR is kept at a constant value of 200. In a real measurement, choosing a later gradient echo as the spin echo often requires the use of a larger echo time and, hence, the SNR would drop if the measurement time were not increased accordingly.

Dependence on the distance between two adjacent echoes

In Figure 4.11, the consequence of changing the distance between two adjacent echoes is demonstrated. The results are related to a GESSE measurement using 64 echoes with an echo distance of 1 ms , 2 ms and 4 ms . The 16th gradient echo is chosen as the spin echo, and the SNR is 200. Essentially the same effect is seen as when the position of the spin echo was altered. Using a small echo distance is equivalent with sampling a small time period, and yields the most spread results. The longer the sampling interval, the more tightly the obtained parameters are positioned in the bottom of the minimum RMSE valley, indicating a less uncertain relationship between the two parameters. However, the distribution of fitted $\Delta\chi$ values does not change substantially. Fitting a Gaussian function to the $\Delta\chi$ distribution, an echo distance of 1 ms gives a standard deviation of 0.14 ppm while 2 ms and 4 ms both yields a standard deviation of 0.11 ms . This corresponds to a relative parameter error of $18 - 24\%$.

Dependence on the total number of echoes

The effect of changing the total number of echoes can be seen in Figure 4.12. The results are pure theoretical and associated with a GESSE measurement using the 16th echo as a spin echo at a SNR of 200. Using 64 echoes instead of 32 while keeping the distance between two adjacent echoes constant (Figure 4.12 (b-c)), results in a lower uncertainty of the relation between $\Delta\chi$ and ζ , but has no major effect on the uncertainty of the individual parameters. Using 32 echoes with an echo distance of 2 ms results in a relative parameter error of 23% while using 64 echoes with an echo distance of 2 ms results in a

relative parameter error of 18 %. However, using 62 echoes with an echo distance of 1 ms yields a relative parameter error of 25 %, the same result as using 32 echoes with an echo distance of 2 ms. Furthermore, using 32 echoes with an echo distance of 4 ms gives a relative parameter error of 18 %, matching the error obtained for 64 echoes with an echo distance of 2 ms. In other words, when comparing 64 echoes with 32 echoes with the double echo distance, i.e. if the total sampling time is constant, the effect on the parameter stability is minimal. Hence, the important parameter seems to be the total sampling period. A large sampling period somewhat increases the stability of the parameter estimation. However, the maximal sampling period and the number of sampling points is limited by the time between the 180° pulse and the spin echo. A longer sampling period requires a longer spin echo time, which would result in a reduced SNR. Hence, the error reduction achieved by using a large fitting area opposes the decreasing SNR. Furthermore, the minimal distance between two adjacent measurement points is dependent on the bandwidth used. Using a small echo distance causes a SNR reduction due to the requirement of increased bandwidth.

Dependence on SNR

Using a later spin echo with a large sampling window stabilizes the parameter estimation. Those actions, however, have to be taken at the expense of SNR. Hence, in order to optimize the sequence parameters, different SNR has to be further considered. In Figure 4.13, the parameters obtained using 64 echoes at an echo distance of 2 ms and the spin echo at the 16th echo, for SNR values of 200, 400 and 600 are shown. A clear improvement in the distribution of the obtained parameters is seen at higher SNR. For $\Delta\chi$, the relative parameter error decreases from 18 % at a SNR of 200 to 7 % at a SNR of 600.

In figure 4.14, the relative error of $\Delta\chi$, ζ and R2 is shown as a function of SNR (32 echoes, echo distance 4 ms, spin echo occurred at 12th echo). The relative error in $\Delta\chi$ and ζ shows a strong SNR dependence. For both parameters, a SNR of 500 is required in order to keep the relative parameter error under 10 %. R2 can be estimated with small relative uncertainty (< 1 %) already at a SNR of 100. However, as can be seen from the scatter plots, if ζ is known, $\Delta\chi$ can be determined with relatively low uncertainty. In conclusion, an accurate value of the susceptibility difference can only be extracted from the measured data if certain conditions are fulfilled. A large uncertainty lays in the simultaneous estimation of $\Delta\chi$ and ζ . To estimate both those parameters at once, an unreasonable large SNR is required. However, if one of the parameters is known the other can be accurately estimated also at low SNR.

Figure 4.15 shows the relative parameter error in $\Delta\chi$ as a function of SNR when ζ is previously known, and used as input parameter to the fitting routine. With prior knowledge of ζ , $\Delta\chi$ can be estimated with a lower uncertainty at a SNR of 100 than could be obtained at a SNR of 600 when both $\Delta\chi$ and ζ were used as fit parameters. At a SNR of 200, which is commonly achieved in a GESSE scan using a measurement time of 15 – 20 minutes, the relative error in $\Delta\chi$ would be 3.2 %. The measurement time required to achieve sufficient SNR to facilitate simultaneous estimation of ζ and $\Delta\chi$ is not accessible in the clinic. Hence, a solution to the problem would be to make a shorter GESSE scan accompanied by an independent measurement of ζ .

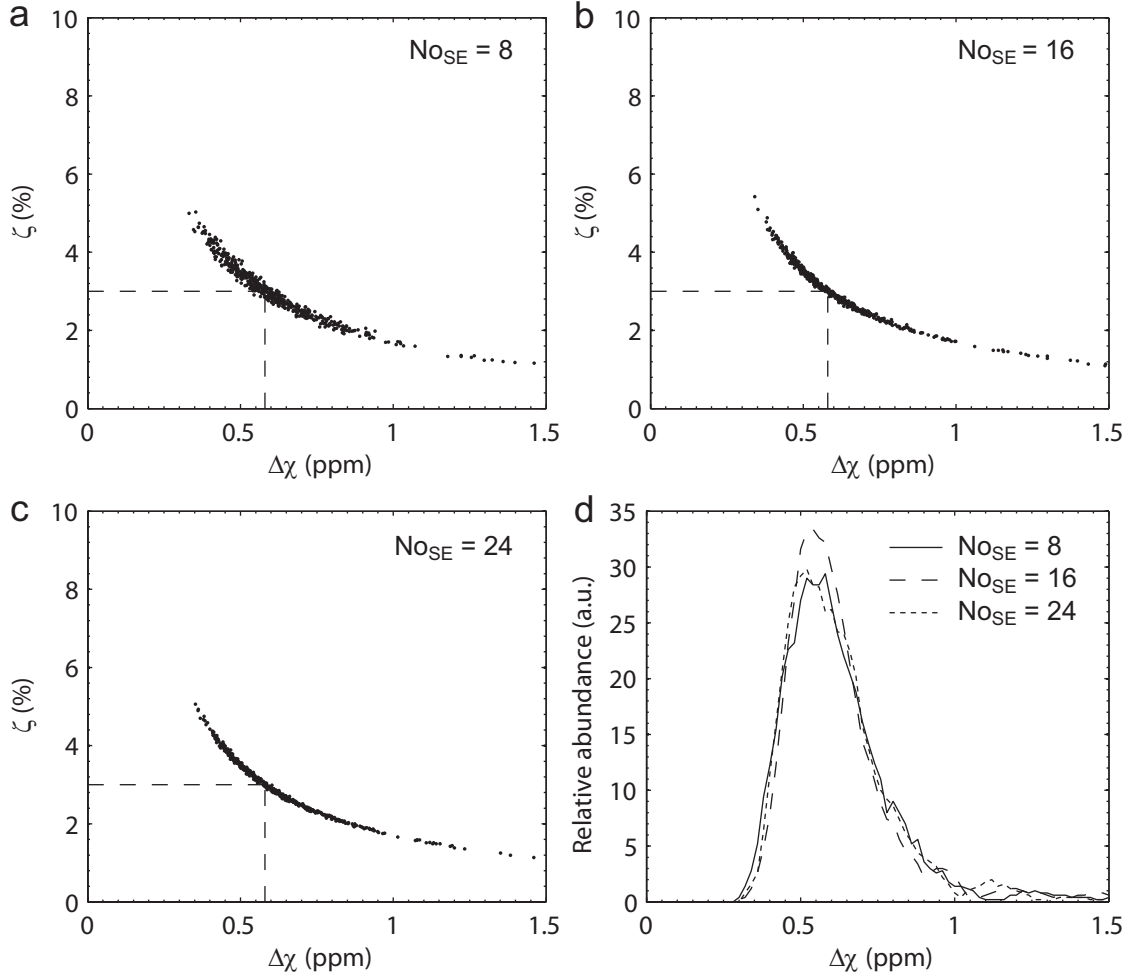


Figure 4.10. Demonstration of the effect on parameter estimation of changing the number of the gradient echo used as spin echo (No_{SE}). For all simulations the SNR was set to 200 and 64 echoes with an echo distance of 2 ms was used. **a)** The obtained sets of ζ and $\Delta\chi$ when evaluating 500 noisy signals and the 8th gradient echo is used as the spin echo. **b)** The obtained sets of ζ and $\Delta\chi$ when evaluating 500 noisy signals and the 16th gradient echo is used as the spin echo. **c)** The obtained sets of ζ and $\Delta\chi$ when evaluating 500 noisy signals and the 24th gradient echo is used as the spin echo. **d)** Histograms of obtained $\Delta\chi$ values when $No_{SE} = 8$ (solid line), $No_{SE} = 16$ (dashed line), and $No_{SE} = 24$ (dotted line). As the number of the gradient echo used as the spin echo is increased, the relation between ζ and $\Delta\chi$ becomes less uncertain. However, when looking at the histogram of the obtained $\Delta\chi$ values, no improvement in the estimation of the single parameter can be seen. Hence, when using both $\Delta\chi$ and ζ as fit parameters, the position of the spin echo is of minor importance. Nevertheless, if one of the parameters is known, the other can be estimated with lower uncertainty by using a later gradient echo as spin echo, under assumption that the SNR is kept constant.

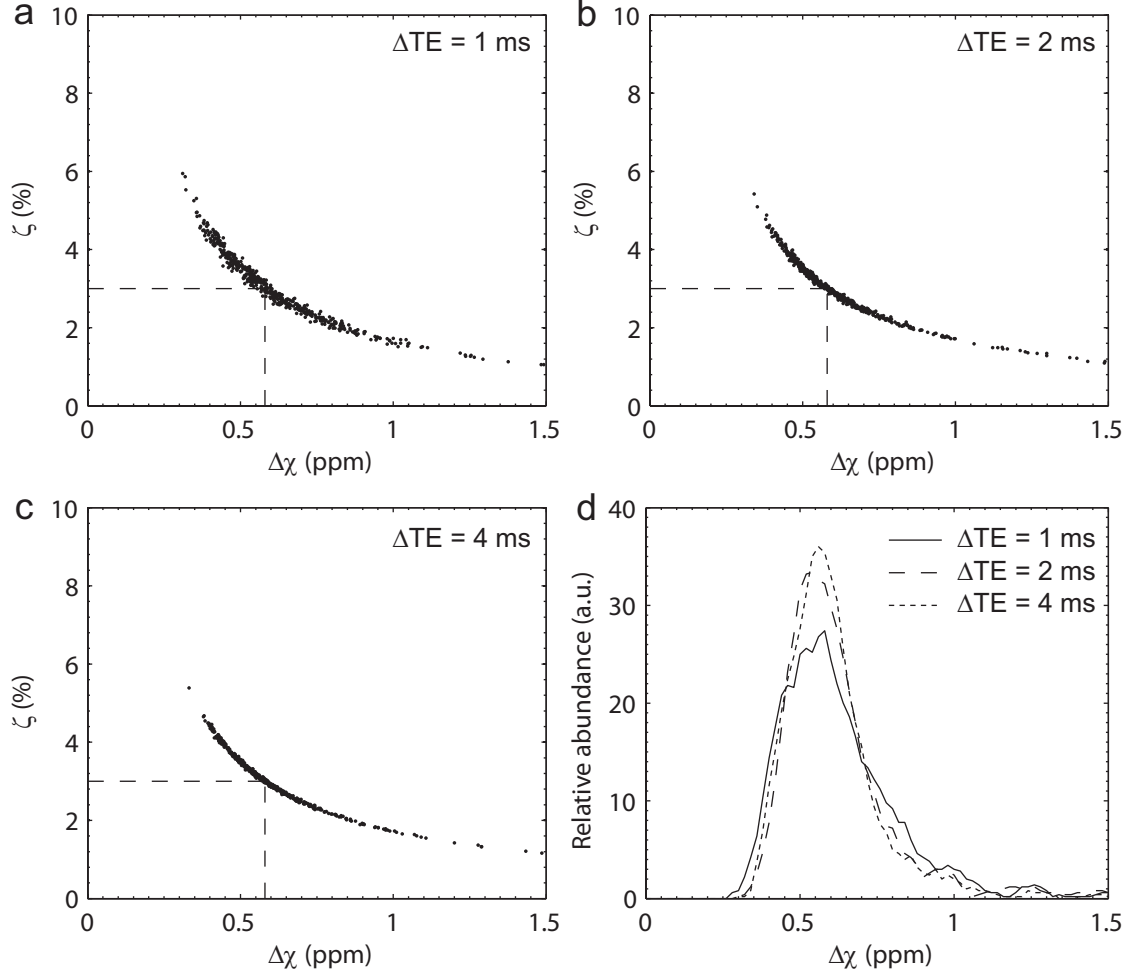


Figure 4.11. Demonstration of the effect on parameter estimation of changing the distance between two adjacent echoes (ΔTE). For all simulations, the SNR was set to 200. 64 echoes were used and the spin echo occurred at the 16th echo. **a)** The obtained sets of ζ and $\Delta\chi$ when evaluating 500 noisy signals and $\Delta TE = 1$ ms. **b)** The obtained sets of ζ and $\Delta\chi$ when evaluating 500 noisy signals and $\Delta TE = 2$ ms. **c)** The obtained sets of ζ and $\Delta\chi$ when evaluating 500 noisy signals and $\Delta TE = 4$ ms. **d)** Histograms of obtained $\Delta\chi$ values when $\Delta TE = 1$ ms (solid line), $\Delta TE = 2$ ms (dashed line), and $\Delta TE = 4$ ms (dotted line). Increasing the echo distance results in a less uncertain relation between ζ and $\Delta\chi$. The histogram in (d) shows that the estimation of $\Delta\chi$ is somewhat stabilized when a larger echo distance is used. This improvement, however, is marginal. On the contrary, if one of the parameters is known beforehand, using a larger echo distance substantially improve the estimation of the other parameter. The previous discussion is only valid if the SNR at the spin echo is kept constant.

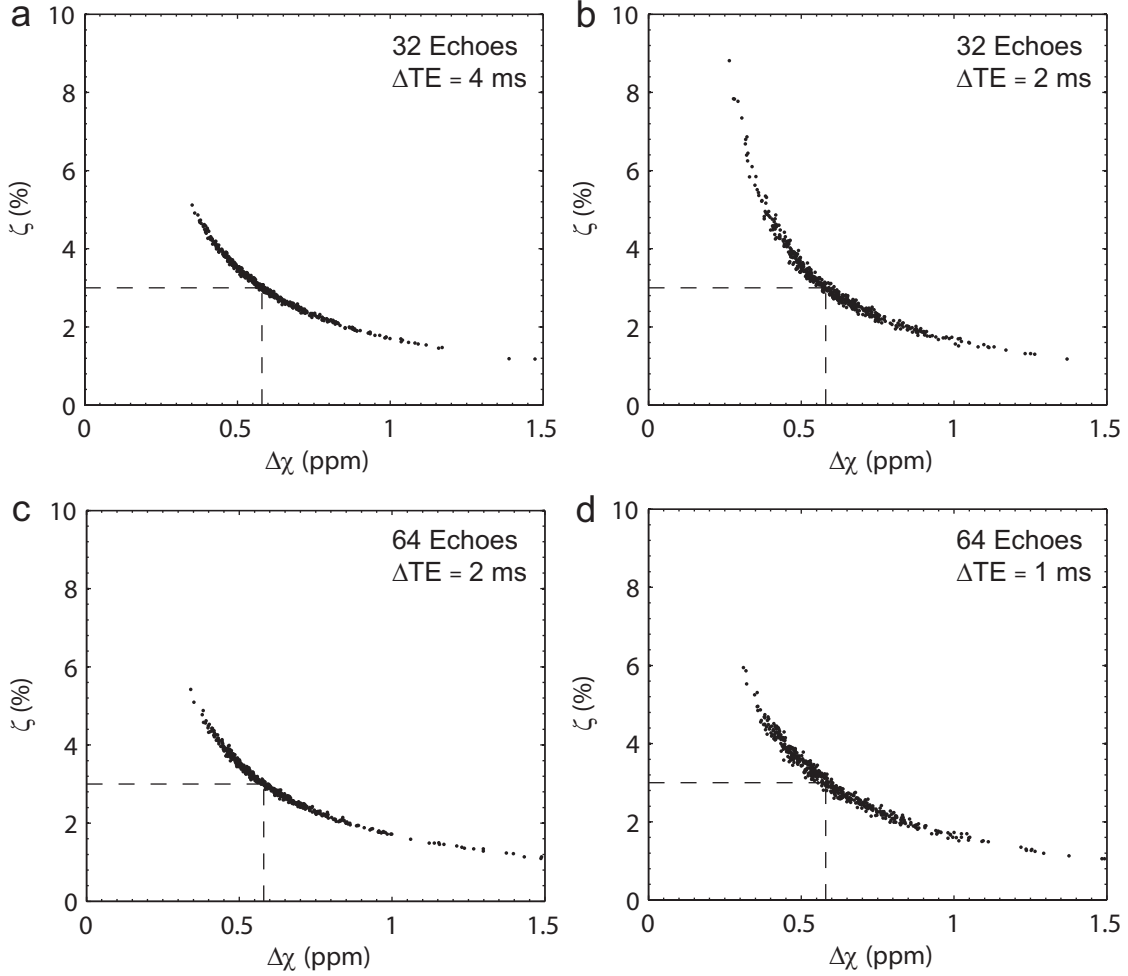


Figure 4.12. Effect on parameter estimation of changing the total number of echoes. For all simulations a SNR of 200 was used. **a)** The obtained sets of ζ and $\Delta\chi$ when evaluating 500 noisy signals calculated using 32 echoes and an echo distance of 1 ms. **b)** The obtained sets of ζ and $\Delta\chi$ when evaluating 500 noisy signals calculated using 32 echoes and an echo distance of 2 ms. **c)** The obtained sets of ζ and $\Delta\chi$ when evaluating 500 noisy signals calculated using 64 echoes and an echo distance of 2 ms. **d)** The obtained sets of ζ and $\Delta\chi$ when evaluating 500 noisy signals calculated using 64 echoes and an echo distance of 1 ms. Using a smaller echo distance for a fixed number of echoes results in a less uncertain relation between $\Delta\chi$ and ζ . Increasing the number of echoes while the echo distance is kept constant has the same effect on the relation between the two parameters as using the double echo distance. However, using the double amount of echoes with half the echo distance does not substantially improve the obtained parameter distribution. Hence, the important parameter is the total sampling time rather than the total number of echoes. However, increasing the sampling time only improves the estimation of the relation between $\Delta\chi$ and ζ . The uncertainty in the single parameters is not significantly improved.

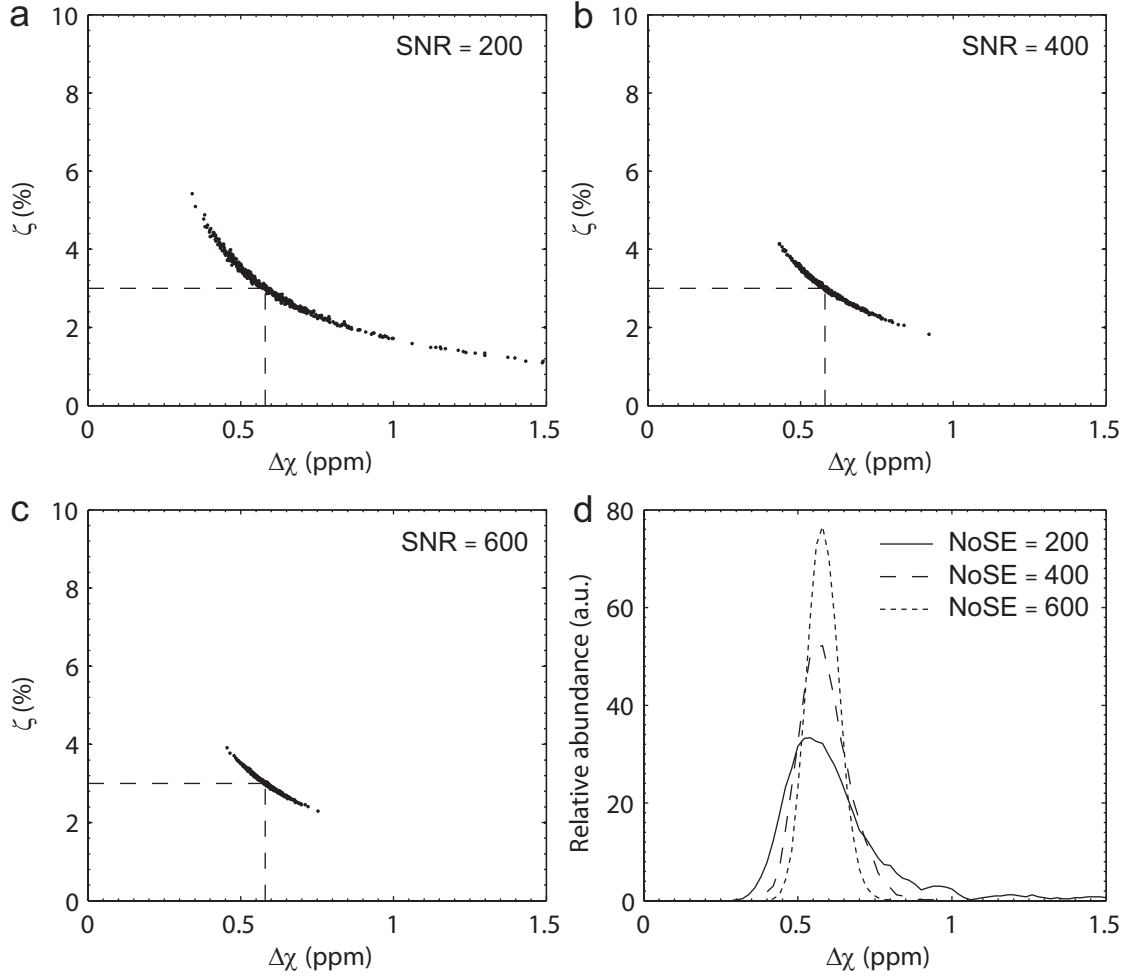


Figure 4.13. Effect on parameter estimation of changing the SNR. For all simulations 64 echoes with an echo distance of 2 ms was used. The spin echo occurred at the 16th gradient echo. **a)** The obtained sets of ζ and $\Delta\chi$ when evaluating 500 noisy signals with $\text{SNR} = 200$. **b)** The obtained sets of ζ and $\Delta\chi$ when evaluating 500 noisy signals with $\text{SNR} = 400$. **c)** The obtained sets of ζ and $\Delta\chi$ when evaluating 500 noisy signals with $\text{SNR} = 600$. **d)** Histograms of obtained $\Delta\chi$ values when $\text{SNR} = 200$ (solid line), $\text{SNR} = 400$ (dashed line), and $\text{SNR} = 600$ (dotted line). Increasing the SNR does not drastically changes the uncertainty in the relation between $\Delta\chi$ and ζ . However, the SNR increase causes a sharp decrease of the uncertainty in the single parameters. Hence, in order to obtain an accurate simultaneous estimation of $\Delta\chi$ and ζ , the SNR has to be increased.

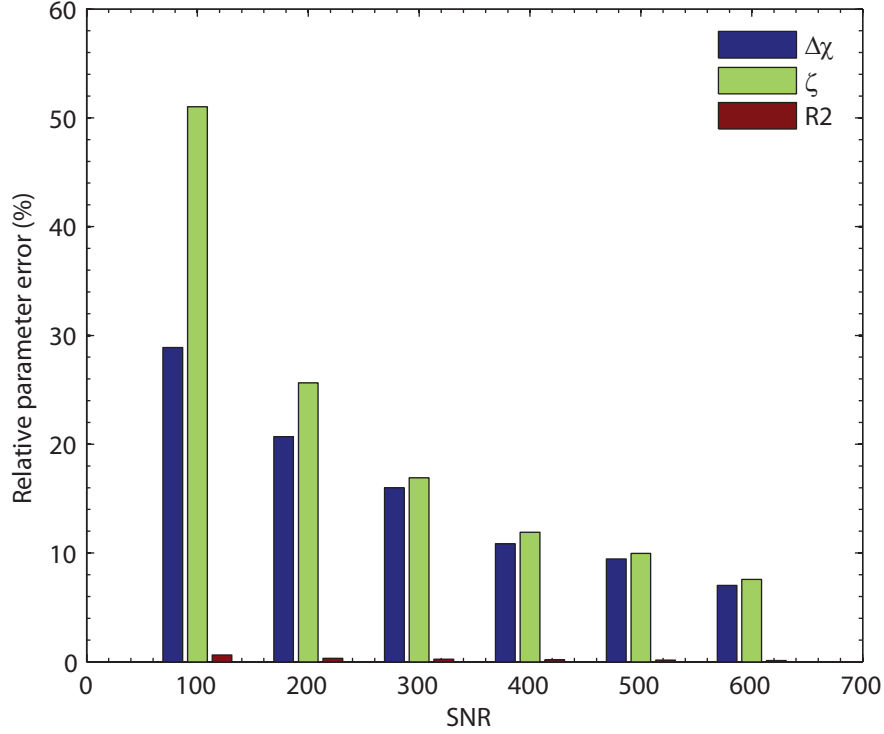


Figure 4.14. Relative parameter error as a function of SNR when $\Delta\chi$ and ζ is fitted simultaneously. (NoSE = 12, $\Delta TE = 4\text{ ms}$, 32 echoes).

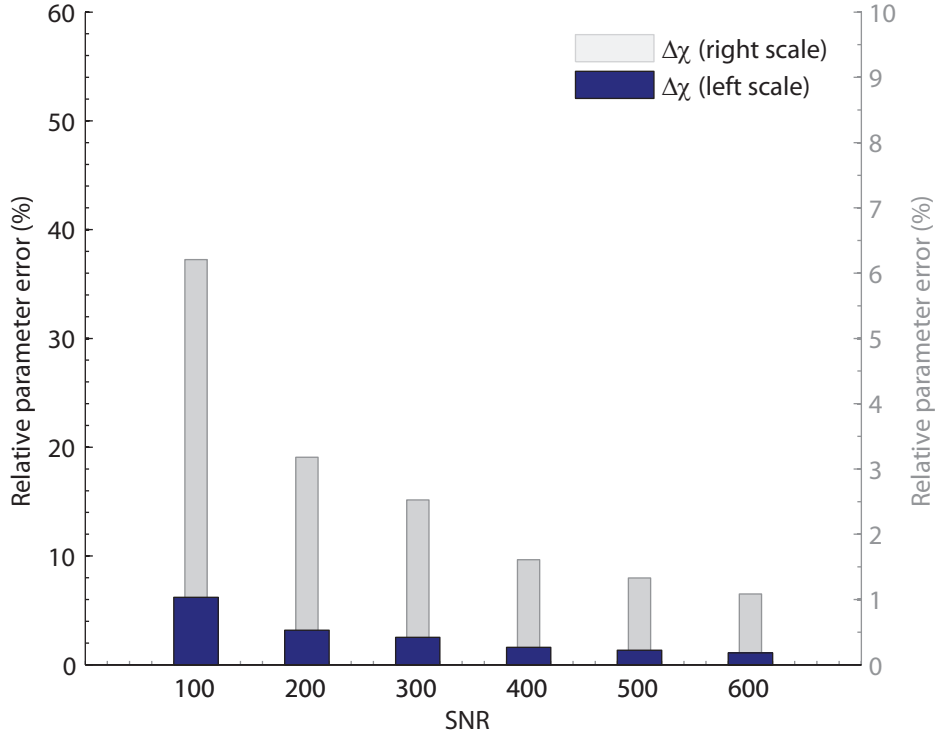


Figure 4.15. Relative parameter error in $\Delta\chi$ as a function of SNR when ζ is previously known. Both bars at a certain SNR refers to the same relative error in $\Delta\chi$. However, the size of the blue bars, which belongs to the left scale, is comparable to the bars shown in Figure 4.14. The grey bars should be used together with the right scale and is added to simplify the reading of the diagram. (NoSE = 12, $\Delta TE = 4\text{ ms}$, 32 echoes).

4.2.3 Expected Effect *in vivo*

Diffusion has a clear effect on the MR signal in string network phantom experiments under the conditions used in this work. At a commonly used echo time of 68 ms, a diffusion effect is seen also for a large string diameter of 245 μm . However, the self-diffusion of water is smaller *in vivo* than in the phantoms used and, hence, the effect is expected to be smaller.

Model the human brain is not trivial. The two-compartment model, describing venous blood vessels as infinitely long paramagnetic cylinders immersed in a homogeneous tissue matrix is undoubtedly an oversimplification. As previously mentioned, several attempts have been made to find models that are more realistic. Intravascular signal as well as a long T2 component, presumably originating from ISF and CSF, has been implemented with promising results [He und Yablonskiy, 2007; He et al., 2008]. However, in addition to signal from ISF/CSF and the intravascular space, diffusion is present and although the effect is small, it will most likely change the outcome of the experiment if it is not accounted for. The major difficulty in modeling diffusion effects is that it depends on the size and distribution of the objects that are causing the field distortions. The true vessel size distribution is in general not known during an *in vivo* measurement, which complicates the attempt to correct for diffusion effects.

In order to estimate the inaccuracy of the parameter estimation for an *in vivo* measurement when the effect of diffusion is neglected, simulations were performed using parameters expected *in vivo*. The ADC was set to $0.8 \cdot 10^{-9} \text{ m}^2/\text{s}$ which is the value expected in gray matter. Furthermore, ζ was set to 3%, $\Delta\chi$ to 0.6 ppm and R2 to 12 s^{-1} . The vessel diameter was set to 50 μm which is larger than expected from known microvasculature anatomy. However, if an effect is seen for 50 μm vessels, it will be even more significant for smaller vessels. The simulations were carried out for a 3 T system and an SNR of 200 was assumed. Data were simulated using both the static dephasing model and the water diffusion model and was subsequently evaluated using the static dephasing model.

The result of the evaluation of the simulated data is shown in Figure 4.16. (a-b) shows the distribution of $\Delta\chi$ and ζ obtained when evaluating static dephasing data (black dots) and water diffusion data (red dots). In (a), the results when using a shorter spin echo time is shown, and (b) shows the results when using a longer spin echo time. For the shorter spin echo time $\Delta\chi$ is $0.67 \pm 0.17 \text{ ppm}$ and ζ is $2.04 \pm 0.69 \%$ when diffusion effects are present but not taken into account at evaluation. Those values can be compared to a $\Delta\chi$ of $0.59 \pm 0.08 \text{ ppm}$ and a ζ of $3.03 \pm 0.61 \%$, which are the values obtained when no diffusion effects are present. For the longer spin echo time $\Delta\chi$ is $0.39 \pm 0.10 \text{ ppm}$ and ζ is $4.11 \pm 1.58 \%$ when the effect of diffusion are not taken into account at evaluation, compared to a $\Delta\chi$ of $0.61 \pm 0.12 \text{ ppm}$ and a ζ of $2.85 \pm 0.77 \%$ which is the values found for the static dephasing signal. Hence, as previously seen relative parameter errors of approximately 20 – 30 % are obtained when both $\Delta\chi$ and ζ are simultaneously fitted.

In agreement with previous simulations, the relation between $\Delta\chi$ and ζ is more well determined when a longer spin echo time is used. In Figure 4.16 (c-d), the distribution of $\Delta\chi$ and R2 values obtained when evaluating static dephasing data (black dots) and water diffusion data (red dots) using a fix ζ are shown. In (c), the results when using a shorter spin echo time and in (d), the results when using a longer spin echo time are presented.

For the shorter spin echo time, the obtained $\Delta\chi$ is $0.52 \pm 0.03 \text{ ppm}$ when analysing the data calculated with diffusion, using the static dephasing model. The corresponding evaluation of static data yields a $\Delta\chi$ value of $0.60 \pm 0.03 \text{ ppm}$. Using a longer spin echo time and data with diffusion results in a $\Delta\chi$ value of $0.51 \pm 0.02 \text{ ppm}$, compared to $0.60 \pm 0.02 \text{ ppm}$ for the data without diffusion. The R2 values obtained for the non-static dephasing data are $12.60 \pm 0.20 \text{ s}^{-1}$ and $12.75 \pm 0.08 \text{ s}^{-1}$ for the shorter spin echo time and the longer spin echo time, respectively. Hence, when diffusion is present this is compensated for during the curve fitting by a slight increase of R2, resulting in an underestimation of $\Delta\chi$. For both GESSE sequences, the mean $\Delta\chi$ is nearly the same. The distribution, however, is much narrower in case of a later spin echo time, where the two distributions are clearly separated. The obtained $\Delta\chi$ values when the non-static dephasing data were evaluated without taking the effect of diffusion into account and both ζ and R2 were fixed to their true values was $0.60 \pm 0.01 \text{ ppm}$ for the shorter spin echo time and $0.54 \pm 0.02 \text{ ppm}$ for the longer spin echo time.

4.3 In Vivo Measurements

FIGURE 4.17 SHOWS parameter maps of ζ , $\Delta\chi$ and R2 obtained at evaluation of a GESSE scan performed at $3T$ using 32 echoes with an echo distance of 4 ms . The spin echo occurred at the 13th gradient echo corresponding to an echo time of 108 ms . A TR of 1500 ms and 6 averages resulted in a scan time of 19 minutes. The SNR was estimated to approximately 100. ζ , which *in vivo* would correspond to the deoxygenated cerebral blood volume (dCBV), is expected to be about 1.5% and 3% in white and gray matter, respectively. However, in the map of ζ values shown in Figure 4.17 (a) no apparent contrast between gray and white matter is visible. Furthermore, the obtained values of ζ are partly much larger than the expected 1.5–3%. In contrast, the $\Delta\chi$ map shown in Figure 4.17 (b) has large areas with values much lower than the anticipated $0.3 - 0.5 \text{ ppm}$. Moreover, the $\Delta\chi$ map is rather inhomogeneous which is not expected from the literature. The darker areas in the ζ map, indicating low dCBV values, match the brighter central areas in the $\Delta\chi$ map, and vice versa. This is in agreement with the simulations in section 4.2 which showed that a signal curve calculated with a small ζ and a large $\Delta\chi$ could be very similar to a signal curve calculated using a large ζ and a small $\Delta\chi$.

The R2 values shown in Figure 4.17 (c) are approximately 15 – 20% larger than the values measured using the CPMG sequence. This inconsistency of T2 values is likely to be caused by diffusion effects. The CPMG sequence has a very short TE of 12.6 ms and, hence, the R2 measurements carried out using this sequence should be practically unaffected by diffusion. The simulations (c.f. figures in Appendix B) showed that when diffusion is present but the evaluation still is performed using the static dephasing model, the R2 is overestimated. The obtained R2 value will be dependent on the vessel size, the diffusion coefficient and the echo time.

Figure 4.18 (a) shows the spin echo magnitude image from the GESSE scan used to produce the parameter maps in Figure 4.17. In the image, an evaluation ROI is marked with a white ellipse. The ROI was positioned in the white matter of the brain where

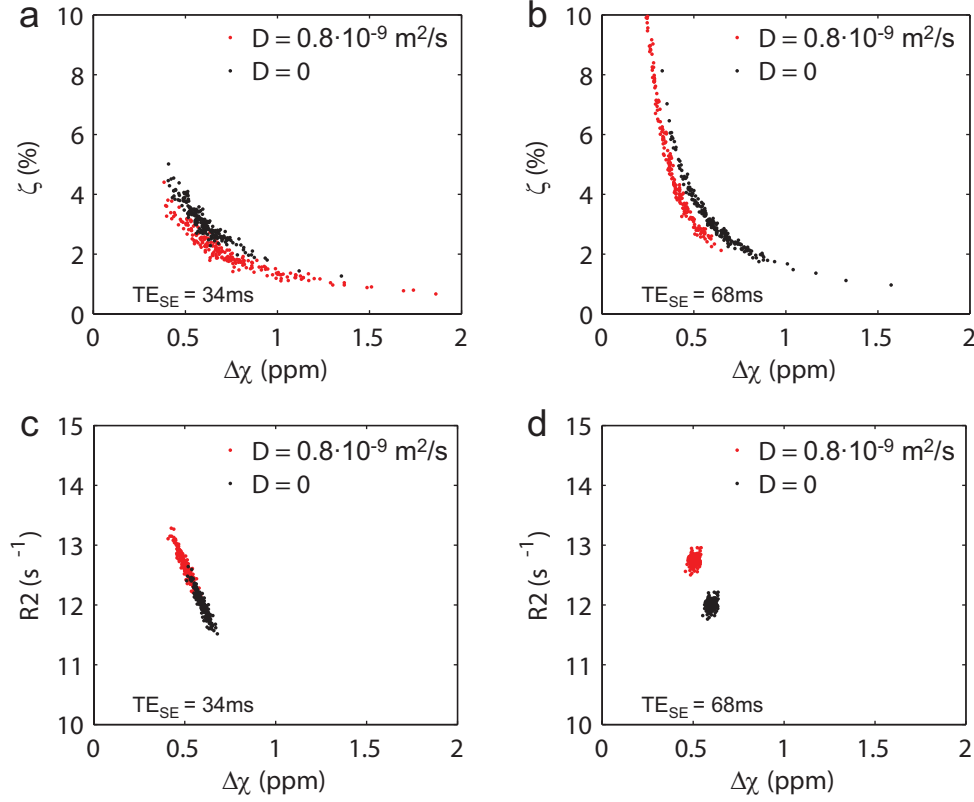


Figure 4.16. Result of evaluation of data simulated with and without diffusion using parameters expected *in vivo* ($\Delta\chi = 0.6 \text{ ppm}$, $\zeta = 3\%$, $R2 = 12 \text{ s}^{-1}$) and an SNR of 200. All evaluations were performed without taking the effect of diffusion into account, in order to estimate the error introduced when signal curves that have a diffusion effect are evaluated using the static dephasing model. **a)** Distribution of $\Delta\chi$ and ζ when three parameters were used as fit parameters and a shorter spin echo time was used. **b)** Distribution of $\Delta\chi$ and ζ when three parameters was used as fit parameters and a longer spin echo time was used. **c)** Distribution of $\Delta\chi$ and $R2$ when ζ was fixed at a value of 3% and a shorter spin echo time was used. **d)** Distribution of $\Delta\chi$ and $R2$ when ζ was fixed at a value of 3% and a longer spin echo time was used.

homogeneous ζ and $\Delta\chi$ are expected. In Figure 4.18 (b), the sets of ζ and $\Delta\chi$ obtained at evaluation of each pixel inside the ROI in Figure 4.18 (a) are shown. The evaluation results in a distribution of parameter sets, similar to the distributions observed during the simulations (section 4.2), corresponding to the valley of low RMSE values. The smaller plot in Figure 4.18 (b) shows a magnified view of the obtained ζ in the range of 0 to 5%. In this view, it can be seen that the ζ values in the range of the expected 1 – 2%, corresponds to $\Delta\chi$ values in the expected range of 0.3 – 0.5 ppm. The distribution of $\Delta\chi$ values obtained when the evaluation is made pixel-by-pixel with a fixed ζ of 1.5% are shown with black unfilled squares in Figure 4.18 (c). The black filled diamonds represent the distribution of $\Delta\chi$ values from Figure 4.18 (a), i.e., the distribution obtained when $\Delta\chi$ and ζ are fitted simultaneously. When ζ is fixed to 1.5% the obtained $\Delta\chi$ values are almost exclusively found in a range of probable *in vivo* values.

The mean signal intensity as a function of echo time in the ROI marked in Figure 4.18 (a) is shown in Figure 4.18 (d). The black solid line represent the fitted curve when both $\Delta\chi$ and ζ are used as fit parameters. Such a small $\Delta\chi$ value as the 0.17 ppm obtained when $\Delta\chi$ and ζ are fitted simultaneously is not realistic *in vivo*. The value of 0.37 ppm obtained when ζ is fixed at 1.5% is more in agreement with the expected susceptibility difference. Nevertheless, the plotted curves once again illustrate the disadvantageous feature that several sets of $\Delta\chi$ and ζ results in more or less identical signal curves. Even though $\Delta\chi$ differs with 0.2 ppm , it is not possible to distinguish between the two curves. Hence, a simultaneous determination of the two parameters can be excluded with present *in vivo* data.

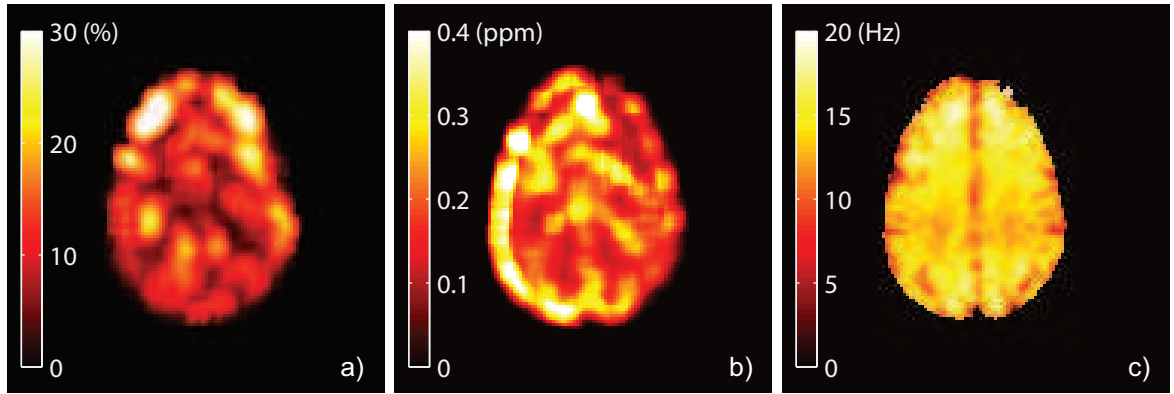


Figure 4.17. Parameter maps obtained when evaluating *in vivo* data acquired at $3T$ using 32 echoes with an echo distance of 4 ms , the spin echo occurred at the 13th gradient echo (118 ms). The evaluation was done using the static dephasing model and 3 fit parameters. **a)** Deoxygenated cerebral blood volume (dCBV) map, **b)** susceptibility difference ($\Delta\chi$) map and, **c)** R2 map. The dCBV is expected to be approximately 1.5% in white matter and about 3% in gray matter. The dCBV map in (a) does not show any clear contrast between gray and white matter and has values much larger than expected. The $\Delta\chi$ map is expected to be homogeneous and have values in the order of $0.3 - 0.5\text{ ppm}$. Instead of a homogeneous $\Delta\chi$ map, the evaluation results in a rather inhomogeneous map with many pixels having a $\Delta\chi$ value much lower than 0.3 ppm . The darker areas in (a), indicating small dCBV values, agree with the bright areas in (b), indicating high $\Delta\chi$ values. This is in agreement with the simulations in section 4.2 that showed that many sets of volume fraction and $\Delta\chi$ produced very similar signal curves. The parameters that cause similar signal curves corresponded to a low volume fraction and a large $\Delta\chi$, a high volume fraction and a small $\Delta\chi$ or an intermediate volume fraction and $\Delta\chi$. The R2 values obtained at evaluation are approximately $15 - 20\%$ larger

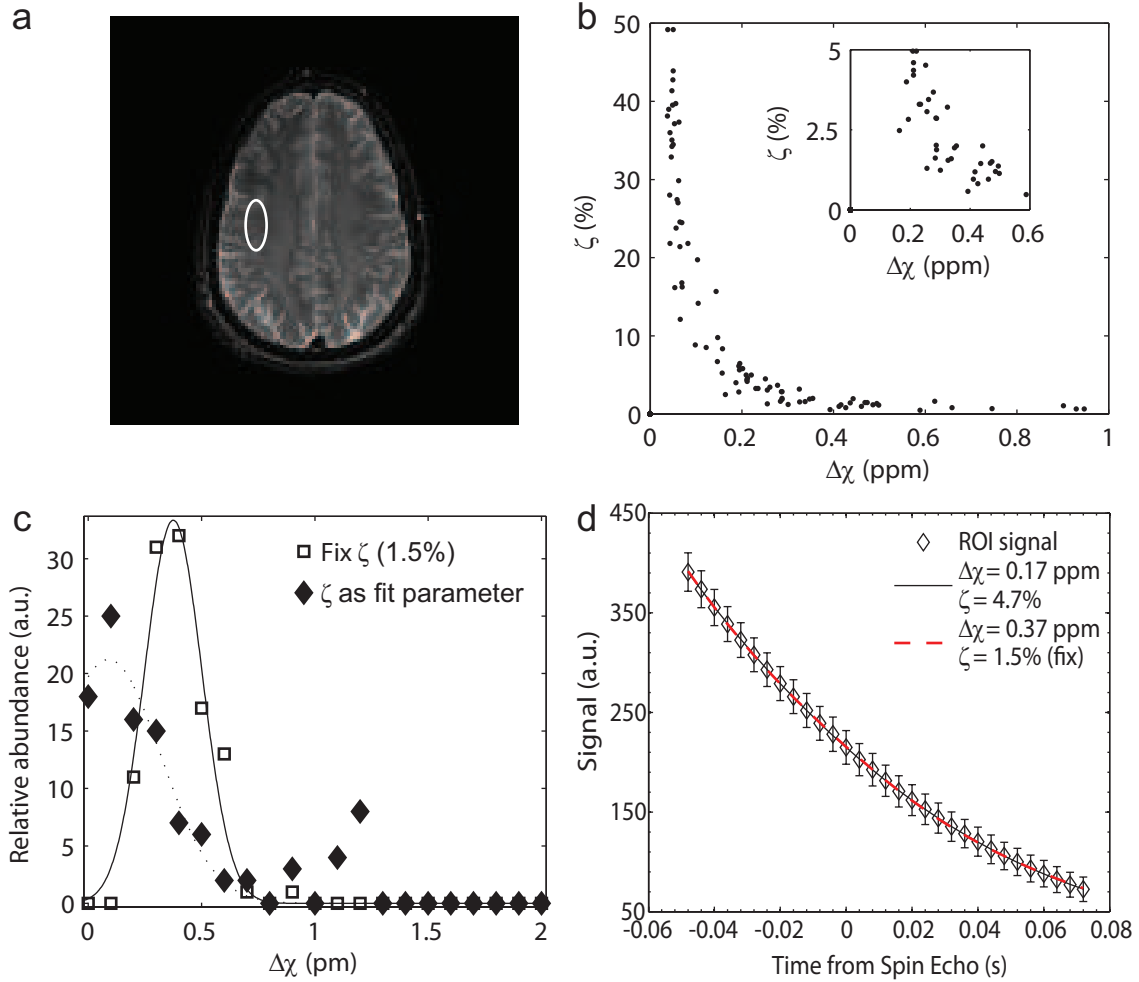


Figure 4.18. **a)** Magnitude image from the GESSE sequence at the spin echo ($TE_{SE} = 108\text{ ms}$), with the evaluation ROI marked in white. **b)** Sets of $\Delta\chi$ and ζ values obtained by individual evaluation of every pixel in the ROI marked in (a). Although a constant ζ and $\Delta\chi$ is expected, the evaluation results in a distribution of values, similar to the distribution seen from the simulations (section 4.2). The smaller plot offers a magnified view of ζ values from 0 to 5%. In this magnified view it can be seen that when ζ is in the range of the expected 1–2%, the corresponding $\Delta\chi$ takes values of 0.3–0.5 ppm which are the values expected in the brain. **c)** Histogram of the obtained $\Delta\chi$ values when using both $\Delta\chi$ and ζ as fit parameters (filled diamonds) and when ζ is fixed to 1.5% (squares). When $\Delta\chi$ and ζ are fitted simultaneously, the majority of the found $\Delta\chi$ values does not correspond to the expected values of 0.3–0.5 ppm. If, however, ζ is fixed to 1.5% the obtained $\Delta\chi$ values are almost exclusively found in the expected range. **d)** Mean signal from the ROI marked in Figure 4.18 (a) and the fitted signal curves when both $\Delta\chi$ and ζ are used as fit parameters (black solid line) and when a fixed ζ of 1.5% is used (red dashed line). Even though there is a large difference between the two $\Delta\chi$ values, the fitted curves are practically impossible to tell apart. Hence, a stable simultaneous estimation of $\Delta\chi$ and ζ is very hard to accomplish under *in vivo* conditions.

Modification of the oxygenation saturation

As alluded to above, many problems need to be solved in order establish a reliable method for quantitative tissue oxygenation measurements. The major problem appears to be the simultaneous estimation of ζ and $\Delta\chi$. To solve this, an independent measurement of ζ has to be performed. Furthermore, diffusion is expected to influence the measurement. In order to consider diffusion the vessel size distribution has to be estimated, which is not a straightforward procedure. Another large difficulty in the validation of the *in vivo* measurements is the absence of exact reference values. However, by modification of the oxygenation saturation a relative change could be detected. Such a relative measurement could give a suggestion of the sensitivity of the method.

Caffeine intake, reduces the cerebral blood flow in the brain [Cameron et al., 1990; Field et al., 2003]. In order for the oxygen consumption of the brain to stay constant, more oxygen has to be extracted from the blood. The result is an accumulation of deoxyhemoglobin in the veins and, hence, a larger $\Delta\chi$.

A 27 years old male healthy volunteer was measured with the GESSE sequence ($B_0 = 3\text{ T}$, 32 echoes, $\Delta\text{TE} = 4\text{ ms}$, $\text{No}_{SE} = 13$, $\text{TE}_{SE} = 108\text{ ms}$, $\text{TR} = 1500\text{ ms}$, 6 averages) before and 1 hour after oral intake of 200 mg caffeine (Coffeinum N 0,2 g tablets, Merck dura GmbH, Darmstadt, Germany). Susceptibility weighted images were acquired directly after each GESSE scan. Susceptibility weighted imaging (SWI) is an imaging technique that combines both the magnitude and the phase information in the MR signal for noninvasive cerebral venographic imaging. The method was first applied by Reichenbach et al. [1997] and was later called SWI by Haacke et al. [2004]. In the SWI images, the effect of caffeine on the amount of deoxyhemoglobin in the veins should be directly observable.

Figure 4.19 (a-b) shows the SWI images before and 1 hour after caffeine intake, respectively. As indicated by the red arrows in Figure 4.19 (b), the veins are more distinct in the SWI image acquired after caffeine intake, indicating that more deoxyhemoglobin is present in the veins. An evaluation ROI was positioned in an area where strong susceptibility effects were seen. Larger veins were avoided. Figure 4.19 (c) shows the corresponding signal decays, of the ROIs shown in (a) and (b), measured with the GESSE sequence. The signal is shown in logarithmic scale to facilitate a comparison between the two curves. After caffeine intake (unfilled squares), the signal has a higher relaxation rate, indicating an increased amount of deoxyhemoglobin. Using a fix volume fraction of 3%, evaluation of the two signal curves results in a $\Delta\chi$ change of 0.12 ppm. This result is in agreement with measurements performed by Sedlacik et al. [In Press, Corrected Proof] who did quantitative oxygenation measurements on a single vein using the single cylinder method presented in section 3.3.2. Consequently, the method shows a sensibility to changes in the venous oxygen saturation which is promising for further studies.

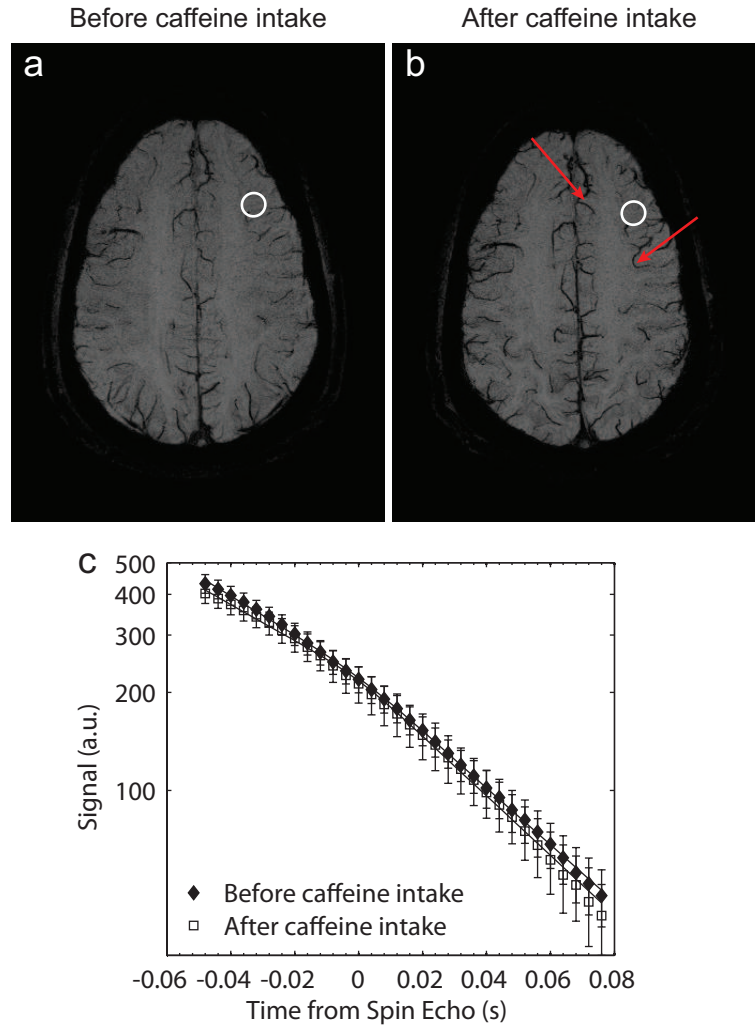


Figure 4.19. **a)** Susceptibility weighted image (SWI) of a healthy volunteer before caffeine intake. **b)** Susceptibility weighted image (SWI) of a health volunteer after caffeine intake. A larger contrast between the large veins and the surrounding tissue (red arrows) is present than before caffeine intake (a). The extra contrast is due to the enhanced susceptibility effect caused by an increased amount of paramagnetic blood in the veins. The increased susceptibility difference between the veins and the surrounding tissue should affect the signal decay and, hence, be observable in a GESSE scan. **c)** Measured signal decay in the ROI marked in (a-b) before caffeine intake (filled diamonds) and after caffeine intake (squares). After caffeine intake a more rapid signal decays is present. This is expected since the caffeine contributes to a higher oxygen extraction which, increases the amount of paramagnetic blood in the veins.

V

Discussion

Network Phantom

The static dephasing model [Yablonskiy und Haacke, 1994] and the water diffusion model [Kiselev und Posse, 1999], both assume statistically distributed and randomly oriented cylinders in a homogeneous medium. In order to verify the models, measurement phantoms that mimic this geometry were constructed. Monofilamentous polyamide strings are suitable for phantom construction since they are homogeneous and available in diameters that cover a large range of the capillary diameters. However, even though a relatively small string filled compartment ($\varnothing = 48\text{ mm}$) was used in the phantoms, the string length required for a reasonable volume fraction of $2 - 5\%$ is several kilometers in case of a string with a diameter of $27\text{ }\mu\text{m}$. To coil the strings, obeying the properties of the model, i.e., statistically distributed and randomly orientated, is not straightforward. Hence, errors are likely to be present due to dissimilarities between the measurement and the theoretical geometry. Since the evaluation of the phantom measurements is performed in ROIs covering a large part of the string-filled compartment, the effect of the inhomogeneously coiled strings is expected to be balanced out. However, this may be true for the static dephasing situation but in case of water diffusion, the result is dependent on the exact vessel radius distribution, and the effect of inhomogeneously coiled strings will not average out by using the mean signal in a ROI. Hence, the errors introduced in the measurements due to inhomogeneous coiling of the strings are likely to be more prominent for the measurements where a strong water diffusion effect is present.

Macroscopic Field Inhomogeneities

The method presented in this work aims to estimate the oxygenation saturation in the veins by measurement of the field gradients caused by the paramagnetic vessels inside a voxel. Macroscopic field inhomogeneities could be assumed to cause an additional, constant magnetic field gradient in each measurement voxel. A constant field gradient applied during the signal read out causes an additional sinc-shaped signal decay that will be overlaid on

the MR signal. If this additional signal loss is not properly corrected for, incorrect values of ζ and $\Delta\chi$ will be obtained at the evaluation. A well-shimmed imaging slice, together with proper positioning, is the best way to avoid macroscopic field inhomogeneities. Positioning the slice in a region unaffected by the field inhomogeneities caused by the frontal sinuses and the nasal cavity can be done in case of pilot measurements. However, in the event of patient measurements, the position of the slice cannot be arbitrarily chosen and there is a risk that a scan has to be made in a region strongly affected by field inhomogeneities. Furthermore, careful shimming is very time consuming and, hence, improper for the already long GESSE measurement. Correction of the inhomogeneity effect subsequent to the measurement would make a quick, basic shimming during the measurement sufficient. Using a thin imaging slice helps to minimize the effect of macroscopic field inhomogeneities but on the expense of SNR or measurement time.

If the field inhomogeneities are small, the sinc-shaped signal decay can be approximated with a Gaussian function. Previous studies [Yablonskiy, 1998; Bongers, 2004] employed a correction for macroscopic field inhomogeneities by combining this analytical expression with the analytical expression that exist for the long time asymptotes of the static dephasing model. However, this method can only be used if an analytical expression for the signal decay is present, which is not the case for the water diffusion model or the extended model including intravascular signal and signal from ISF/CSF. Furthermore, the correction using the quadratic exponential term was shown to be extremely sensitive to low SNR [Bongers, 2004].

An alternative to the use of the analytical, quadratic exponential correction is to estimate the macroscopic field inhomogeneities using high resolved phase images [Jezzard und Balaban, 1995; Irarrazabal et al., 1996]. Such phase maps can be straightforwardly produced using a 3D gradient echo sequence. When the macroscopic field inhomogeneities inside the voxel are known, the expected, additional signal loss can be numerically estimated and a correction of the original data can be achieved. In this work, investigation of this correction method was performed in phantom measurements, which showed that signal loss caused by macroscopic field inhomogeneities could be consistently corrected for.

The large advantage of the correction method used in this work is the use of a separate 3D GRE scan. Since the macroscopic inhomogeneity correction is preformed prior to the data evaluation, it is independent on the evaluation method used. Hence, it can be used together with any measurement technique or data evaluation technique. Since the water diffusion model used in this work, does not have an analytical signal expression this is an essential characteristic of the correction method.

Single Cylinder Measurements

The single string measurement performed in this work aimed to serve as a reference to the network phantom measurements. While the exact cylinder network geometry can be hard to accomplish in a phantom, the single cylinder geometry is uncomplicated to mimic and the results obtained by the single cylinder measurements can be assumed accurate. An analytical solution to the MR signal formation from a voxel containing a

single magnetized cylinder can be found in Yablonskiy und Haacke [1994]. This solution, however, is derived for a single cylinder coaxial with a cylindrical measurement voxel. To derive an analytical solution for other voxel geometries is not straightforward. However, in a standard measurement, square voxels are used and, hence, an alternative solution has to be found. The numerical simulation used in this work, developed by Sedlacik et al. [2007], allows for consideration of arbitrary voxel geometries. Furthermore, Sedlacik et al. [2007] showed that considering square voxels is not enough to simulate an authentic measurement. In a real measurement, the k-space cannot be sampled to infinity, which means that the point spread function has to be considered as well. Discrepancy of up to 100 % can be found between results obtained using a cylindrical voxel or a square voxel with PSF [Sedlacik et al., 2007]. The large advantage of this method is the applicability for any object as long as the associated magnetic field disturbance can be calculated. Sedlacik et al. [2007] showed that the method could be used with promising results in estimating the oxygenation saturation in a single vein oriented perpendicular or parallel to the imaging slice.

The numerically simulated signal was in good agreement with the measured signal for all single string phantom measurements. To evaluate the outcome of the measurement, the result can be compared with the literature values. Rákoš et al. [1966] measured the susceptibility of polyamide strings to a value of $-4\pi \cdot 0.766 \text{ ppm}$. Furthermore, they found that when the string is elongated its susceptibility decreases. For an elongation of 50 % the susceptibility drops to $-4\pi \cdot 0.811 \text{ ppm}$. In the single string measurements performed in this work, a deviation between the two string diameters was seen. One explanation to this could be that the thinner, $194 \mu\text{m}$, string becomes slightly more elongated when the phantom is built. When the phantom is constructed the single strings is slipped through two holes at the side of the bottle and tied together at the back. According to the manufacturer, the difference in the average extension between the $245 \mu\text{m}$ string and a $63 \mu\text{m}$ string is 29 %. Specification for the $194 \mu\text{m}$ string was not available. However, it is reasonable to expect a difference. Since the NiSO_4 solution is more paramagnetic than the polyamide strings, a decreased susceptibility of the strings would correspond to an increased susceptibility difference between the strings and the solution, which is in agreement with the results. If a linear relation between the elongation and the susceptibility change is assumed, the difference between the result obtained by the $194 \mu\text{m}$ sting and the $245 \mu\text{m}$ string would correspond to an elongation difference of 7 %. Another, more likely solution is that the two strings simply have different susceptibility due differences in the bulk material (e.g. color additives etc.). By using additional string diameters for the single string measurements, it would have been straightforward to conclude if the variation in susceptibility between the different string diameters is systematic or appears random. However, due to the restricted spatial resolution of the whole-body scanner, the accuracy of a measurement performed with a thinner string could be doubted. The better choice would have been to perform additional measurement using a thicker string. However, when the experiments were performed, no thicker string was available.

Using the literature value for the volume susceptibility of NiCl in water the susceptibility of NiSO_4 solutions of different concentrations can be calculated (c.f. section 3.2.3.3). For a solution containing $3 \text{ g/l NiSO}_4 \cdot 6\text{H}_2\text{O}$, as in phantom III and IV, the calculated susceptibility would be $-4\pi \cdot 0.664 \text{ ppm}$. Assuming a susceptibility of $-4\pi \cdot 0.766 \text{ ppm}$ for the

polyamide strings, the expected susceptibility difference is 1.28 ppm . This value is 20–30 % higher than the values obtained in the single string measurement. For a $\text{NiSO}_4 \cdot 6\text{H}_2\text{O}$ concentration of 3.75 g/l (phantom II) the calculated susceptibility difference would be 1.39 ppm compared to the measured $1.11 - 1.20 \text{ ppm}$, and for 4 g/l $\text{NiSO}_4 \cdot 6\text{H}_2\text{O}$ (phantom I) the calculated value is 1.44 ppm in contrast to the measured $1.19 - 1.28 \text{ ppm}$.

It is not straightforward to validate which value that corresponds to the true susceptibility difference. The single string measurement has several potential error sources. The precise angle between the string and the B_0 field was always assumed 90° . Careful positioning of the phantom and supervision by means of localizer scans was employed to ensure that this assumption holds. However, if this is not the case minor errors may be introduced. Furthermore, the relaxation rate of the NiSO_4 solution increases with the NiSO_4 concentration. Hence, there are not much signal left during the last sample points for the 5 g/l and 7 g/l measurement. Since the signal from the string containing voxel is divided by the surrounding, homogeneous signal, the signal appears to rebuild a maximum with higher amplitude than the previous maximum. This is not true, but only an effect of dividing two signals with extremely low amplitude. Those points, however, become a very low weighting factor during curve fitting due to their large relative error and do not affect the outcome of the evaluation. Additionally, numerical errors may be introduced because of the discretization. This effect, though, has been shown to be negligible [Sedlacik et al., 2007]. Finally, a potential error source could be the sub-voxel shift applied to position the string in the center of the voxel. If this re-positioning fails, false results will be obtained.

Evaluation Technique

Previous attempt to measure tissue oxygenation and deoxygenated blood volume with the GESSE approach have been made using the asymptotes of the MR signal around the spin echo and at long GRE time [Yablonskiy, 1998; An und Lin, 2000; An et al., 2001; An und Lin, 2002]. However, the analytical method has a number of disadvantages compared to the numerical method. In the analytical method, only the measurement points located in the long time area and the signal at the spin echo is used for parameter estimation. Consequently, extrapolation is required in order to estimate the volume fraction, a procedure that is highly SNR sensitive. The data sampled at long echo times can only determine the $R2'$, which is proportional to the product of ζ and $\Delta\chi$. In order to separate the effect of ζ and $\Delta\chi$, the signal intensity at the spin echo has to be accurately estimated. Hence, the accuracy of the independent ζ and $\Delta\chi$ measurement is determined mainly by the SNR and the number of sampling points within the long time region. In contrast, in the numerical method, all measurement points are included in the curve fit and no extrapolation or detours over additional parameters are required. Additionally, the need to sample the long time asymptote before the spin echo vanishes when using the numerical method, which allows for shorter spin echo time and increased SNR. For both approaches, problems arise when ζ is close to zero. In the analytical approach, the sought susceptibility difference is calculated as the quotient of $R2'$ and ζ . When ζ is estimated to zero or very close to zero, huge errors may result from this operation. The numerical method is more stable and does not yield those enormous errors. However, since ζ and the characteristic function, which is

dependent on $\Delta\chi$, appears as a product in the exponent, if one of them is set to zero, the other one can be just any number. Hence, when no effect is present, the fitting routine will give a value of zero for one of the parameters and some other number, probably the start value, for the other. This can be misleading if the two parameter maps are not revised simultaneously.

Nevertheless, the analytical method may work fine in phantom experiments at high SNR. However, as emphasized by He und Yablonskiy [2007], during a *in vivo* measurement the signal during a spin echo may be considerably contaminated by lipids and metabolites in the tissue and, hence, substantial errors can be introduced into the estimation of ζ if this is not modeled for. Since multiple R_2 relaxation rates are present, this error would depend on the spin echo time. Hence, when the analytical method is used *in vivo* without considering multiple T_2 decay components, the estimated R_2' will depend on the chosen fitting interval [Fujita et al., 2003], leading to errors in the estimated susceptibility difference.

The numerical method allows a more realistic brain model to be used. Since there are no needs for analytical asymptotes, diffusion, intravascular signal and signal from ISF/CSF can be modeled. The main disadvantage of the numerical method is that the evaluation is extremely time-consuming due to the iterative process. However, if the progress in hardware development continues at the same pace this should not be a problem in the future

Cylinder Network

The evaluation of the cylinder network phantom measurements was performed using the signal from a large ROI in the string-filled compartments. This was done in order to achieve better statistics and to compensate for inhomogeneous packing of the strings. If areas with artifacts from air bubbles were found, they were excluded from the ROI.

Using the static dephasing model for evaluation, measurements performed with the $89\,\mu\text{m}$ and the $245\,\mu\text{m}$ phantom generally yield $\Delta\chi$ values closer to the reference values than measurements performed with the $27\,\mu\text{m}$ and the $63\,\mu\text{m}$ phantom (Table 4.2). Especially for long echo times, the $27\,\mu\text{m}$ and the $63\,\mu\text{m}$ phantom generates unreasonable results. The effect increases with decreasing string diameter, indicating that it probably is a diffusion effect. Analyzing the results from the $245\,\mu\text{m}$ phantom, proper parameter values are obtained for all measurements except when a longer spin echo time is used at $3\,T$. For the $89\,\mu\text{m}$ phantom, both measurements using a shorter echo time results in proper results. Using a longer spin echo time, none of the measurements produces accurate results. The deviation from the reference value is larger for $3\,T$ than for $1.5\,T$. For the $27\,\mu\text{m}$ and the $63\,\mu\text{m}$ phantom, short echo time and low magnetic field strength seems to yield reasonable results, whereas the outcome from all other measurement seems illogical. The effect of diffusion seems to be more prominent at higher field strengths. This contradicts the statement of He und Yablonskiy [2007] that the effect of diffusion turns insignificant at higher field strengths.

However, when using the water diffusion model for evaluation, no better results are ac-

complished. Only for phantom IV, the incorrect estimation for long echo times at $3T$ is corrected for. Looking at the measurements using the $89\mu m$ phantom, the results for short echo times shows a too small $\Delta\chi$, whereas the results for the long echo time overestimates $\Delta\chi$ when using the water diffusion model. The same effect is seen for the $63\mu m$ phantom, only stronger. Evaluation of the measurements with the $27\mu m$ phantom, using the water diffusion model, produces no consistent results.

Accurate results could not be achieved for all string diameters, even if the diffusion model was used. However, the effects seen in the phantom measurements are similar to the effects predicted by the water diffusion model. The RMSE between a measured signal curve where a large diffusion effect is expected and the curves predicted by the static dephasing model shows that the theoretical signal decay calculated with the expected parameter shows small resemblance to the measured curve. On the other hand, when the root mean squared error is calculated for the water diffusion model, a low RMSE value is often obtained for the expected set of $\Delta\chi$ and ζ . When evaluating the data using the water diffusion model both the string diameter and the apparent diffusion coefficient appears as input parameters to the routine. In order to compare the evaluation using the static dephasing model with the evaluation using the water diffusion model, the number of fit parameters should be kept constant. Hence, the string radius and the ADC have to be given to the routine. The string radius used is the one provided by the manufacturer for each string size and the ADC is measured as described in section 3.2.2.2. Hence, minor deviations may be introduced via those parameters, but not to such extent that the results can be explained. On the other hand, the water diffusion model may be more sensible to the packing of the strings. Both methods assume statistically distributed strings than the static dephasing model. If several strings clutch together they will appear as one thicker string. If this is the case, the diffusion sensitive measurements (longer echo time, smaller string diameter) will be most affected. Furthermore, when evaluating the signal curves with shorter echo time a smaller parameter error is generally obtained than for the signal curves with the longer echo time. This is because when diffusion is present, the deviation from the static dephasing case is more prominent before the spin echo. For the shorter echo time, fewer echoes are sampled before the spin echo and, hence, a smaller deviation from the modeled curve is expected when comparing this curve with the static dephasing model than for the longer echo time.

Despite the ambiguity in the parameter evaluation using the water diffusion model. The phantom measurements performed in this work can be used as a verification of the water diffusion model as it was proposed by Kiselev und Posse [1999].

Little consideration has been given to the obtained ζ values. This is because the subject of this work is to find a method where $\Delta\chi$ (should be read as “oxygenation saturation”) can be estimated with enough accuracy. If there is a possibility to simultaneously obtain ζ this is of course even more satisfying. However, from the results of this work it seems that an independent estimation of ζ is required in order to accurately estimate $\Delta\chi$. The ζ values present in Table 4.2 is rather close to the expected values when $\Delta\chi$ is close to the expected value. The true ζ in the ROI, however, is in practice not known. The relative volume fraction to the whole compartment is known, but due to inhomogeneous packing of the strings, the relative volume fraction is dependent on the positioning of measurement

slice and how the ROI is drawn. In order for the volume fraction to be exactly known, a multi slice acquisition has to be performed and a 3D ROI has to be defined covering the whole compartment. However, ζ is assumed not to deviate too much from the accustomed value.

Simulations

The simulations showed that a simultaneous evaluation of $\Delta\chi$ and ζ only can be achieved under very restricted conditions. Not surprisingly, the parameter found to be most important for the possibility to separate the two parameters was image noise. The SNR required in order to keep the relative parameter error under 10 % is many times higher than normally achieved in a GESSE measurement. In a GESSE measurement with a clinically tolerable scan time (< 20 minutes) and a clinically relevant resolution ($2 \times 2 \times 6 \text{ mm}^3$) performed at $3T$, the SNR normally is on the order of $150 - 250$, dependent on the echo time used. For a SNR of 200, a relative error in $\Delta\chi$ of about 21 % would be expected. In order to increase SNR while keeping the resolution constant, the measurement time has to be extended. Since, the SNR is proportional to the square root of the number of measurements, increasing the SNR from 200 to 600 would require nine times the measurement time. Hence, 20 minutes measurement having a SNR of 200 would have to be extended to $3h$ to yield a SNR of 600. Such a measurement time is not applicable in the clinic, and still the relative error in $\Delta\chi$ would be about 10 %, which is higher than desirable. It should also be noticed, that this is valid for a simple two-compartment model. It will be even more difficult for a real *in vivo* application where other parameters influence the signal. In conclusion, it appears complex to accomplish a reliable estimation of $\Delta\chi$ under existing conditions, using this method. Going to higher field strengths could be a solution to the problem. At higher field strengths SNR is increased and the susceptibility effect is enlarged since $\delta\omega$ is direct proportional to the magnetic field strength. However, unwanted susceptibility effects also increase with the field strength, which may cause problems. But, as can be seen from Figure 4.10 – 4.13, if $\Delta\chi$ or ζ is previously known, the other parameter can be accurately estimated already at very low SNR. Hence, in order to realize this method in the clinic, a separate blood volume measurement is required. With a reliable blood volume measure, the simulations showed that a relative error in $\Delta\chi$ of approximately 3 % could be reached already at an SNR of 200.

The simulation of different GESSE sequence parameters showed that for a certain SNR, the relation between $\Delta\chi$ and ζ can be more accurately determined if a later gradient echo is used as a spin echo. This is in agreement with the results from the phantom measurements, where, when using the water diffusion model and a fixed ζ , better results were more frequently occurring when a later spin echo was used. Furthermore, the simulations showed that using a more frequent sampling does not notably improve the parameter estimations when $\Delta\chi$ and ζ is fitted simultaneously. This contradicts the prediction that a dense sampling of the short time area will contribute to a better separation of $\Delta\chi$ and ζ . The central parameter was rather shown to be the total sampling time. In order to achieve a more precise relation between $\Delta\chi$ and ζ , the sampling time should be chosen as large as possible, of course with consideration taken that enough signal remains at the last

echo. Choosing a large sampling window additionally improved the accuracy in the single parameters to some extent. The relaxation rate, R_2 , could be accurately estimated even at very low SNR and does not influence the outcome of the evaluation in case of static dephasing. In case of diffusion, however, R_2 plays a significant role. When R_2 is used as a fit parameter, the fits obtained using the static dephasing method coincide well with the measured data point even though the obtained $\Delta\chi$ not at all agrees with the authentic value. Hence, by adjusting R_2 , the static dephasing method can compensate for the diffusion effect in the measure data, but the result will be misleading. Therefore, an additional T2 measurement is recommended.

The practical influence of diffusion effects was investigated through simulations using parameters expected *in vivo*. It was found that by neglecting the effect of diffusion when predicting the MR signal-time course as expected in an *in vivo* measurement, the GESSE measurement with the shorter spin echo time overestimated $\Delta\chi$ with 12 % while the GESSE measurement with the longer spin echo time underestimated $\Delta\chi$ with 35 %. Hence, there could exist an optimal spin echo time where the obtained mean value agrees with the true mean value. This spin echo time, however, would depend on the radius and the apparent diffusion coefficient, and still the relative parameter error would be large when $\Delta\chi$ and ζ is fitted simultaneously. When ζ is fixed but R_2 is used as fit parameter, the obtained $\Delta\chi$ is approximately 15 % smaller than the true value for both GESSE sequences, R_2 is correspondingly increased to fit the static dephasing model to the non-static dephasing data.

Kiselev et al. [2005] estimated the vessel caliber in healthy human brain tissue to be in the range of 21–51 μm . This is slightly higher than expected from the known microvasculature anatomy. During the simulations, a vessel diameter of 50 μm was used. Hence, the effect of diffusion seen in the simulations is presumable even stronger *in vivo*. Consequently, modeling and consideration of diffusion effects are essential for an accurate estimation of the tissue oxygenation using the model presented in this work. However, considering the effect of diffusion requires prior knowledge of the vessel radius distribution within the voxel. The simulations performed here considered a uniform vessel size. Further studies are required where the influence of different radius distributions is examined. In addition, utilization of a more realistic tissue model naturally results in a larger amount of unknown parameters. Inclusion of intravascular signal, signal from ISF/CSF and diffusion gives a signal expression composed of three exponential functions with 11 free parameters. It is straightforward to conclude that it will be difficult to obtain stable results when fitting such an expression to a signal decay as the one shown in Figure 4.18 (d). Thus, for the method presented in this work to be a reliable oxygenation measurement method, several parameters have to be predetermined by independent measurements or some other means.

In vivo Measurements

The problem with verification of *in vivo* measurements is the absence of exact reference values. Instead presumed solutions have to be found in the literature. Although the reported values of venous oxygenation saturation are fairly consistent they are normally

found to be either in the range of 50 % or around 70 %. Moreover, even if a reference value for the venous oxygenation saturation could be established, it is not straightforward to estimate the expected value of $\Delta\chi$ *in vivo*. As mentioned briefly in section 2.3.4, there exist several values in the literature for the susceptibility difference between fully oxygenated and fully deoxygenated blood ($\Delta\chi_{ox}$). An early measurement was performed by Pauling and Coryell [1936], resulting in a value of $4\pi \cdot 0.27 \text{ ppm}$. Later measurement resulted in values of $4\pi \cdot 0.20 \text{ ppm}$ [Plyavin und Blum, 1983], $4\pi \cdot 0.18 \text{ ppm}$ [Weisskoff und Kiihne, 1992] and $4\pi \cdot 0.27 \text{ ppm}$ [Spees et al., 2001]. During previous attempts to quantify the BOLD effect, the value measured by Weisskoff und Kiihne [1992] has been frequently used [Haacke et al., 1997; Levin et al., 2001; An und Lin, 2002]. Later publications [He und Yablonskiy, 2007; He et al., 2008] argues strongly for the value measured by Spees et al. [2001]. However, the correct value is still unknown. A $\Delta\chi$ of 0.4 ppm would correspond to an oxygen saturation of 65 % if $\Delta\chi_{ox}$ is taken as $4\pi \cdot 0.27 \text{ ppm}$ but an oxygen saturation of 48 % with a $\Delta\chi_{ox}$ of $4\pi \cdot 0.18 \text{ ppm}$. If, however, $4\pi \cdot 0.18 \text{ ppm}$ would be confirmed as the true value of $\Delta\chi_{ox}$ and the oxygen saturation rather is 70 %, the $\Delta\chi$ would only be 0.23 ppm , and conversely, if $4\pi \cdot 0.27 \text{ ppm}$ is shown to be the correct $\Delta\chi_{ox}$ value but the oxygen saturation only is 50 %, $\Delta\chi$ would be 0.58 ppm . Thus, both the value of $\Delta\chi_{ox}$ and the venous oxygen saturation has to be verified before a statement of the method's reliability can be made.

The pixel-by-pixel evaluation shown in Figure 4.17 showed a great instability. This, however, was anticipated due to the low SNR of 100. The low SNR was required since the intention of the experiment was to demonstrate the effect seen during the simulations for low SNR. Increasing the SNR by choosing a shorter spin echo time can be easily done in case of patient measurements. However, a SNR higher than approximately 250 will be problematic to achieve in 20 minutes. Furthermore, increasing the SNR by choosing a larger number of averages will enlarge the risk of unwanted patient movements during the scan. Consequently, without using higher magnetic field strengths or unreasonable long measurement times it will be difficult to achieve a SNR much higher than 200 – 300. As shown in the simulations, the inherent instability of the method for simultaneous estimation of $\Delta\chi$ and ζ is extensive at such a low SNR. An independent measurement of the deoxygenated blood volume fraction is most certainly required.

Non-MR Techniques available to measure regional cerebral blood volume in humans include positron emission tomography (PET) and single photon emission computed tomography (SPECT) [Walovitch et al., 1990]. The disadvantage of those methods, except for the use of radioactive tracers, is that large effort has to be put into the realization of comparable positioning of the patients, and exact localization of the measurement volume in the two separate measurement systems. Available MR based methods to obtain cerebral blood volume includes contrast-enhanced bolus tracking techniques and contrast-enhanced steady-state techniques [Barbier et al., 2001]. The bolus tracking method is well suited to obtain fast, low-resolution information of the relative cerebral blood volume. However, in order to get a quantitative measure of the blood volume, the so-called arterial input function has to be accurately estimated. The arterial input function can be estimated by measuring signal changes around or inside a major blood vessel but several sources, including correcting for small vessel Hct and partial volume effects, make an accurate estimation difficult. In contrast to bolus tracking methods, steady state methods offer

a higher SNR [Tropres et al., 2001] which can be used to increase the resolution, but at the expense of longer acquisitions. Furthermore, the increase in the susceptibility difference between blood and tissue due to the injection of the contrast agent has to be known in order to estimate the absolute cerebral blood volume. Moreover, both techniques are invasive and they measure the whole blood volume. The blood volume needed for the evaluation of the measure data obtained using the GESSE sequence is the venous part, or rather the deoxygenated part, which then have to be estimated, a procedure that is likely to introduce further errors. Furthermore, in brain lesions (for example, in tumors), the blood-brain barrier can be disrupted, which allows for leakage of the contrast agent from the intravascular space into the extravascular space[Østergaard et al., 1996b,a]. This may preclude or introduce errors in the CBV mapping.

To facilitate a correction for diffusion effects *in vivo*, the vessel radius distribution in every measurement voxel has to be known. The relation of contrast-enhanced transverse relaxation rates $R2^*$ and $R2$ is a technique used for vivo mapping of the mean caliber of cerebral vessels [Kiselev et al., 2005]. This method, however, is normally used to track relative changes in vessel size rather than an absolute measure. Quantitative vessel size imaging must include measurements of the diffusion coefficient as well as an absolute determination of the regional cerebral blood volume.

VI

Conclusion and Outlook

THE OXYGEN SUPPLY of the brain is of great interest because it is directly related to the tissue viability. In particular, oxygenation is a central factor for the aggressiveness and metastasis tendency of cancer tumors. Additionally, hypoxia is a major obstacle to tumor therapy and associated with poor outcome for cancer patients. Unfortunately, the practical diagnostic possibilities for quantitative mapping of cerebral blood oxygenation are few.

An analytical model derived by Yablonskiy und Haacke [1994] describes the time course of magnetic resonance signal relaxation due to magnetic field inhomogeneity induced by a vascular network. Previous attempts to use this model to quantify tissue oxygenation using magnetic resonance imaging have been made without taking the effect of diffusion into account. The theoretical work of including the effect of diffusion into the model has been previously made by Kiselev und Posse [1999].

In this work, the influence of diffusion on the MR signal formation in the presence of a cylinder network was for the first time studied in phantom measurements. The task of verifying of the analytical model in presence of diffusion, included construction of measurement phantoms, which to the greatest extent possible were constructed to reflect the properties of the model. The phantoms were constructed using randomly coiled polyamide strings of different radius, immersed in a $NiSO_4$ solution. To validate the results obtained with the network phantoms, independent measurements of the susceptibility difference between the polyamide strings and the $NiSO_4$ solution were performed using single string phantoms. Moreover, since the method used in this work to measure tissue oxygenation, analyzes the signal relaxation caused by magnetic field inhomogeneities induced by the vascular network, any other source of inhomogeneities will be superimposed on the effect and, thus, spoil the estimation. A correction method based on acquisition and evaluation of high resolved 3D phase maps was optimized and tested in phantom measurements. It was shown that induced macroscopic field inhomogeneities can be successfully corrected for. The prediction of the MR signal as a function of cylinder radius and diffusion coefficient, as proposed by Kiselev und Posse [1999], was verified in network phantom measurements.

Furthermore, the practical influence of diffusion effects was investigated through simula-

tions using parameters expected *in vivo*. It was found that by neglecting the effect of diffusion when predicting the MR signal-time course expected in an *in vivo* measurement, errors of approximately 13 % would be introduced into the parameter estimation. The exact error, however, could potentially be much larger and is dependent on many factors including the sequence parameters used as well as the radius distribution. Nevertheless, considering the effect of diffusion requires prior knowledge of the vessel radius distribution within the voxel. Further studies are required where the influence of different radius distributions examined. The simulations also revealed that a simultaneous evaluation of $\Delta\chi$ and ζ only can be achieved under very restricted conditions. The possibility to separate the two parameters is exclusively determined by the image noise. In order to keep the relative parameter error under 10 % a SNR of 600 is required. However, if one of the parameters is previously known a SNR of 100 – 200 should be sufficient to accurately estimate the other parameter.

The initial *in vivo* measurements confirmed the results obtained from the simulations. By using known literature values for the blood volume fraction in the brain, oxygenation levels that are in agreement with previous studies could be achieved. Furthermore, the sensitivity to caffeine induced oxygenation changes is encouraging for further studies. However, quantitative blood volume measurements and correction for diffusion effects have to be performed in order to verify the practical use of the method *in vivo*. Nevertheless, if this could be successfully accomplished, the theoretical cylinder network model will become a tool for MR-based *in vivo* quantification of tissue oxygenation and will potentially replace the invasive ^{15}O PET technique used today.

Bibliography

- Abdul-Rahman, H. S., Gdeisat, M. A., Burton, D. R., Lalor, M. J., Lilley, F. und Moore, C. J.: Fast and robust three-dimensional best path phase unwrapping algorithm. *Appl Opt*, 46: 6623–6635, 2007.
- Abragam, A.: *Principles of Nuclear Magnetism*. Oxford University Press, London, 1994.
- An, H. und Lin, W.: Quantitative measurements of cerebral blood oxygen saturation using magnetic resonance imaging. *J Cereb Blood Flow Metab*, 20: 1225–1236, 2000.
- An, H. und Lin, W.: Cerebral oxygen extraction fraction and cerebral venous blood volume measurements using MRI: effects of magnetic field variation. *Magn Reson Med*, 47: 958–66, 2002.
- An, H., Lin, W., Celik, A. und Lee, Y. Z.: Quantitative measurements of cerebral metabolic rate of oxygen utilization using MRI: a volunteer study. *NMR Biomed*, 14: 441–447, 2001.
- Barbier, E. L., Lamalle, L. und Decorps, M.: Methodology of brain perfusion imaging. *J Magn Reson Imaging*, 13(4): 496–520, 2001.
- Bloch, F.: Nuclear induction. *Phys. Rev.*, 70(7-8): 460–474, 1946.
- Bongers, A.: *Ortsaufgelöste Messung der Gewebe-Sauerstoffversorgung mittels BOLD-sensitiver MR-Bildgebung*. Dissertation, Ruprecht - Karls - Universität Heidelberg, 2004.
- Bonny, J. M., Laurent, W. und Renou, J. P.: Detection of susceptibility effects using simultaneous T2* and magnetic field mapping. *Magn Reson Imaging*, 18: 1125–1128, 2000.
- Boxerman, J. L., Hamberg, L. M., Rosen, B. R. und Weisskoff, R. M.: MR contrast due to intravascular magnetic susceptibility perturbations. *Magn Reson Med*, 34(4): 555–566, 1995.
- Brown, J. M. und Giaccia, A. J.: The unique physiology of solid tumors: opportunities (and problems) for cancer therapy. *Cancer Res*, 58: 1408–1416, 1998.
- Brown, R. J. S.: Distribution of fields from randomly placed dipoles: Free precession signal decay as result of magnetic grains. *Phys Rev*, 121(5): 1379–1383, 1961.

- Brown, T. R., Kincaid, B. M. und Ugurbil, K.: NMR chemical shift imaging in three dimensions. *Proc Natl Acad Sci U S A*, 79(11): 3523–3526, 1982.
- Cameron, O. G., Modell, J. G. und Hariharan, M.: Caffeine and human cerebral blood flow: A positron emission tomography study. *Life Sciences*, 47(13): 1141–1146, 1990.
- Carr, H. Y. und Purcell, E. M.: Effects of diffusion on free precession in nuclear magnetic resonance experiments. *Phys Rev*, 94: 630–638, 1954.
- Duvernoy, H.M., Delon, S. und Vannson, J.L.: Cortical blood vessels of the human brain. *Brain Res Bull*, 7: 519–579, 1981.
- Field, A. S., Laurienti, P. J., Yen, Y.-F., Burdette, J. H. und Moody, D. M.: Dietary caffeine consumption and withdrawal: Confounding variables in quantitative cerebral perfusion studies? *Radiology*, 227(1): 129–135, 2003.
- Folland, G. B.: *Fourier Analysis and its Applications*. Brooks/Cole Publishing Company, 1992.
- Fujita, N., Shinohara, M., Tanaka, H., Yutani, K., Nakamura, H. und Murase, K.: Quantitative mapping of cerebral deoxyhemoglobin content using MR imaging. *Neuroimage*, 20: 2071–2083, 2003.
- Gati, J. S., Menon, R. S., Ugurbil, K. und Rutt, B. K.: Experimental determination of the BOLD field strength dependence in vessels and tissue. *Magn Reson Med*, 38: 296–302, 1997.
- Golay, X., Silvennoinen, M. J., Zhou, J., Clingman, C. S., Kauppinen, R. A., Pekar, J. J. und van Zijl, P. C. M.: Measurement of tissue oxygen extraction ratios from venous blood T2: Increased precision and validation of principle. *Magn Reson Med*, 46: 282–291, 2001.
- Gudbjartsson, H. und Patz, S.: The Rician distribution of noisy MRI data. *Magn Reson Med*, 34: 910–914, 1995.
- Haacke, E. M., Brown, R. W., Thompson, M. R. und Venkatesan, R.: *Magnetic Resonance Imaging. Physical Principles and Sequence Design*. Wiley, New York, 1999.
- Haacke, E. M., Xu, Y., Cheng, Y. C. und Reichenbach, J. R.: Susceptibility weighted imaging (swi). *Magn Reson Med*, 52(3): 612–618, 2004.
- Haacke, E.M., Lai, S., Reichenbach, J.R., Kuppusamy, K., Hoogenraad, F.G.C., Takeichi, H. und Lin, W.: In vivo measurement of blood oxygen saturation using magnetic resonance imaging: A direct validation of the blood oxygen level-dependent concept in functional brain imaging. *Human Brain Mapping*, 5: 341–346, 1997.
- Hahn, E. L.: Spin echoes. *Phys Rev*, 80(4): 580–594, 1950.
- He, X. und Yablonskiy, D. A.: Quantitative BOLD: mapping of human cerebral deoxygenated blood volume and oxygen extraction fraction: default state. *Magn Reson Med*, 57: 115–126, 2007.

- He, X., Zhu, M. und Yablonskiy, D. A.: Validation of oxygen extraction fraction measurement by qBOLD technique. *Magn Reson Med*, 60: 882–888, 2008.
- Hirsch, J. G., Bock, M., Essig, M. und Schad, L. R.: Comparison of diffusion anisotropy measurements in combination with the FLAIR-Technique. *Magn Reson Imaging*, 17: 705—716, 1999.
- Hoogenraad, F.G., Reichenbach, J.R., Haacke, E.M., Lai, S., Kuppusamy, K. und Sprenger, M.: In vivo measurement of changes in venous blood-oxygenation with high resolution functional MRI at 0.95 Tesla by measuring changes in susceptibility and velocity. *Magn Reson Med*, 97–107, 1998.
- Irrazabal, P., Meyer, C. H., Nishimura, D. G. und Macovski, A.: Inhomogeneity correction using an estimated linear field map. *Magn Reson Med*, 35: 278–282, 1996.
- Ito, H., Kanno, I., Kato, C., Sasaki, T., Ishii, K., Ouchi, Y., Iida, A., Okazawa, H., Hayashida, K., Tsuyuguchi, N., Ishii, K., Kuwabara, Y., und Senda, M.: Database of normal human cerebral blood flow, cerebral blood volume, cerebral oxygen extraction fraction and cerebral metabolic rate of oxygen measured by positron emission tomography with ^{15}O -labelled carbon dioxide or water, carbon monoxide and oxygen: a multicentre study in japan. *Eur J Nucl Med Mol Imaging*, 31: 635—643, 2004.
- Jezzard, P. und Balaban, R. S.: Correction for geometric distortion in echo planar images from B_0 field variations. *Magn Reson Med*, 34: 65–73, 1995.
- Kiselev, V. G., Strecker, R., Ziyeh, S., Speck, O. und Hennig, J.: Vessel size imaging in humans. *Magn Reson Med*, 53(3): 553–563, 2005.
- Kiselev, V.G. und Posse, S.: Analytical model of susceptibility-induced MR signal dephasing: Effect of diffusion in a microvascular network. *Magn Reson Med*, 41: 499—509, 1999.
- Lauterbur, P. C.: Image formation by induced local interactions: Examples employing nuclear magnetic resonance. *Nature*, 242(5394): 190–191, 1973.
- Le Bihan, D., Turner, R. und Patronas, N.: *Diffusion and Perfusion Magnetic Resonance Imaging*. Raven Press, New York, 1995.
- Levin, J. M., de B. Frederick, B., Ross, M. H., Fox, J. F., von Rosenberg, H. L., Kaufman, M. J., Lange, N., Mendelson, J. H., Cohen, B. M. und Renshaw, P. F.: Influence of baseline hematocrit and hemodilution on BOLD fMRI activation. *Magn Reson Imaging*, 19: 1055–1062, 2001.
- Ljunggren, S.: A simple graphical representation of fourier-based imaging methods. *J Magn Reson*, 54: 338–343, 1983.
- Ma, J. und Wehrli, F. W.: Method for image-based measurement of the reversible and irreversible contribution to the transverse-relaxation rate. *J Magn Reson*, Series B 111: 61–69, 1996.

- Malonek, D., Dirnagl, U., Lindauer, U., Yamada, K., Kanno, I. und Grinvald, A.: Vascular imprints of neuronal activity: relationships between the dynamics of cortical blood flow, oxygenation, and volume changes following sensory stimulation. *Proc Natl Acad Sci U S A*, 94: 14826–14831, 1997.
- Mansfield, P.: Multi-planar image formation using NMR spin echoes. *J Phys Chem: Solid State Physics*, 10: L55–L58, 1977.
- Meiboom, S. und Gill, D.: Modified spin-echo method for measuring nuclear relaxation times. *Rev Sci Instrum*, 29: 688–691, 1958.
- Molls, M., Stadler, P., Becker, A., Feldmann, H.J. und Dunst, J.: Relevance of oxygen in radiation oncology. mechanisms of action, correlation to low hemoglobin levels. *Strahlenther Onkol*, 4: 13–16, 1998.
- Moskalenko, Y. E.: *Biophysical aspects of cerebral circulation*. Pergamon Press, Oxford, 1980.
- Ogawa, S., Lee, T.M. und Barrere, B.: The sensitivity of magnetic resonance imaging signals of a rat brain to changes in the cerebral venous blood oxygenation. *Magn Reson Med*, 29(2): 205–210, 1993.
- Østergaard, L., Sorensen, A. G., Kwong, K. K., Weisskoff, R. M., Gyldensted, C. und Rosen, B. R.: High resolution measurement of cerebral blood flow using intravascular tracer bolus passages. part II: Experimental comparison and preliminary results. *Magn Reson Med*, 36(5): 726–736, 1996a.
- Østergaard, L., Weisskoff, R. M., Chesler, D. A., Gyldensted, C. und Rosen, B. R.: High resolution measurement of cerebral blood flow using intravascular tracer bolus passages. part I: Mathematical approach and statistical analysis. *Magn Reson Med*, 36(5): 715–725, 1996b.
- Pauling, L. und Coryell, C. D.: The magnetic properties and structure of hemoglobin, oxyhemoglobin and carbonmonoxyhemoglobin. *Proc Natl Acad Sci U S A*, 22: 210–216, 1936.
- Plyavin, Y. A. und Blum, E. Y.: Magnetic parameters of blood cells and high gradient paramagnetic and diamagnetic phoresis. *Magnetohydrodynamics*, 19: 349—359, 1983.
- Price, W. S., Ide, H. und Arata, Y.: Self-diffusion of supercooled water to 238K using PGSE NMR diffusion measurements. *J Phys Chem A*, 103(4): 448—450, 1999.
- Purcell, E. M., Torrey, H. C. und Pound, R. V.: Resonance absorption by nuclear magnetic moments in a solid. *Phys. Rev.*, 69(1-2): 37–38, 1946.
- Reichenbach, J. R., Venkatesan, R., Schillinger, D. J., Kido, D. K. und Haacke, E. M.: Small vessels in the human brain: Mr venography with deoxyhemoglobin as an intrinsic contrast agent. *Radiology*, 204(1): 272–277, 1997.
- Rákoš, M., Šimo, R. und Varga, Z.: Magnetic study of elongated polyamide fibres. *Czechoslovak Journal of Physics*, 16: 167–169, 1966.

- Schenk, J. F.: The role of magnetic susceptibility in magnetic resonance imaging: MRI magnetic compability of the first and second kinds. *Med Phys*, 23(6): 815–850, 1996.
- Schmidt, R.F. und Thews, G.: *Physiologie des Menschen, Heidelberg*. Springer, 1995.
- Schmitt, F., Stehling, M.K. und Turner, R.: *Echo-Planar Imaging*. Springer, Heidelberg, 1998.
- Schröder, H.: *Optimierung und Verifizierung BOLD-sensitiver MR-Bildgebungsmethoden zur Bestimmung der Gewebeoxygenierung*. Diplomarbeit, Ruprecht - Karls - Universität Heidelberg, 2005.
- Sedlacik, J.: *New Advances in Susceptibility Weighted MRI to Determine Physiological Parameters*. Dissertation, Technischen Universität Ilmenau, 2007.
- Sedlacik, J., Rauscher, A. und Reichenbach, J. R.: Obtaining blood oxygenation levels from MR signal behavior in the presence of single venous vessels. *Magn Reson Med*, 58(5): 1035–1044, 2007.
- Sedlacik, J., Rauscher, A. und Reichenbach, J. R.: Quantification of modulated blood oxygenation levels in single cerebral veins by investigating their mr signal decay. *Zeitschrift für Medizinische Physik*, doi:10.1016/j.zemedi.2008.07.005, In Press, Corrected Proof.
- Shannon, C. E.: Communication in the presence of noise. *Proc Institute of Radio Engineers*, 37(1): 10–21, 1949.
- Slichter, C. P.: *Principles of Magnetic Resonance*. Springer, Heidelberg, 1992.
- Spees, W.M., Yablonsiy, D.A., Oswood, M.C. und Ackerman, J.J.H.: Water proton MR properties of human blood at 1.5 Tesla : Magnetic susceptibility T1, T2, T2* and non lorentzian signal behavior. *Magn Reson Med*, 45(4): 533–542, 2001.
- Stryer, L.: *Biochemie*. Spektrum Akad. Verlag, Heidelberg, 1998.
- Sukstanskii, A. L. und Yablonskiy, D. A.: Theory of FID NMR signal dephasing induced by mesoscopic magnetic field inhomogeneities in biological systems. *J Magn Reson*, 151(1): 107–117, 2001.
- Tropres, I., Grimault, S., Vaeth, A., Grillon, E., Julien, C., Payen, J. F., Lamalle, L. und Decorps, M.: Vessel size imaging. *Magn Reson Med*, 45(3): 397–408, 2001.
- Twieg, D. B.: The k-trajectory formulation of the NMR imaging process with applications in analysis and synthesis of imaging methods. *Med Phys*, 10(5): 610–621, 1983.
- Vlaardingerbroek, M. T. und den Boer, J. A.: *Magnetic Resonance Imaging; Theory and Practice*. Springer, 2003.
- Walovitch, R. C., Williams, S. J. und Lafrance, N. D.: Radiolabeled agents for SPECT imaging of brain perfusion. *Int J Rad Appl Instrum B*, 17(1): 77–83, 1990.

- Weisskoff, R. M. und Kiihne, S.: MRI susceptometry: image-based measurement of absolute susceptibility of MR contrast agents and human blood. *Magn Reson Med*, 24(2): 375–383, 1992.
- Yablonskiy, D. A.: Quantitation of intrinsic magnetic susceptibility-related effects in a tissue matrix. phantom study. *Magn Reson Med*, 39(3): 417–428, 1998.
- Yablonskiy, D. A. und Haacke, E. M.: Theory of NMR signal behavior in magnetically inhomogeneous tissues: the static dephasing regime. *Magn Reson Med*, 32(6): 749–63, 1994.
- Yablonskiy, D. A. und Haacke, E. M.: An MRI method for measuring T2 in the presence of static and Rf magnetic field inhomogeneities. *Magn Reson Med*, 37(6): 872–876, 1997.
- Yamaguchi, T., Kanno, I., Uemura, K., Shishido, F., Inugami, A., Ogawa, T., Murakami, M. und Suzuki, K.: Reduction in regional cerebral metabolic rate of oxygen during human aging. *Stroke*, 17(6): 1220–1228, 1986.

List of Tables

2.1	List of selected nuclei with their spins and associated magnetic moments . .	4
3.1	Single string phantom specifications	36
3.2	String network phantom specifications	37
3.3	GESSE sequence parameters for phantom measurements	37
3.4	Measurements Parameters for GESSE scan	38
3.5	Mole mass and density of some substances	38
3.6	Susceptibility of $NiSO_4$ solutions	39
4.1	Result of single string measurements	48
4.2	Result from network phantom	54
4.3	Result from network phantom using fix ζ	58
4.4	Result from network phantom	60
4.5	Result from network phantom using fix ζ	60

List of Figures

2.1	Zeemann splitting	5
2.2	Motion of the magnetization vector in the laboratory and rotating coordinate system	6
2.3	Spin-Lattice Relaxation	8
2.4	Spin-Spin relaxation	9
2.5	Spin Echo formation	12
2.6	Slice selection	14
2.7	Frequency encoding	15
2.8	Schematic view of the concept of k-space	17
2.9	Spin Echo sequence	19
2.10	Gradient Echo sequence	20
2.11	Overview of the cortical blood vessels	21
2.12	Oxygen saturation curve of hemoglobin	22
3.1	Single cylinder in an external magnetic field	26
3.2	Simulated field distribution and voxel shapes	27
3.3	Signal time course in a microvascular network with a refocusing pulse and consideration of diffusion	32
3.4	GESSE Sequence	34
3.5	Single String Phantom	35
3.6	String network phantom	36
4.1	Macroscopic inhomogeneity correction	47
4.2	Results of macroscopic inhomogeneity correction II	47

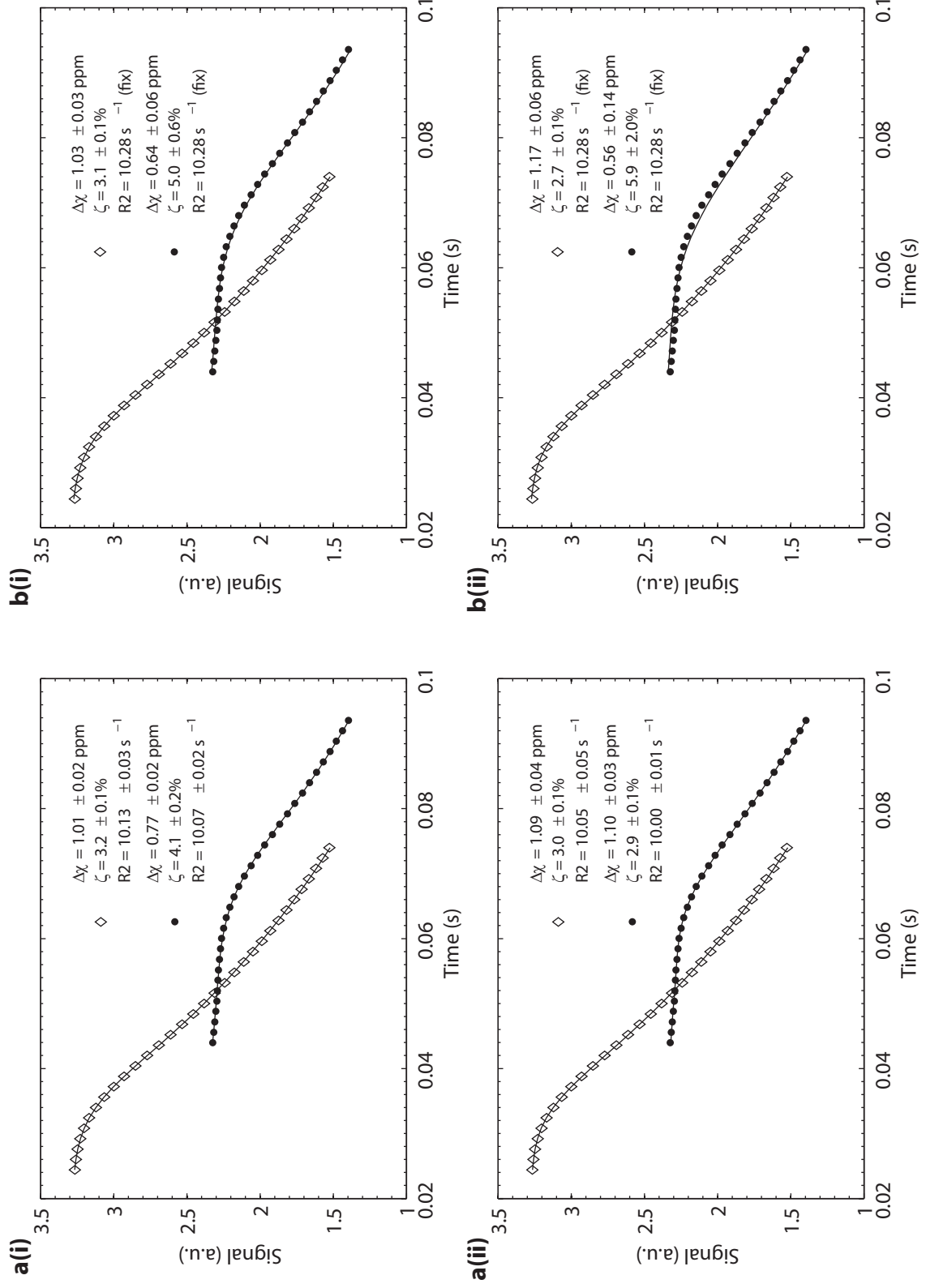
4.3	Signal from single string measurements	48
4.4	Calibration curve of $\Delta\chi$ and R2	49
4.5	Comparison of evaluation methods	50
4.6	Images and measured signal from the $89\mu m$ network phantom	53
4.7	RMSE plots for the $245\mu m$ network phantom using a short echo time	56
4.8	RMSE plots for the $27\mu m$ network phantom using a long echo time	57
4.9	Surface plots of RMSE	61
4.10	Effect on parameter estimation of changing the position of the spin echo	65
4.11	Effect on parameter estimation of changing the distance between two adjacent echoes	66
4.12	Effect on parameter estimation of changing the total number of echoes	67
4.13	Effect on parameter estimation of changing the SNR	68
4.14	Relative parameter error as a function of SNR	69
4.15	Relative parameter error as a function of SNR when ζ is fixed	69
4.16	evaluation of simulated <i>in vivo</i> data	72
4.17	Quantitative maps of ζ , $\Delta\chi$ and R2 <i>in vivo</i>	73
4.18	Evaluation of $\Delta\chi$ <i>in vivo</i>	74
4.19	Modification of the venous oxygenation saturation using caffeine	76

Appendices

Appendix A

Capillary Network Phantom Measurements

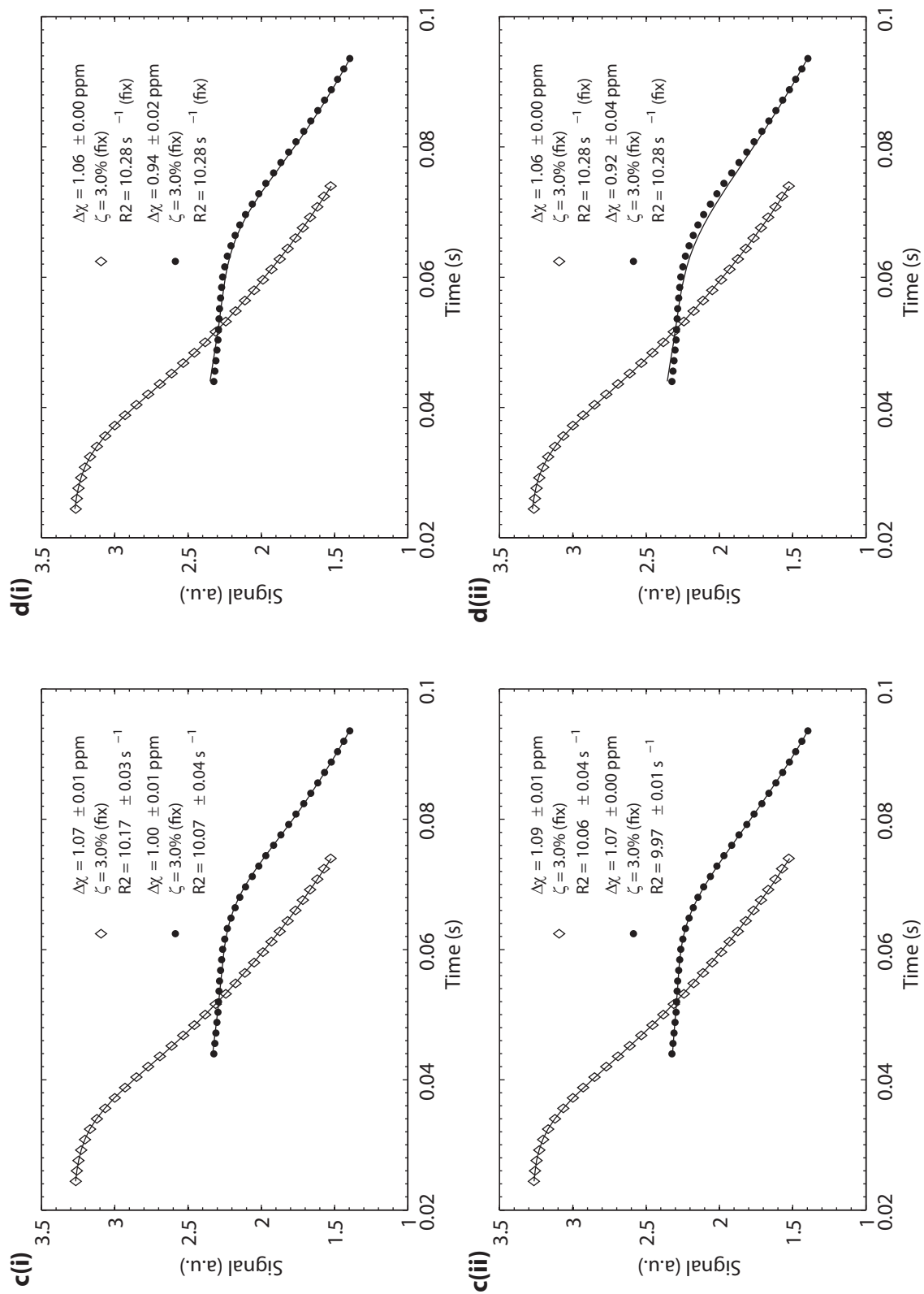
ON THE FOLLOWING pages, the signal time course measured in a ROI in the network phantoms is shown together with the parameters obtained at evaluation. The magnetic field strength and the specific phantom used are given below the figures on respective page. Evaluations performed using three ($\Delta\chi$, ζ and $R2$) fit parameters are labeled with **(a)**. Evaluations with two fit parameters are marked with **(b)** ($\Delta\chi$ and ζ) or **(c)** ($\Delta\chi$ and $R2$). Evaluations made using one ($\Delta\chi$) fit parameter are indicated with **(d)**. Diagrams marked with **(i)** correspond to curves and parameters obtained at evaluation using the static dephasing model. Diagrams marked with **(ii)** correspond to curves and parameters obtained when the water diffusion model was used for evaluation. For all measurement points, the error bars are equal or smaller than the symbol sizes.



245μm phantom at 3T

a) 3 parameter fit, without diffusion (i) and with diffusion (ii)

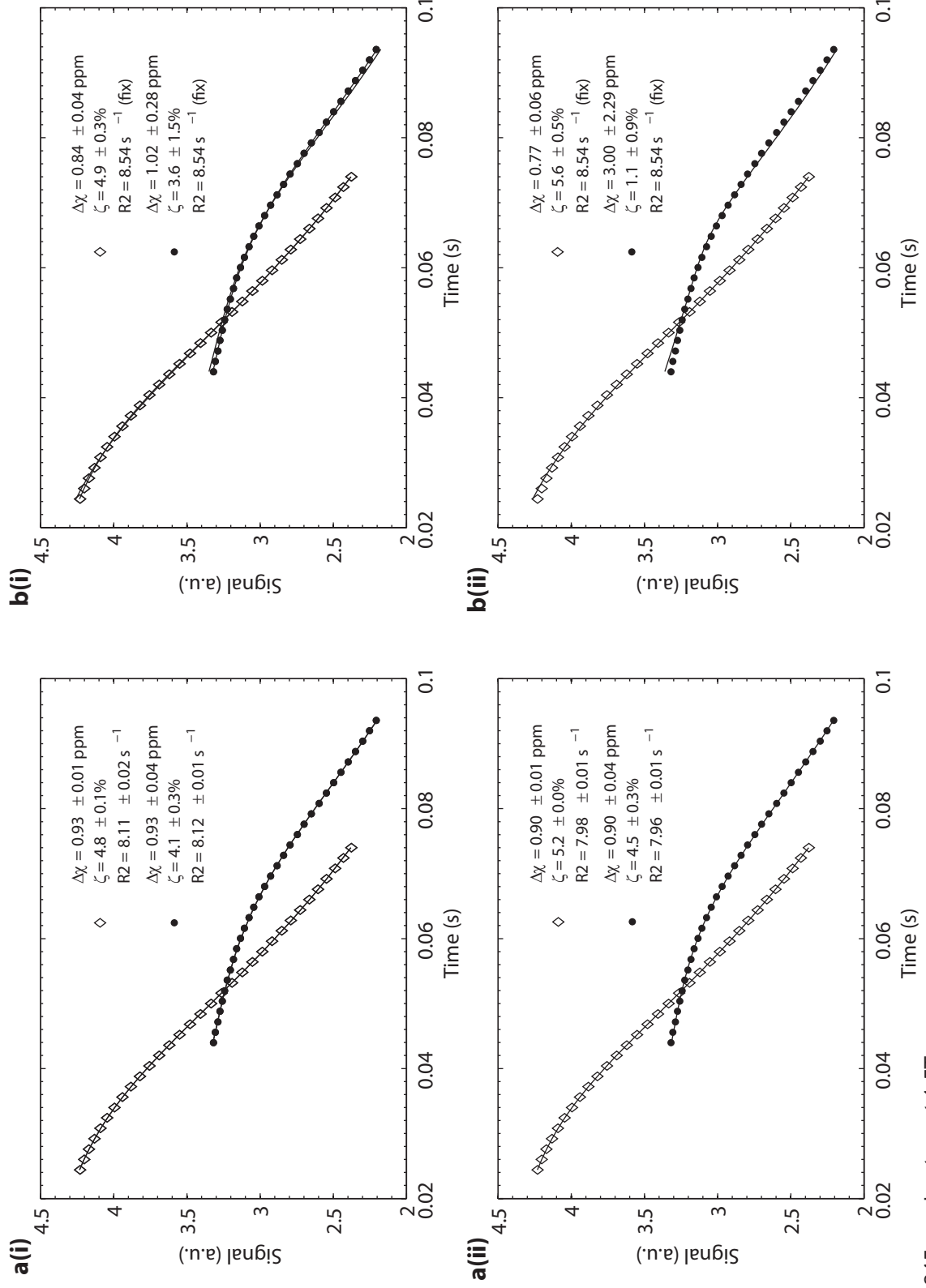
b) 2 parameter fit (fix R2), without diffusion (i) and with diffusion (ii)

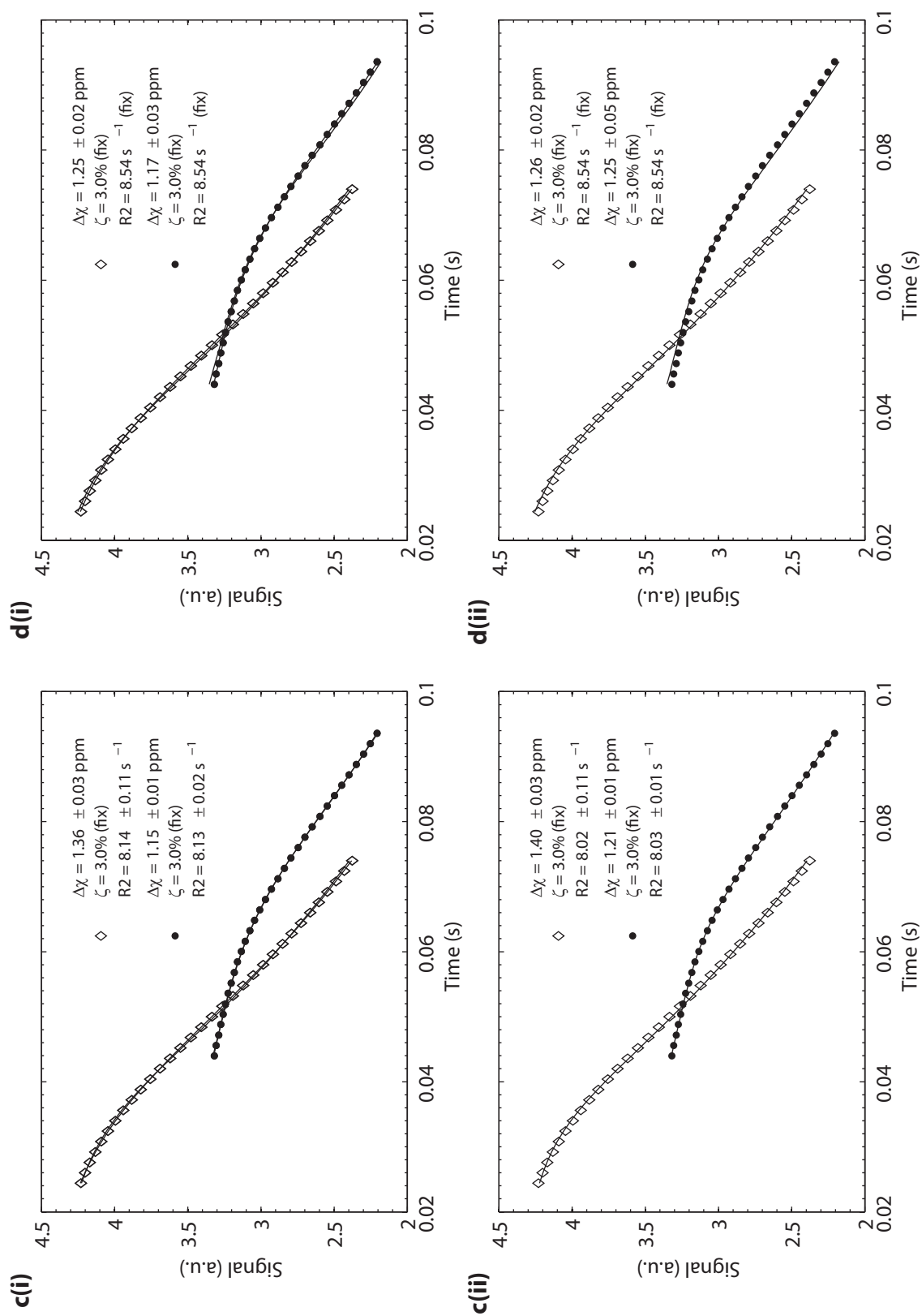


245μm phantom at 3T

c) 2 parameter fit (fix $\Delta\chi$), without diffusion (i) and with diffusion (ii)

d) 1 parameter fit (fix $R2$ and ζ), without diffusion (i) and with diffusion (ii)

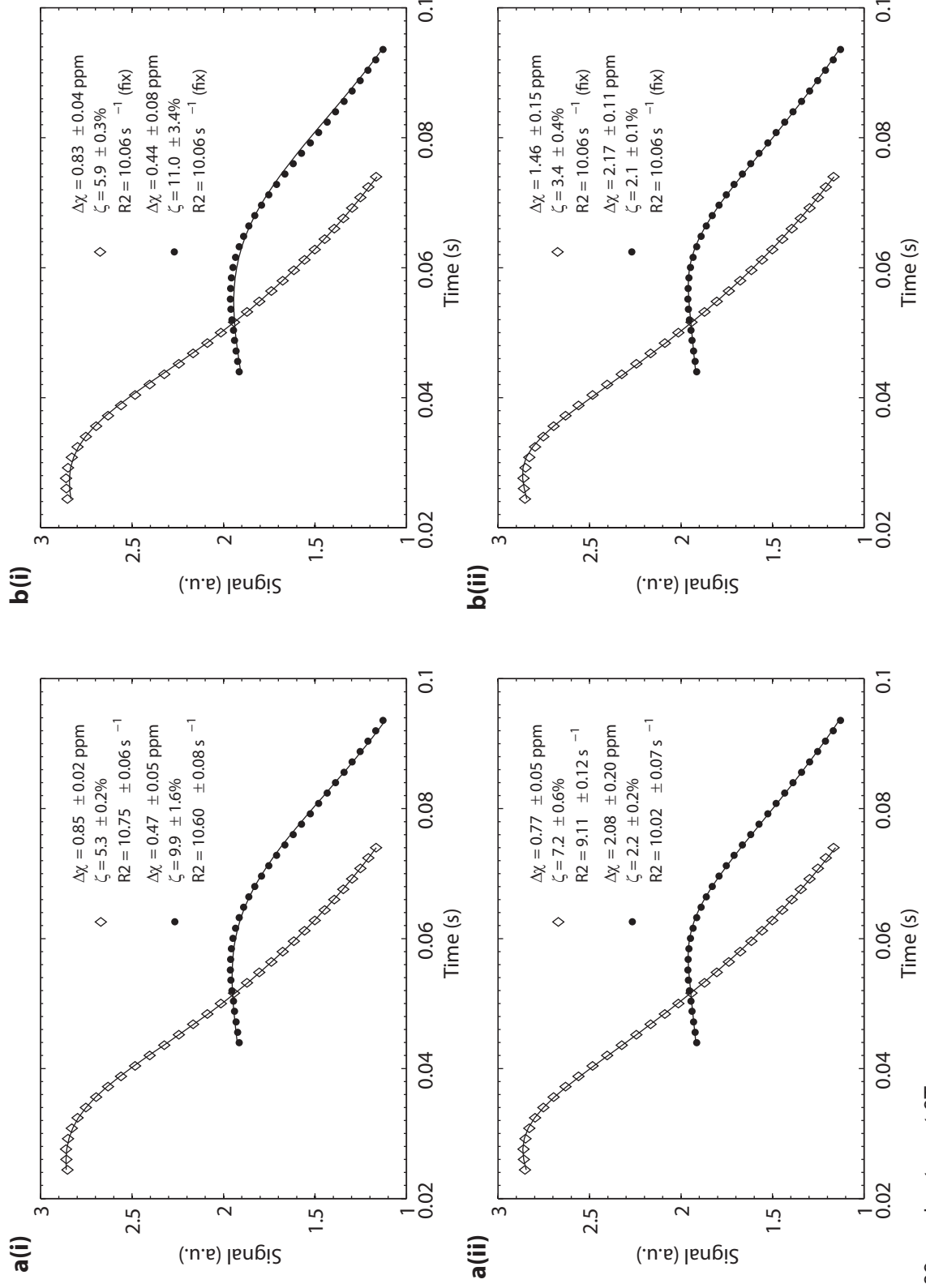


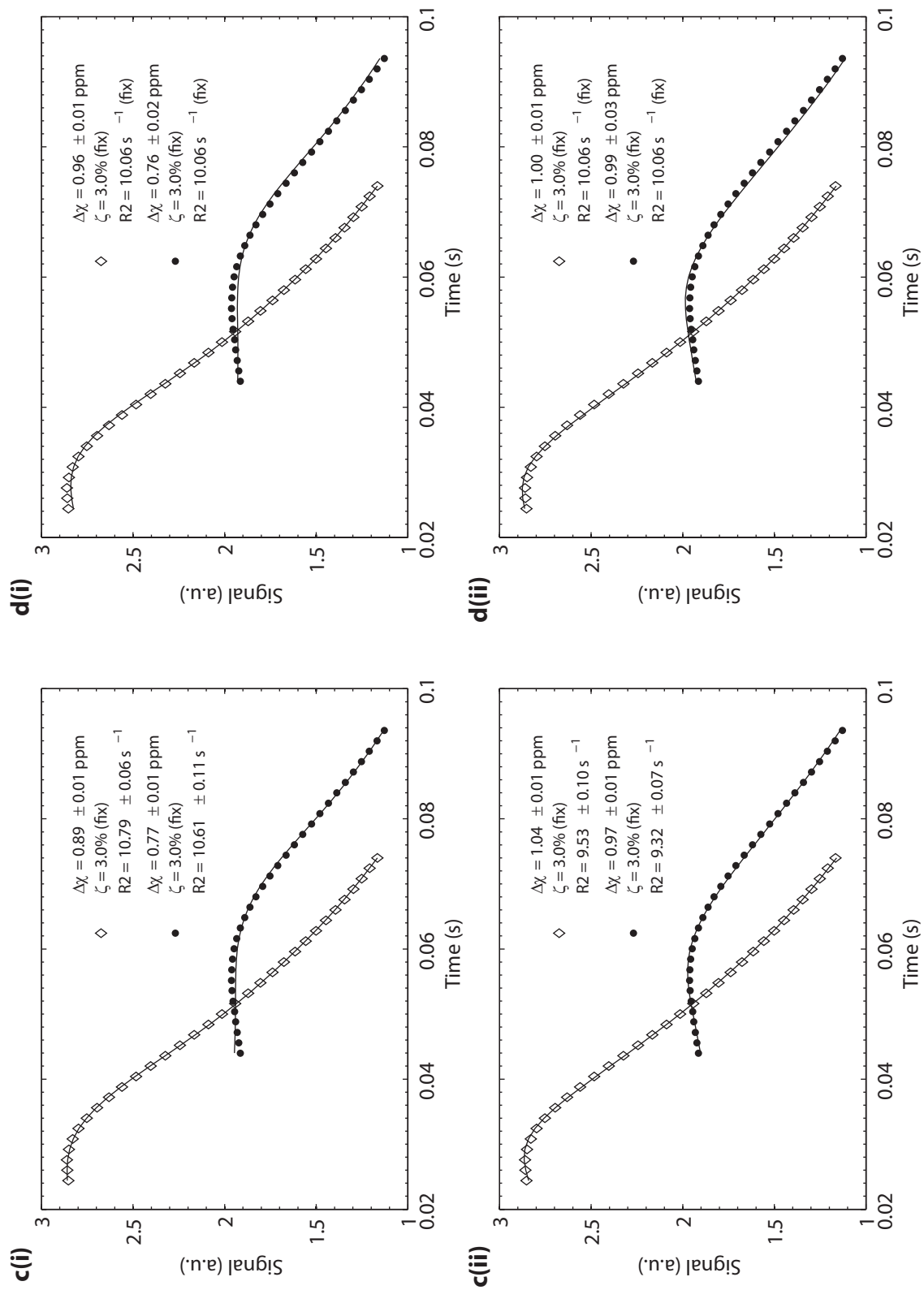


245μm phantom at 1.5T

c) 2 parameter fit (fix ζ), without diffusion (i) and with diffusion (ii)

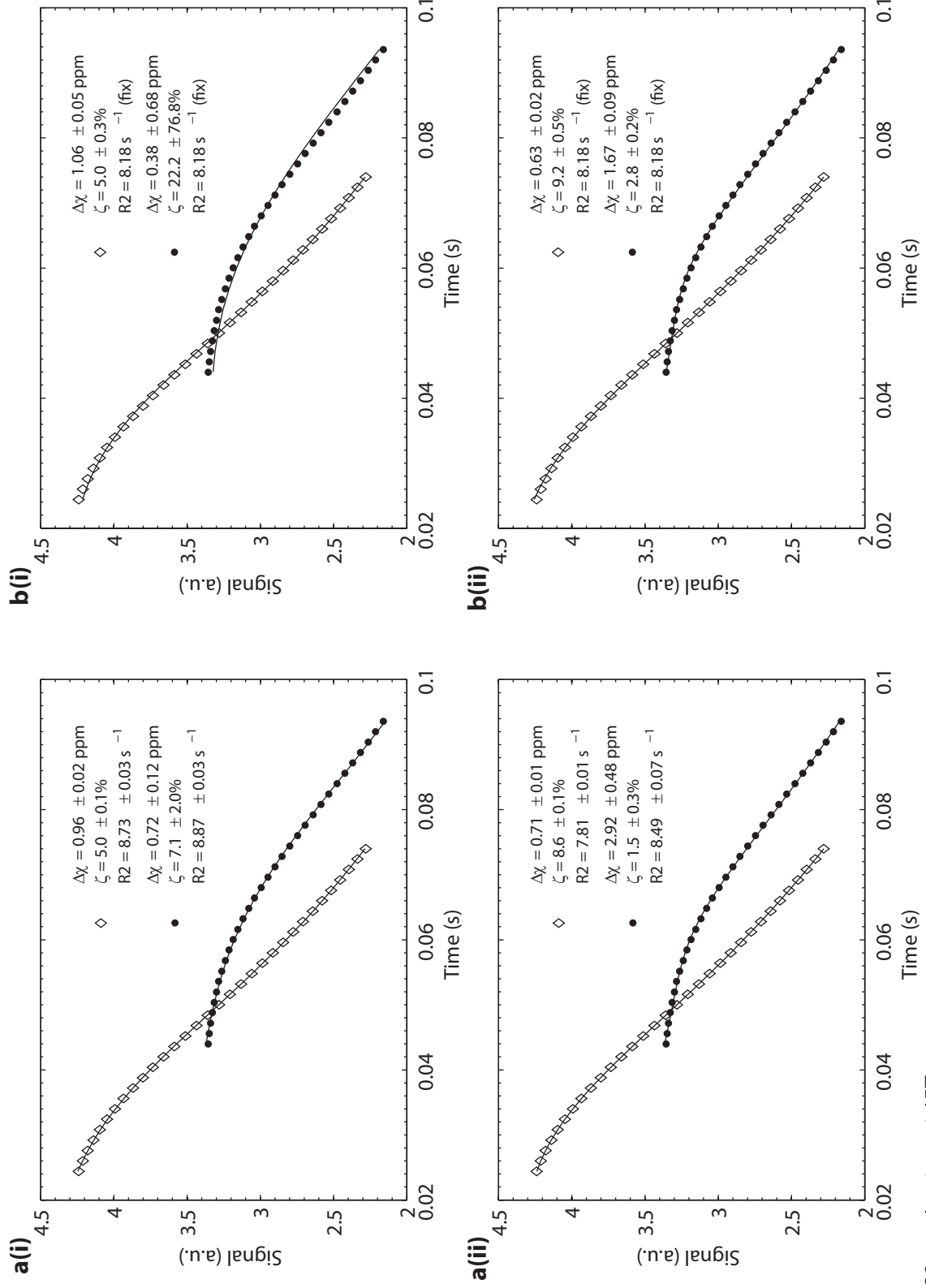
d) 1 parameter fit (fix $R2$ and ζ), without diffusion (i) and with diffusion (ii)

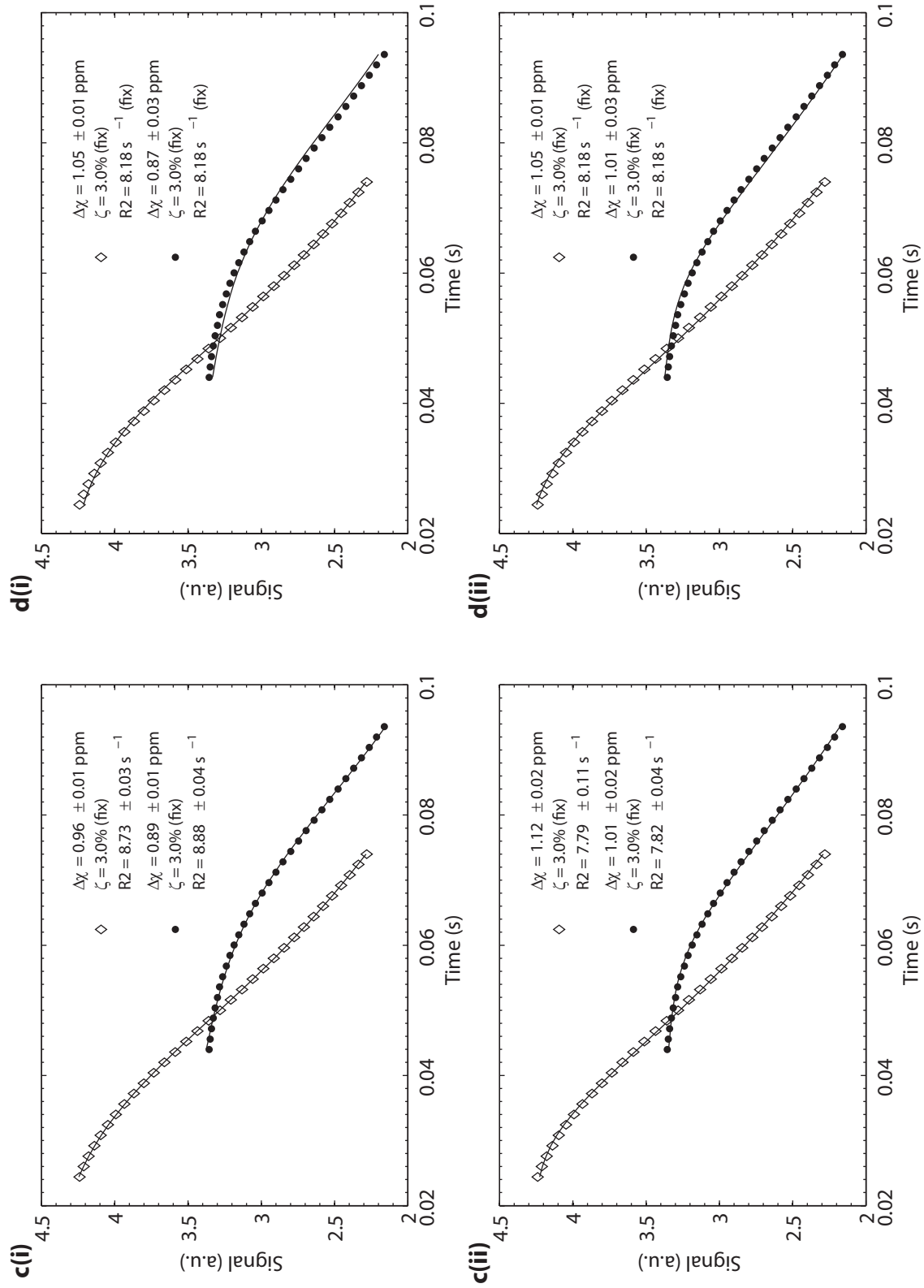




89μm phantom at 3T

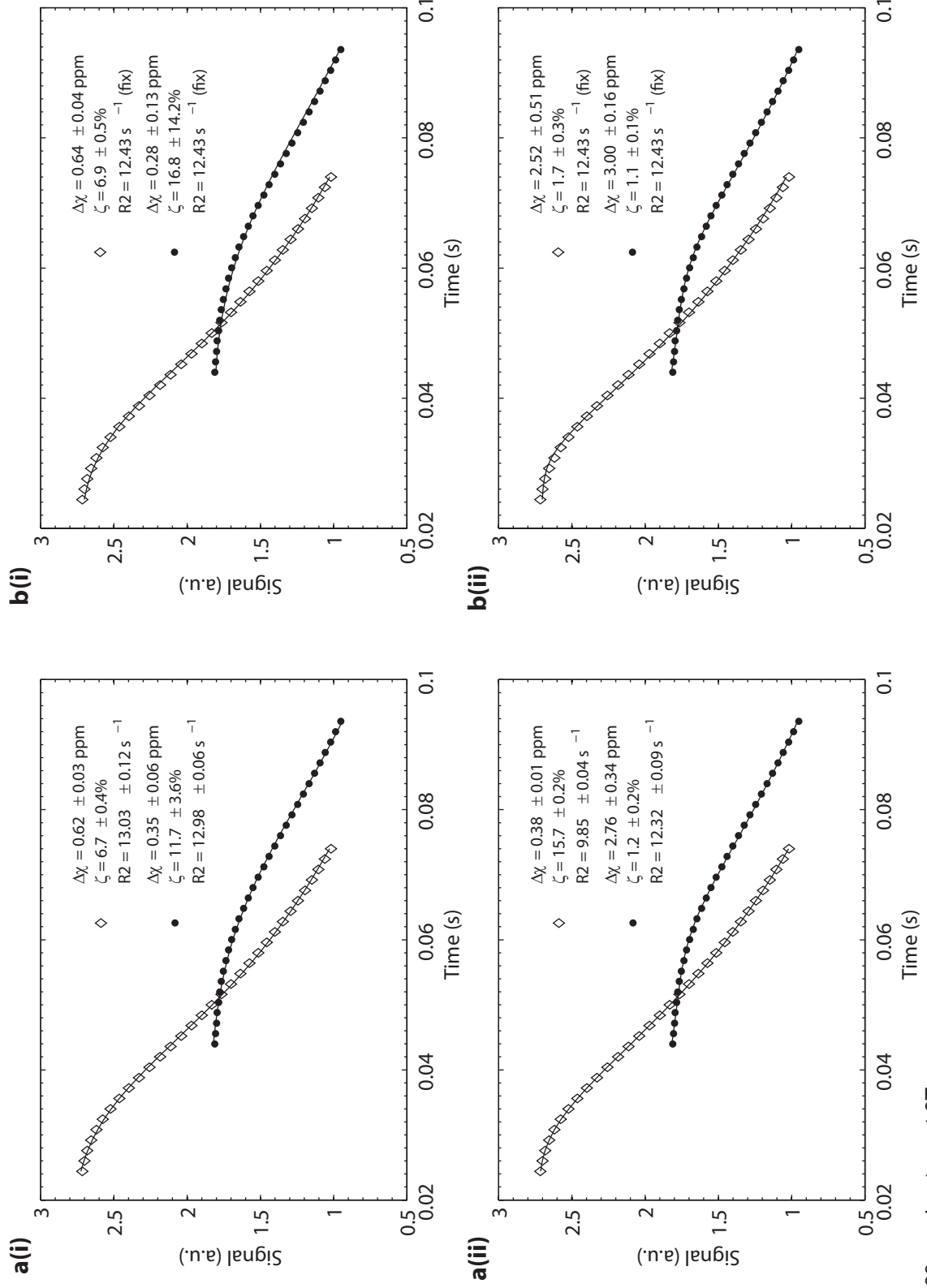
c) 2 parameter fit (fix ζ), without diffusion (i) and with diffusion (ii)d) 1 parameter fit (fix R2 and ζ), without diffusion (i) and with diffusion (ii)





89μm phantom at 1.5T

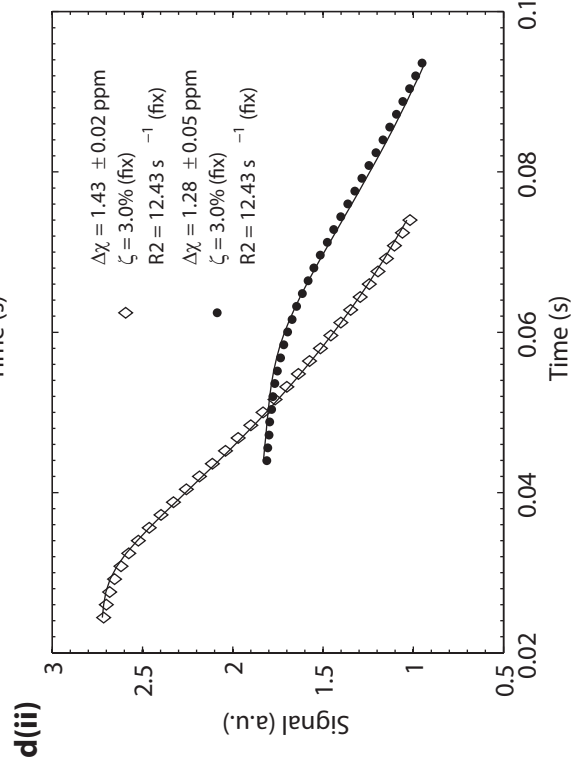
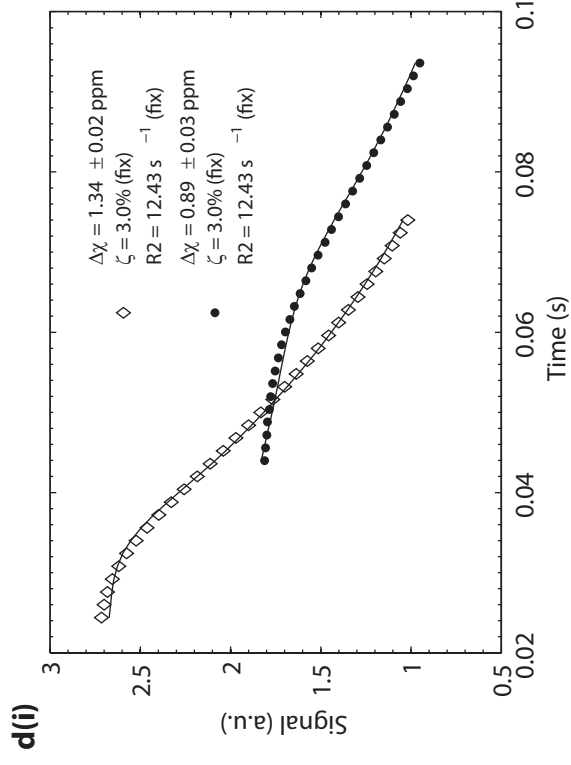
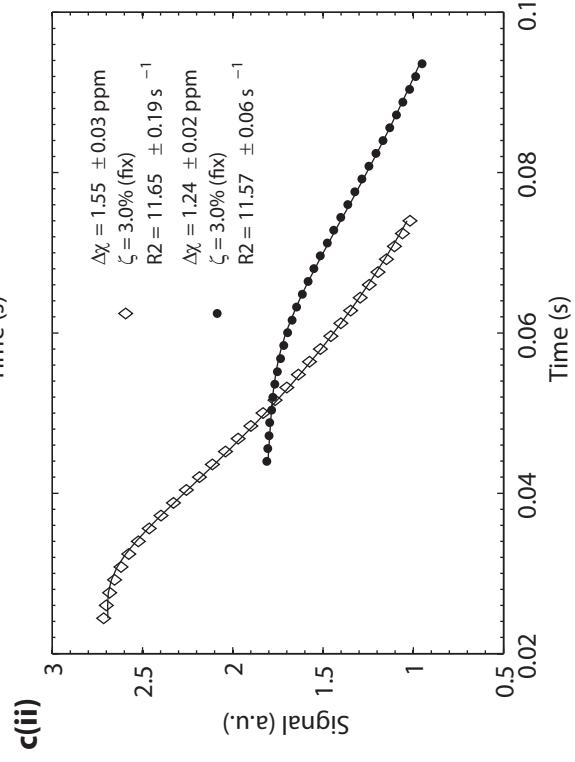
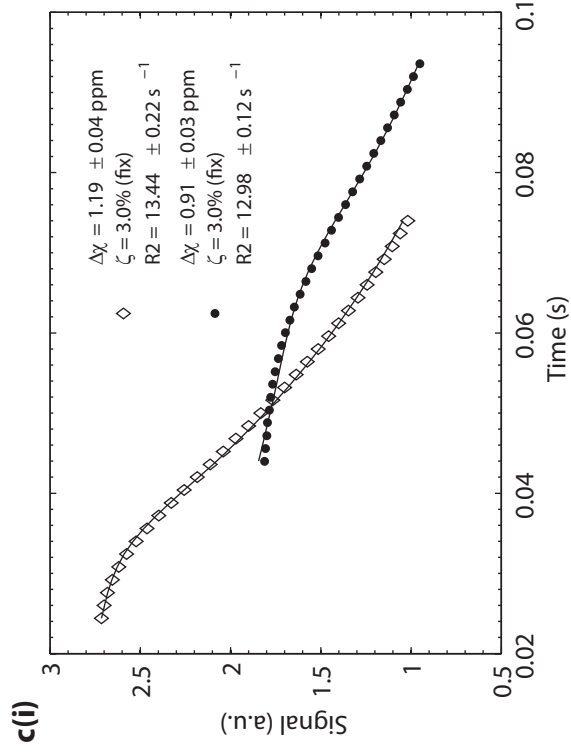
c) 2 parameter fit (fix $\Delta\chi$), without diffusion (i) and with diffusion (ii)d) 1 parameter fit (fix $R2$ and ζ), without diffusion (i) and with diffusion (ii)



63μm phantom at 3T

a) 3 parameter fit, without diffusion (i) and with diffusion (ii)

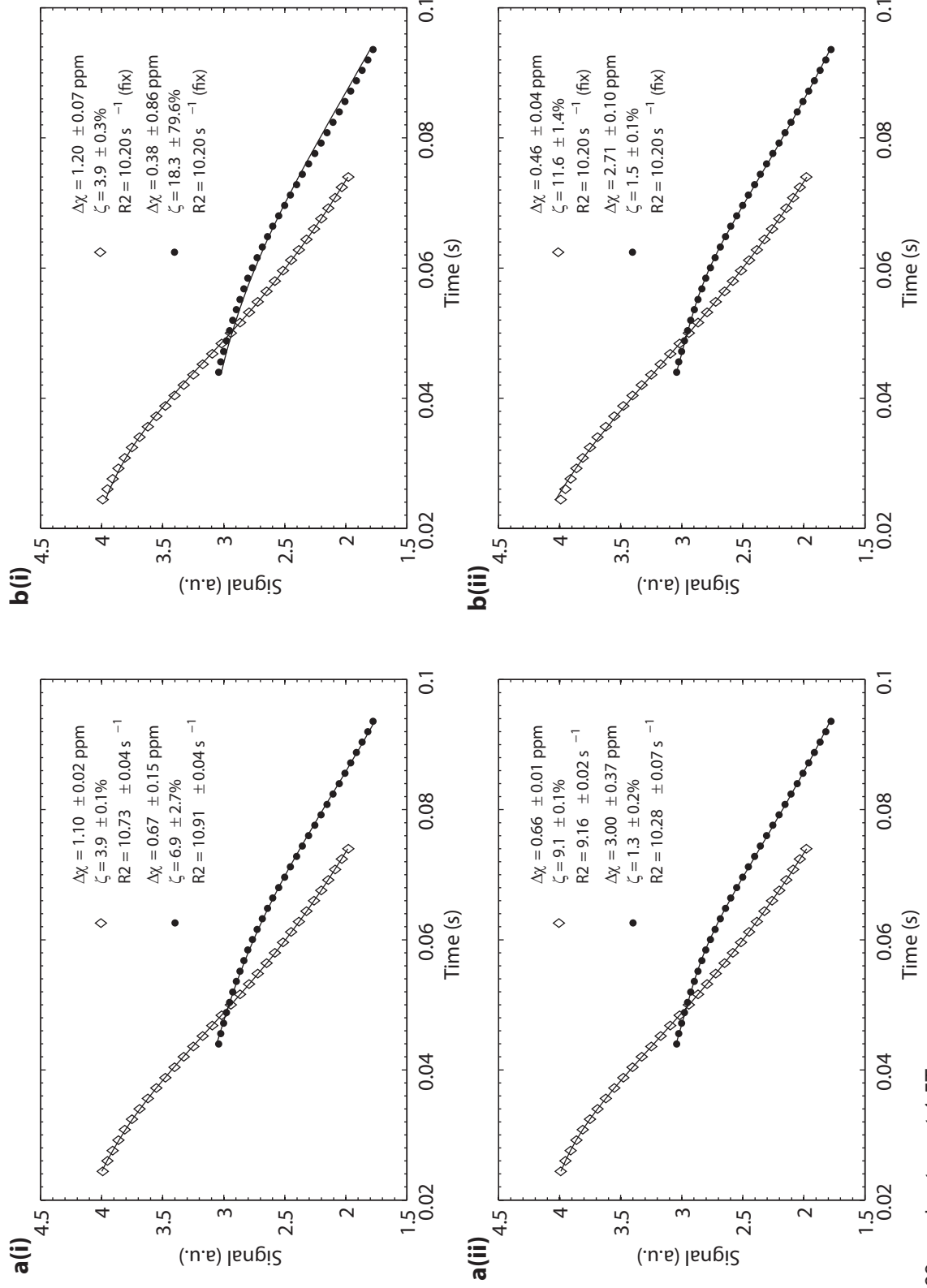
b) 2 parameter fit (fix R2), without diffusion (i) and with diffusion (ii)



63μm phantom at 3T

c) 2 parameter fit (fix ζ), without diffusion (i) and with diffusion (ii)

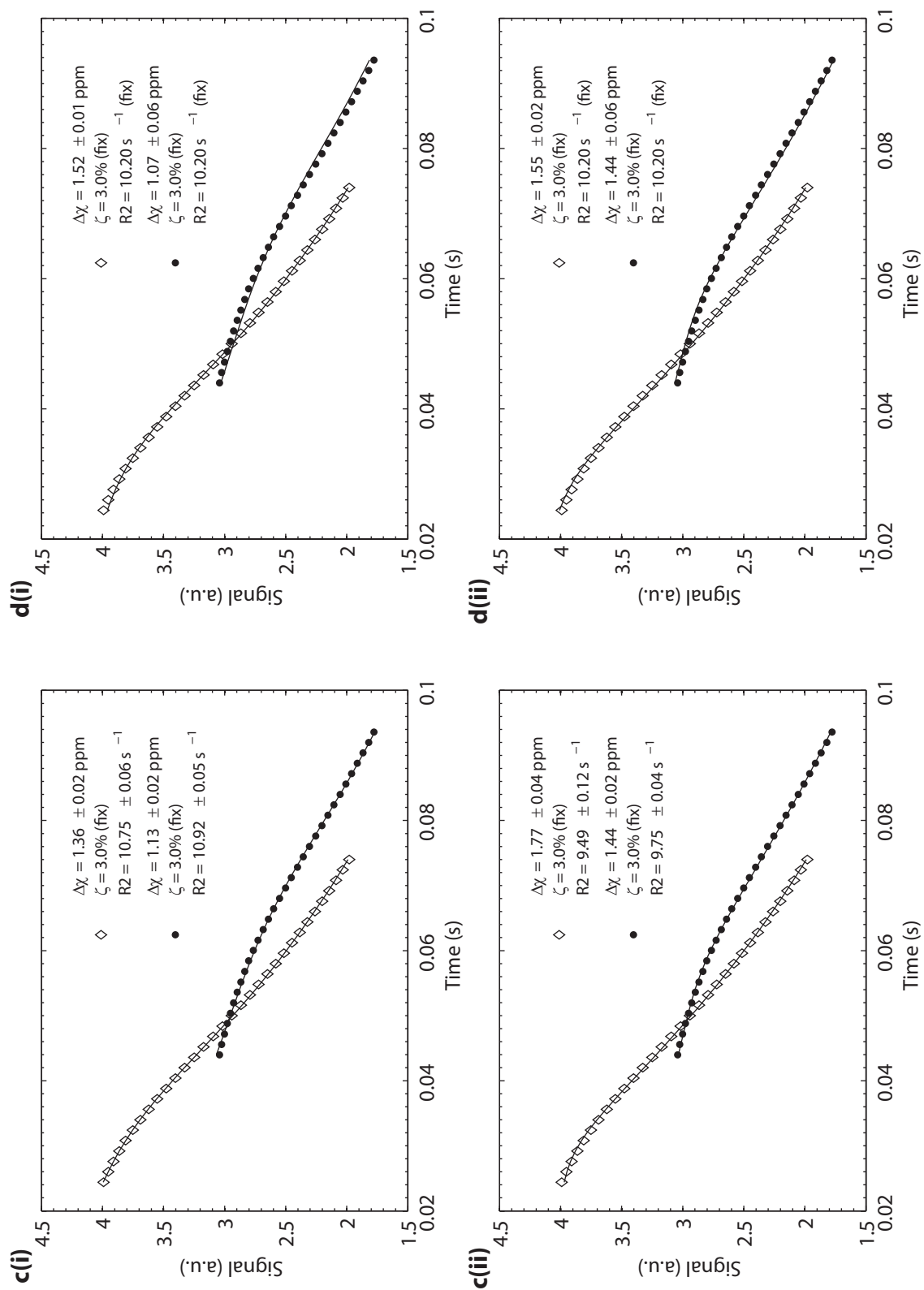
d) 1 parameter fit (fix R2 and ζ), without diffusion (i) and with diffusion (ii)



63μm phantom at 1.5T

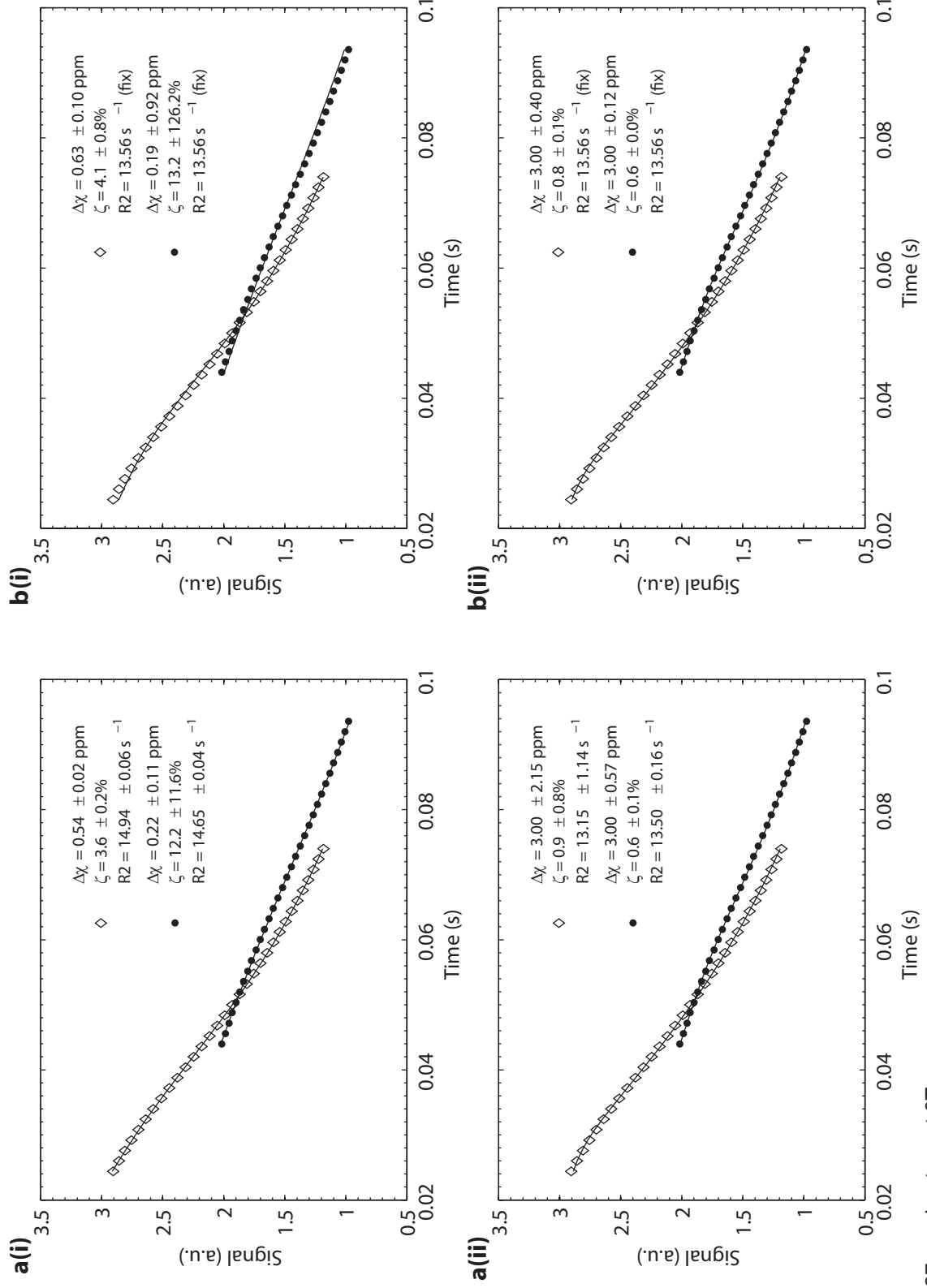
a) 3 parameter fit, without diffusion (i) and with diffusion (ii)

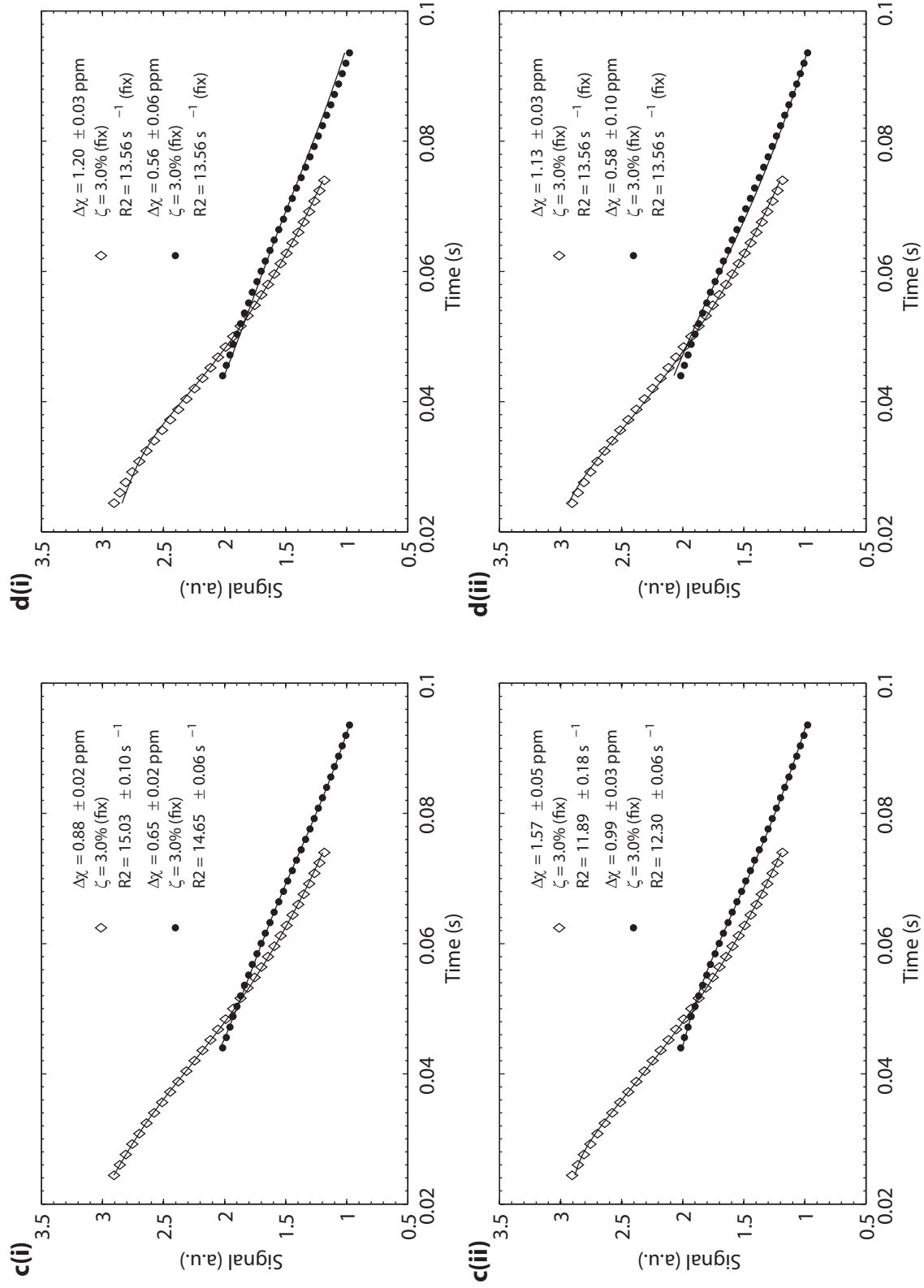
b) 2 parameter fit (fix R2), without diffusion (i) and with diffusion (ii)



63μm phantom at 1.5T

c) 2 parameter fit (fix $\Delta\chi$), without diffusion (i) and with diffusion (ii)d) 1 parameter fit (fix $R2$ and ζ), without diffusion (i) and with diffusion (ii)

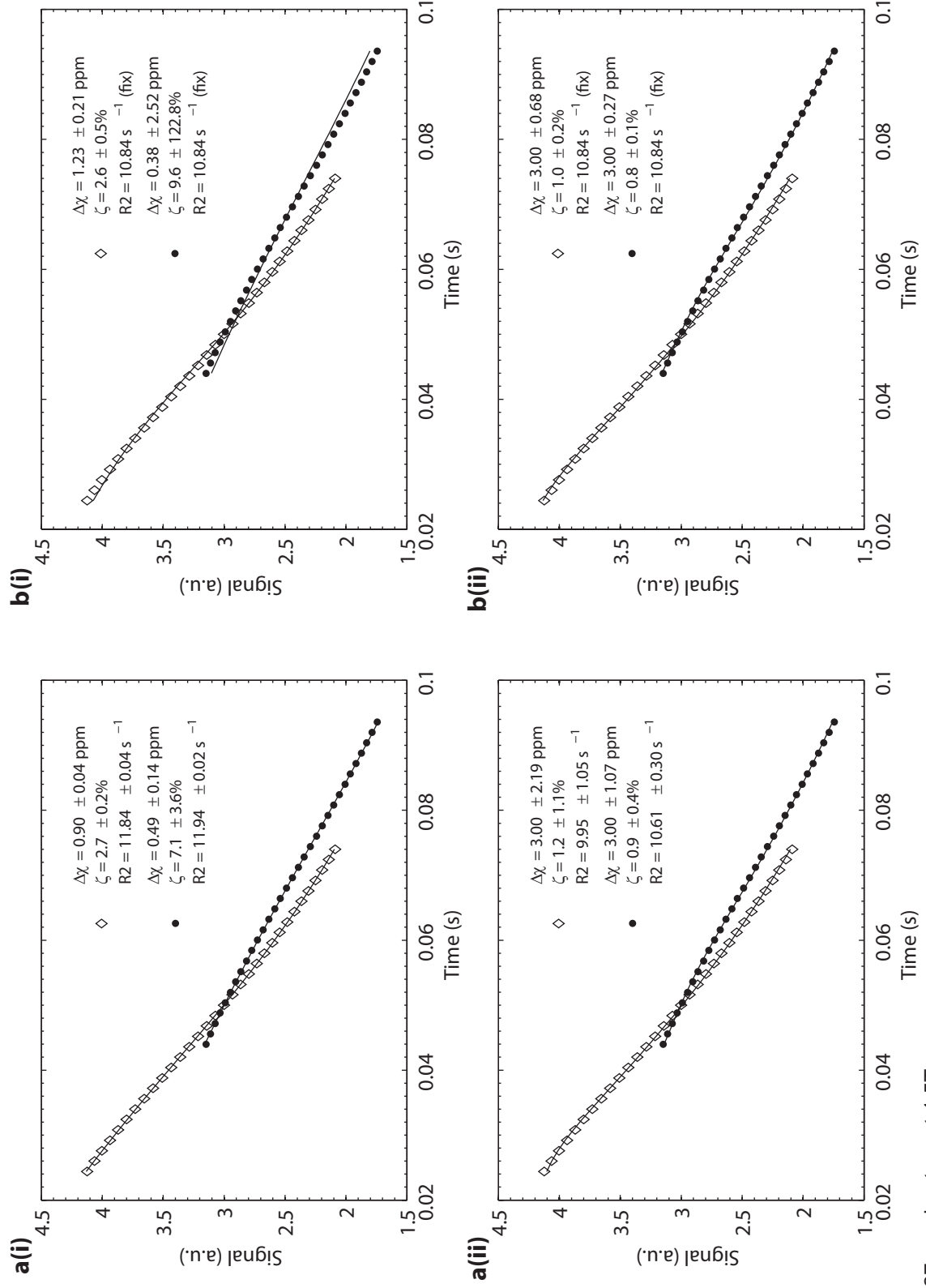


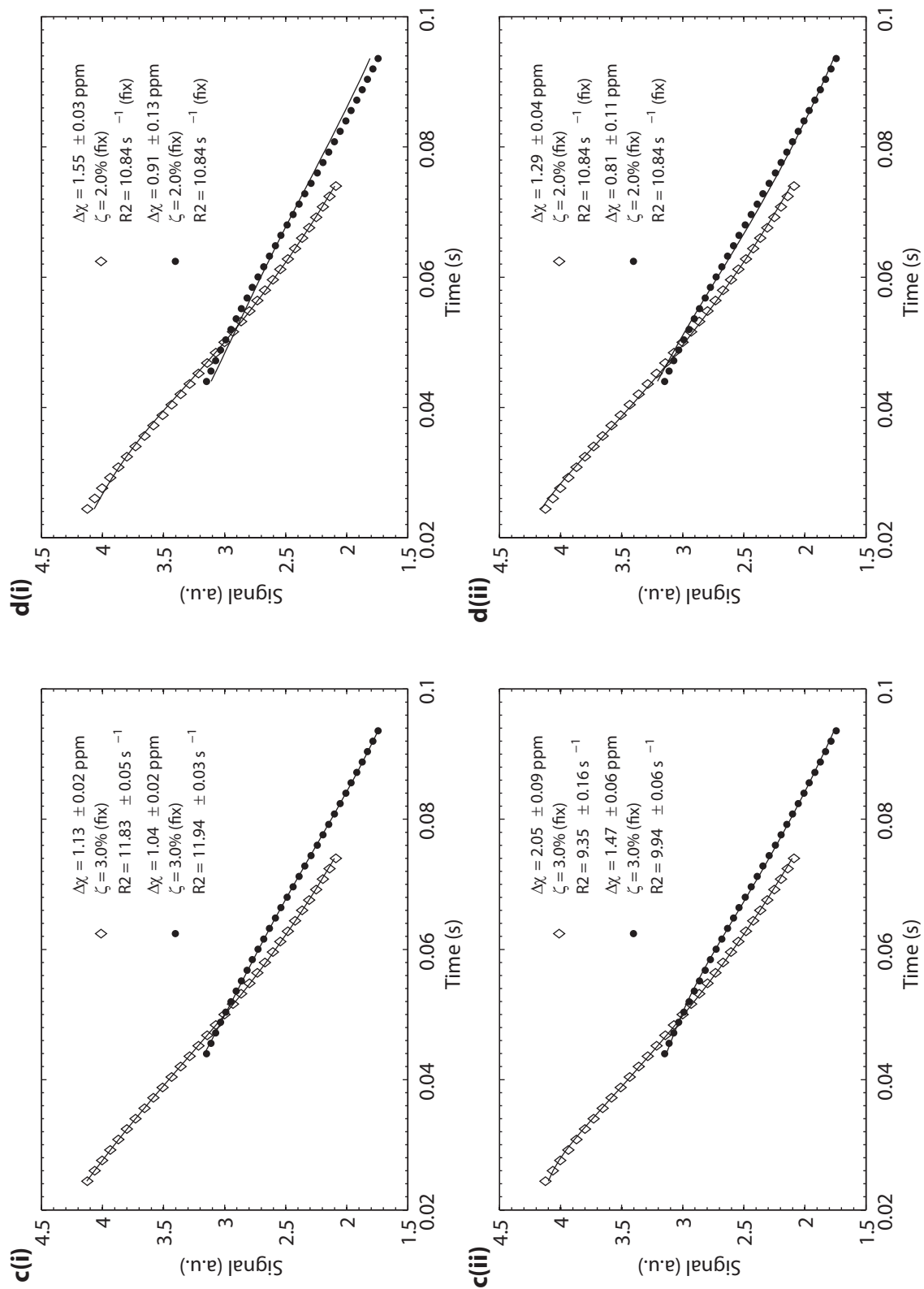


27 μ m phantom at 3T

c) 2 parameter fit (fix ζ), without diffusion (i) and with diffusion (ii)

d) 1 parameter fit (fix R2 and ζ), without diffusion (i) and with diffusion (ii)

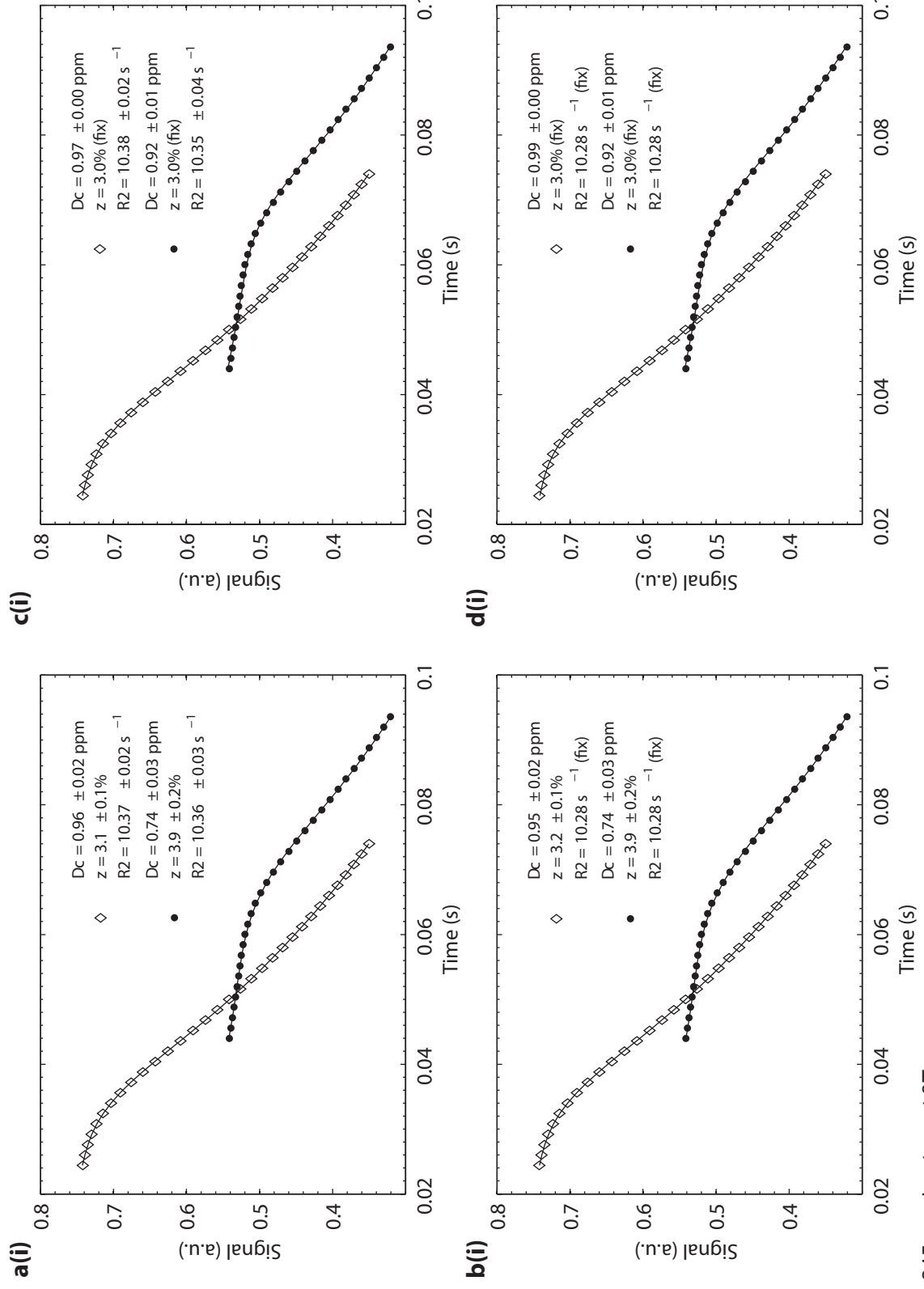


27 μ m phantom at 1.5Tc) 2 parameter fit (fix $\Delta\chi$), without diffusion (i) and with diffusion (ii)d) 1 parameter fit (fix R^2 and ζ), without diffusion (i) and with diffusion (ii)

Appendix B

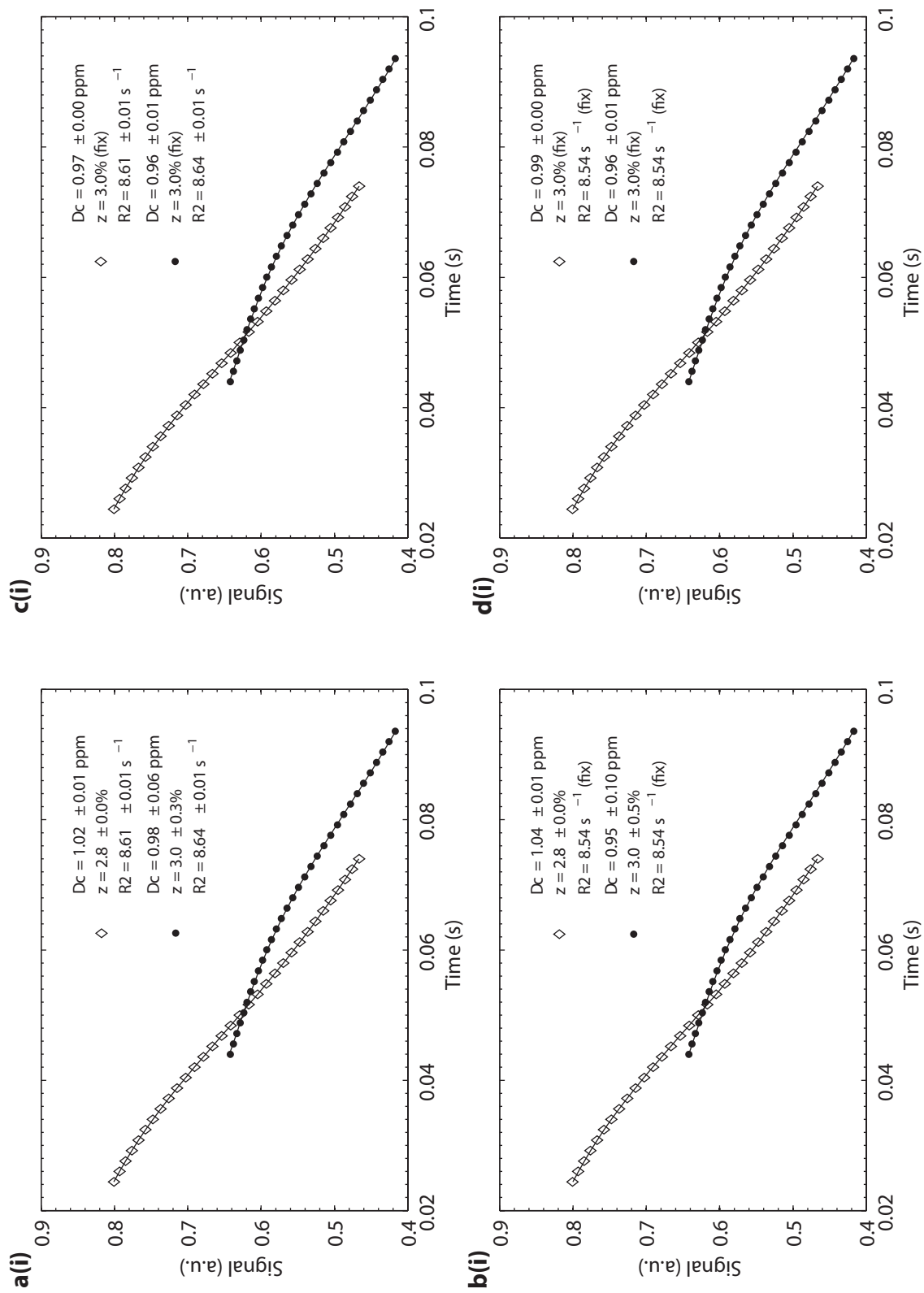
Simulated Non-static Dephasing Capillary Network Signal

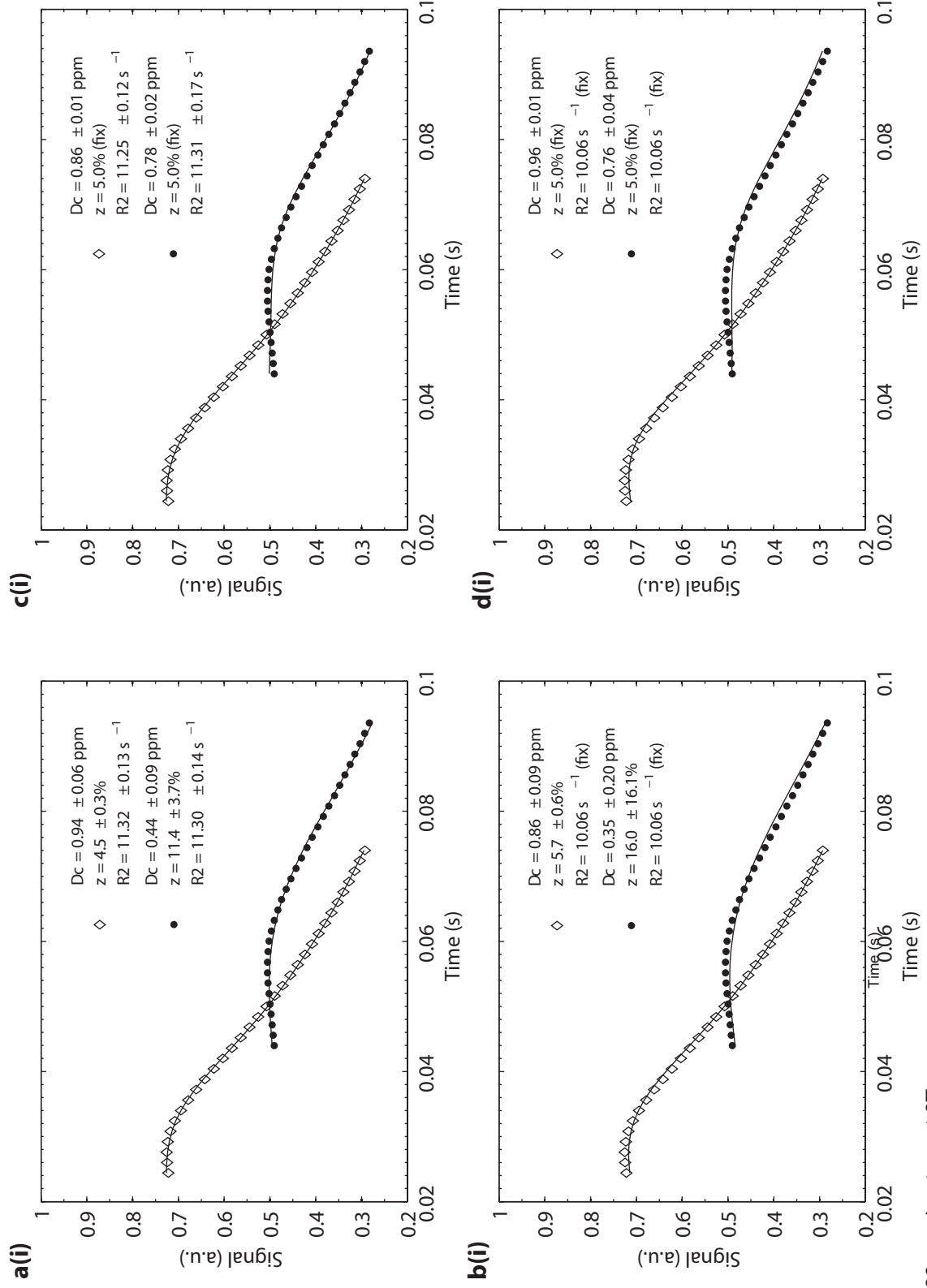
ON THE FOLLOWING pages, signal time courses calculated using the water diffusion model is shown. The signals are calculated using the network phantom specifications and the GESSE sequences used during the phantom measurements. In every plot, the parameters obtained at evaluation are specified together with the fitted signal curve (black line). The magnetic field strength and the cylinder diameter are given below the figures on respective page. Results from evaluations using three ($\Delta\chi$, ζ and $R2$) fit parameters are marked with **(a)**, evaluations with two fit parameters are labeled with **(b)** ($\Delta\chi$ or ζ) and **(c)** ($\Delta\chi$ and $R2$). The use of only one fit parameter ($\Delta\chi$) is indicated with **(d)**. All evaluations were performed without taking the simulated effect of diffusion into account, i.e., using the static dephasing model (i). For all measurement points, the error bars are equal or smaller than the symbol sizes.

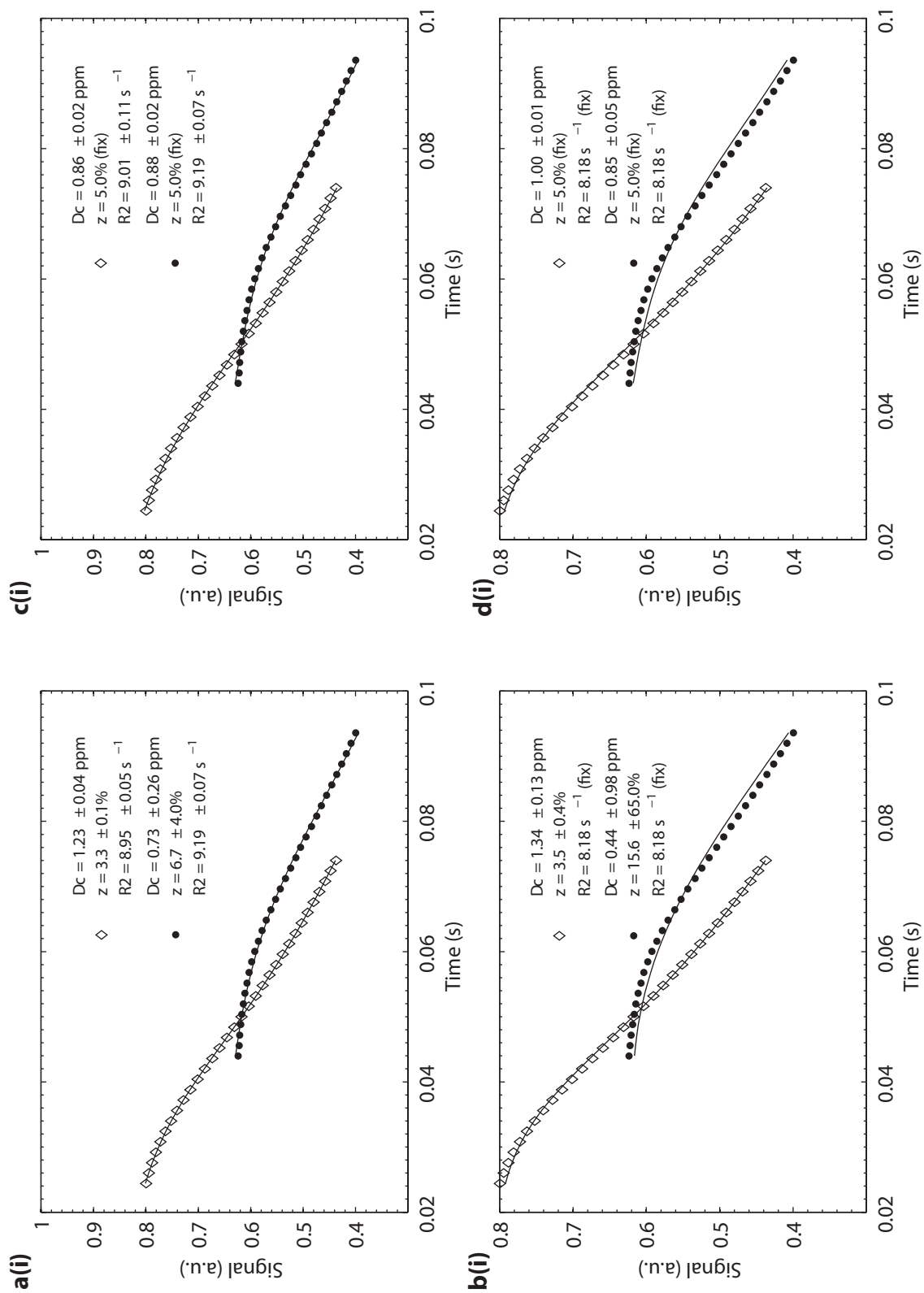


245μm phantom at 3T

a(i) 3 parameter fit, b(ii) 2 parameter fit (fix z), c(ii) 2 parameter fit (fix z), d(ii) 1 parameter fit (fix R2 and z)

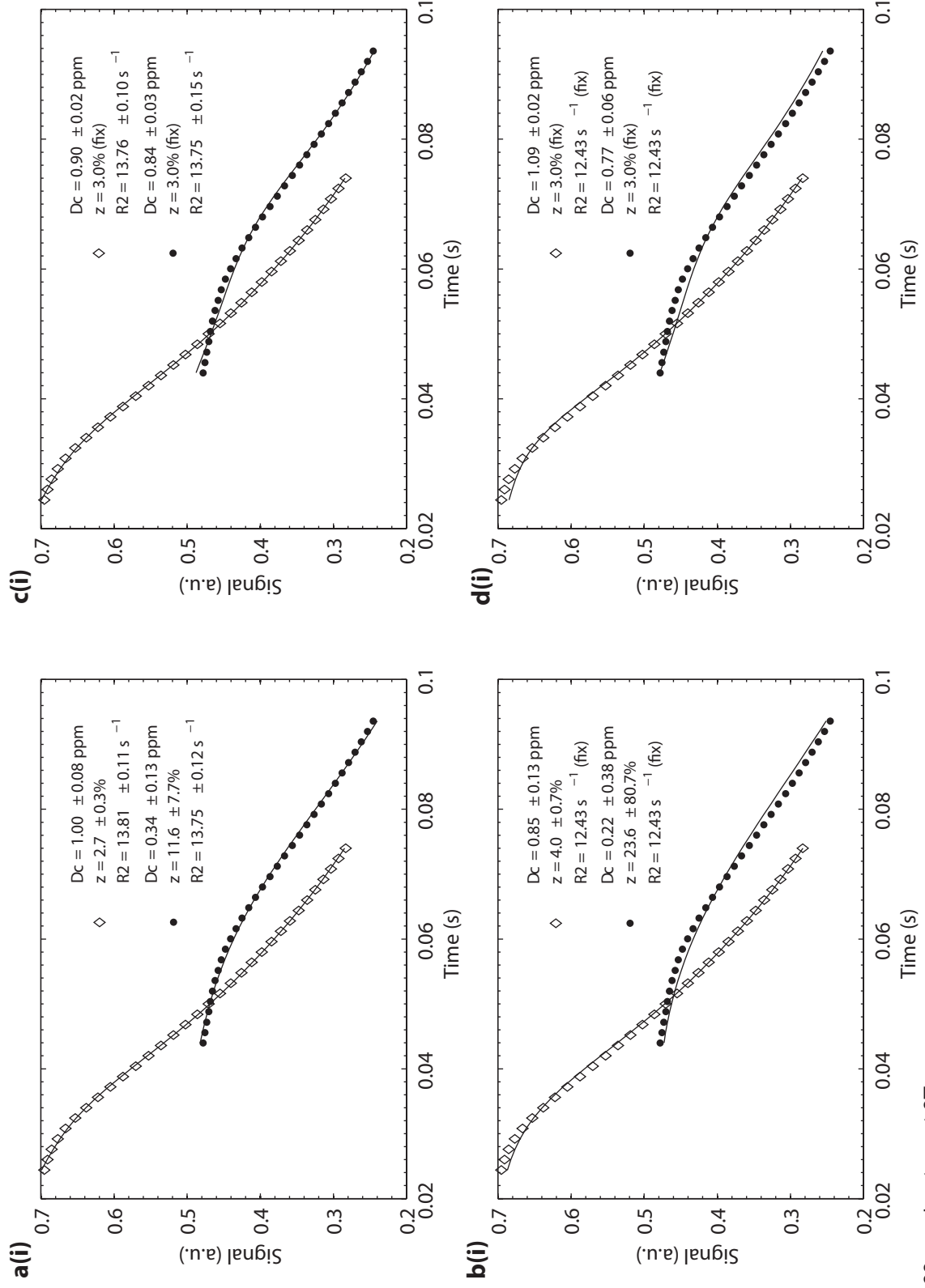
245 μ m phantom at 1.5Ta(ii) 3 parameter fit (fix R2), b(ii) 2 parameter fit (fix ζ), c(ii) 2 parameter fit (fix ζ), d(ii) 1 parameter fit (fix R2 and ζ)

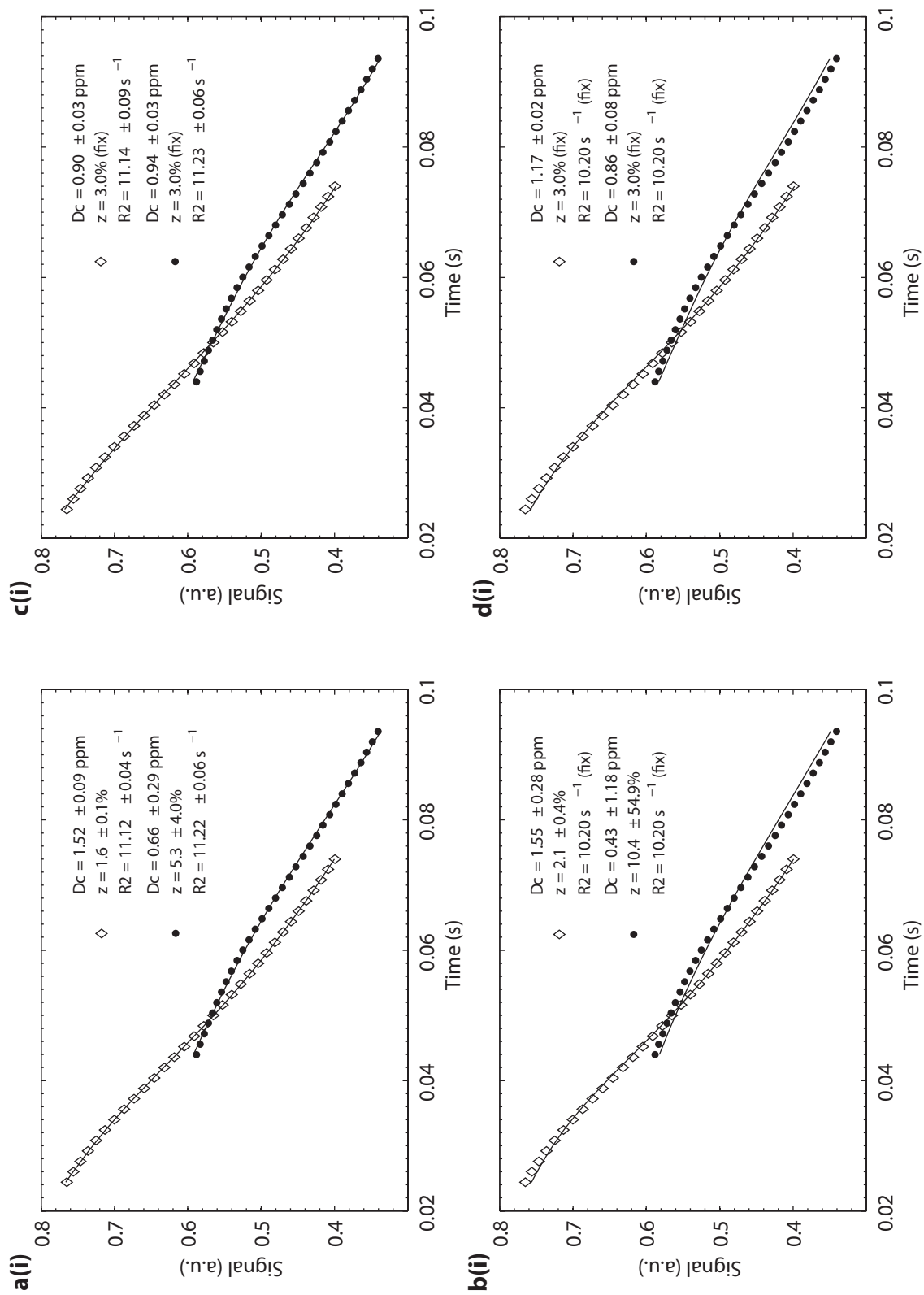




89μm phantom at 1.5T

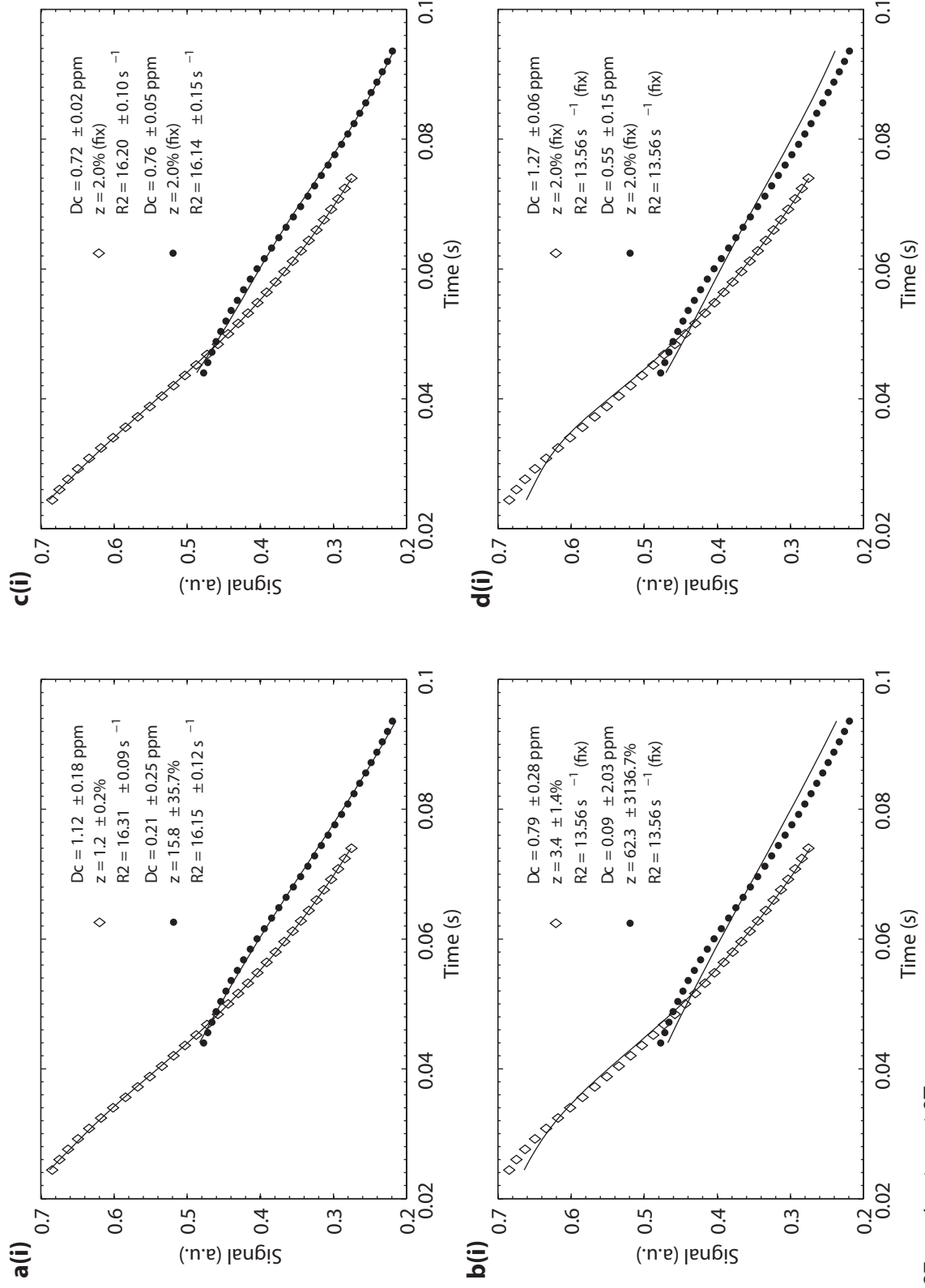
a(ii) 3 parameter fit (fix R2), b(ii) 2 parameter fit (fix ζ), c(ii) 2 parameter fit (fix ζ), d(ii) 1 parameter fit (fix R2 and ζ)

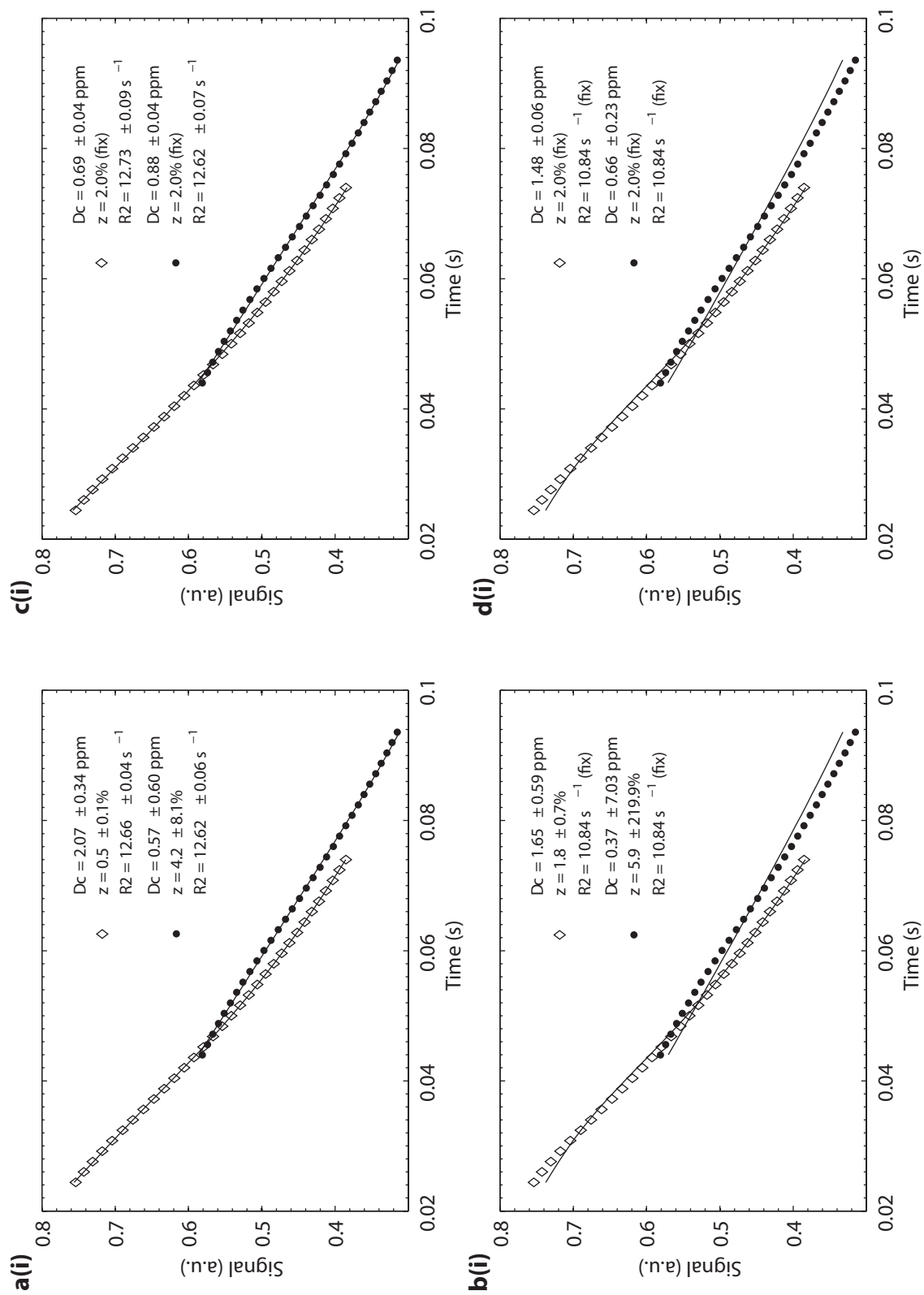




63μm phantom at 1.5T

a(ii) 3 parameter fit, b(ii) 2 parameter fit (fix R^2), c(ii) 2 parameter fit (fix ζ), d(ii) 1 parameter fit (fix R^2 and ζ)



27 μm phantom at 1.5Ta(ii) 3 parameter fit, b(ii) 2 parameter fit (fix R^2), c(ii) 2 parameter fit (fix ζ), d(ii) 1 parameter fit (fix R^2 and ζ)

Acknowledgment

At this point, I would like to express my gratitude to all those people that have supported me throughout this work.

First and foremost, I offer my sincerest gratitude to Prof. Lothar Schad and Prof. Wolfgang Schlegel for the supervision of my Ph.D. thesis. Moreover, I would like to acknowledge the advice and guidance of Prof. Wolfhard Semmler who made many valuable suggestions and gave constructive advice.

The members of my working group have contributed immensely to my personal and professional time as a Ph.D. student. The group has been a source of friendships as well as good advice and collaboration. Of all my colleagues, I want to express my special thanks to Falko Lohberger, Frederik Laun and Sebastian Schmitter for their extremely valuable support for me as a new student, and for the introduction into the field. This is also extended to Armin Nagel who eased my introduction into the German society with his welcoming manner, and who has given me a great amount of administrative help. Furthermore, I would like to thank my roommate Grzegorz Bauman for bringing joy to the everyday work with his entertaining jokes, but also for many thoughtful reflections. Thanks are due to Frederik Laun for proof reading, and Sarah Snyder for editing the English of this document. Many others that have been involved deserve recognition as well. For fear of overlooking somebody, I will not list them all. However, their support in this effort is greatly appreciated.

It would be an omission not to mention my gratitude to Jan Sedlacik, Valerij Kiselev and Dmitriy Yablonskiy for generous practical and theoretical support.

I would also like to thank the medical technical assistants and the radiologist at the department of radiology for the help and support with proband and patient measurements.

I thank the International Ph.D. program at the German Cancer Research Center for funding my work.

Finally, I want to thank my entire family for all their love. A special thought is devoted to my parents for a never-ending support. Furthermore, the support from my life companion Patrik is a powerful source of inspiration and energy. Without his help and encouragement, this study would not have been completed. I admire and thank him for his enduring patience, understanding, and love.

